Investigation of the discovery potential of a Higgs boson in the $t\bar{t}H^0, H^0 \to b\bar{b}$ channel with the ATLAS experiment

Catrin Bernius

University College London

Submitted to University College London in fulfilment of the requirements for the award of the degree of Doctor of Philosophy

6 September 2010

I, Catrin Bernius, confirm that the work presented in this thesis is my own. Where information has been derived from other sources, I confirm that this has been indicated in the thesis.

Abstract

The production of a light Standard Model Higgs boson in association with a top-quark pair at the Large Hadron Collider (LHC) is studied in a simulation of the multipurpose ATLAS experiment. The Higgs boson is assumed to decay into a $b\bar{b}$ pair, and the top-quark pair to decay semi-leptonically. The main background process for this channel is the production of $t\bar{t}$ events, which can be divided into reducible and irreducible components. In the process of generating these components separately, an overlap of events is created through the addition of b-quarks to $t\bar{t}$ events via parton showering in the $t\bar{t}X$ sample. These events are already included in the matrix-element cross-section calculation for the $t\bar{t}b\bar{b}$ sample. A new procedure for the overlap removal is presented in this thesis.

Two analyses are studied, where one aims at the full reconstruction of the final state using a cut-based approach. Recently, this way of reconstructing the $t\bar{t}H^0(H^0 \to b\bar{b})$ process has been found to be extremely challenging. The other analysis is based on a new method employing state-of-the-art jet reconstruction and decomposition techniques where the $t\bar{t}$ pair and the Higgs boson are required to have large transverse momenta and can therefore be reconstructed as massive Higgs and top jets. A recent phenomenological study has shown that the $t\bar{t}H^0$ process can be recovered as a promising search channel for a low mass Standard Model Higgs boson around 120 GeV using this approach. Finally, to enhance the sensitivity of the $t\bar{t}H^0$ channel, a combination of the two analyses is presented.

Summary of Contributions

In this thesis, two analyses to study the $t\bar{t}H^0(H^0 \rightarrow b\bar{b})$ Higgs boson search channel are presented, where the Higgs boson is produced in association with a $t\bar{t}$ pair and decays to a $b\bar{b}$ pair.

One analysis is a cut-based selection method for identifying the Higgs boson and aims at the full reconstruction of the final state. This analysis is based on a previous analysis [5] performed at a centre-of-mass energy of $s = \sqrt{14}$ TeV but has been repeated and optimised with more refined simulated data at $s = \sqrt{10}$ TeV. The obtained statistical significance is discussed together with the systematic errors and compared to the earlier analysis.

The second analysis forms the major analysis and original contribution to this thesis. It is the very first detector level study carried out in the $t\bar{t}H^0(H^0 \rightarrow b\bar{b})$ search channel, employing a new method of jet reconstruction and decomposition techniques and based on a recent phenomenological study [3]. This analysis exploits the boosted regime, where the Higgs boson is produced with very large transverse momentum.

Finally, a way of combining the two analyses is studied and the results are presented.

A more technical contribution in this thesis is a new technique which has been developed to remove the overlap in the $t\bar{t}b\bar{b}$ and $t\bar{t}X$ data samples used in both analyses.

Acknowledgements

Many people have contributed to my PhD studies with their help and guidance. I would like to take the opportunity to thank all of them.

I'd like to thank my supervisor, Dr. Nikos Konstantinidis. He offered me the possibility to work on interesting subjects and I'd like to thank him for his help and advice throughout my PhD.

Furthermore I would like to thank Dr. Simon Dean for valuable advice, support, guidance, encouragement and patience, especially in the last few months of my PhD. He has not only been a great colleague but also become a very good friend of mine over those past four years.
Thank you also to Adam Davison for all the helpful physics and technical discussions, the support and encouragement and for being a great friend. I am very grateful to both of you for your never ending support and friendship!

I would like to thank the Artemis Research and Training Network for their generous financial support and the members of the Artemis RTN for their valuable advice and suggestions during the duration of the funding.

The work presented in this thesis could not have been realised without the help of the UCL Particle Physics Group and the ATLAS Collaboration, in particular the ATLAS Higgs Working Group. I'd also like to thank the UCL HEP group for their advice and suggestions during the weekly physics meetings, as well as my colleagues and friends at UCL, CERN, in Germany and in Geneva.

Finally, I sincerely thank my parents, grandma and sister, for giving me so much love and unconditional support throughout my life, but especially during the last few years. Thank you all for all the opportunities you have provided and worked so hard for.

Contents

List of Figures

List of Tables

Chapter 1

Introduction

The Large Hadron Collider (LHC) at CERN, currently operating at a centre-of-mass energy of 7 TeV, will provide proton-proton collisions with an unprecedented centre-of-mass energy of 14 TeV and with instantaneous luminosities of up to 10^{34} $cm^{-2}s^{-1}$ and is therefore ideally suited to explore the TeV energy domain. It will play an important role in the investigation of fundamental questions of particle physics.

The Standard Model of particle physics describes three of the four known fundamental interactions between the elementary particles: the electromagnetic, weak and strong forces. It provides an extremely accurate description of the electroweak and strong interactions and is in excellent agreement with the numerous experimental measurements. However there is one particle predicted by the Standard Model whose existence has not yet been proven to the present day: the Higgs boson. The Higgs boson is the most-wanted elementary particle in physics as it plays a crucial role of giving other particles a mass without breaking the gauge symmetry the model is built upon. Almost all physical properties of the Higgs boson are predicted by theory, the one which is unknown is its mass.

Direct searches performed at the LEP2 collider exclude a Standard Model Higgs boson with a mass below 114.4 GeV/c^2 at 95% confidence level [1]. Indirect constraints from electroweak precision observables, where a Higgs boson enters through virtual corrections, predict a Higgs boson mass of 89^{+35}_{-26} GeV/c^2 [2]. Under the

assumption that the Standard Model and the theory of the Higgs mechanism are valid, the Higgs boson mass is therefore expected to be close to the LEP2 limit.

This thesis presents two different ways of searching for a Higgs boson in the process $pp \rightarrow t\bar{t}H^0$, where the Higgs boson is produced in association with a $t\bar{t}$ pair and decays to a $b\bar{b}$ pair. The analyses presented here are based on a realistic simulation of the ATLAS detector, one of the two multipurpose experiments at the LHC.

One approach aims at fully reconstructing the final state of the process, assigning the decay products of the two top quarks and the Higgs boson to their mother particles.

The other approach was proposed recently [3] and relies on the already well known associated production of a Higgs boson with a $t\bar{t}$ pair, but where only the phase space region where the Higgs and the top quarks are produced at large transverse momenta is considered. This approach of a Higgs analysis in the boosted regime is based on a study carried out in the process where a Higgs boson is produced in association with a W or Z boson [4] which reinstated the WH/ZH channels as Higgs discovery channels in the low mass range.

A first detector level study of the $t\bar{t}H^0(H^0 \rightarrow b\bar{b})$ Higgs boson search channel in the boosted regime, based on a realistic simulation of the ATLAS detector, is presented in this thesis. The discovery potential, based on simple event counting, is analysed in terms of statistical significance.

Finally, the effect of a combination of the two analyses on the sensitivity of the $t\bar{t}H^0(H^0 \rightarrow b\bar{b})$ process is studied.

The main background for the $t\bar{t}H^0$ process is the production of $t\bar{t}$ events. This background can be divided into reducible and irreducible components, depending on whether or not the final state particles are identical to those in $t\bar{t}H^0$. To be able to study the contributions and behaviour of these backgrounds individually, they are all simulated separately from each other. The separate generation of the background introduces an overlap of events through the addition of b-quarks to $t\bar{t}$ events via parton showering in the $t\bar{t}X$ sample. These events are already included in the matrix-element cross-section calculation for the $t\bar{t}b\bar{b}$ sample. A new procedure for

removing this overlap has been developed here as an improvement to the technique previously used in [5].

The thesis is organised as follows: The LHC collider and ATLAS detector are briefly described in Chapter 2. A short overview of the theory of elementary particle physics and interactions, with emphasis on the mechanism of electroweak symmetry breaking, is given in Chapter 3. Chapter 4 gives an overview of how the simulated data is generated and how the final state particles are identified. The reconstruction of the $t\bar{t}H^0(H^0 \rightarrow b\bar{b})$ final state is presented in Chapter 5. In Chapter 6, the procedure of removing the parton shower/matrix element overlap in $t\bar{t}$ backgrounds of the $t\bar{t}H^0$ channel is described. The Higgs boson search in the boosted regime is then described in Chapter 7, while the combination of the two analyses is discussed in Chapter 8.

Chapter 2

The Large Hadron Collider and the ATLAS Detector

2.1 The LHC

The Large Hadron Collider (LHC) [6, 7, 8] is a superconducting hadron accelerator and collider installed in the 26.7 km tunnel that was constructed between 1984 and 1989 for the CERN Large Electron Positron (LEP) machine. Being a particle-particle collider, there are two rings with counter-rotating beams, unlike particle-antiparticle colliders where both beams share a single ring. To keep the accelerated particles along the curved trajectory, a two-in-one design was chosen for the superconducting magnets, providing a magnetic field in opposite directions for the two nearby lying accelerated particle beams. The LHC is designed to collide proton beams with a centre-of-mass energy of $\sqrt{s} = 14$ TeV, but can also collide heavy (Pb) ions with an energy of 2.8 TeV per nucleon.

Figure 2.1 shows a schematic overview of CERN's accelerator complex located at the Swiss-French border near Geneva. Protons are produced through ionisation of hydrogen a ion beam source, with a so-called *duo-plasmatron source*. Before they are injected to the LHC, the protons are pre-accelerated in different stages. At the beginning of the acceleration chain, a linear accelerator (LINAC) and a subsequent booster injects the protons into the Proton Synchrotron (PS) which accelerates them to 26 GeV. The protons are then transferred into the Super Proton Synchrotron

(SPS) where the energy is increased to 450 GeV before they are injected into the LHC. In fully operational mode, the LHC accelerates the proton beams to their final energy of 7 TeV, providing a centre-of-mass energy of 14 TeV.

The delivered instantaneous luminosity is a very important parameter of an accelerator. The proton beams will be structured in 2808 spatially distinct bunches, each with 10^{11} protons, the nominal separation being 25 ns which corresponds to a distance of 7.5 m. This means the protons will collide every 25 ns, resulting in 40 000 000 bunch-bunch collisions per second. The proton beams are not collided head on but at a small crossing angle of the order $150 - 200$ μrad to avoid the occurrence of parasitic collisions. The machine luminosity $\mathcal{L}$ is given by:

$$\mathcal{L} = \frac{N_B^2 n_B f_{rev} \gamma_r}{4\pi \epsilon_n \beta^*} F \tag{2.1}$$

where N_B is the number of particles per bunch, n_B the number of bunches per beam, f_{rev} the revolution frequency, γ_r the relativistic gamma factor, ϵ_n the normalised transverse beam emittance, β^* the beta function at the collision point and F the geometric luminosity reduction factor due to the crossing angle at the interaction point (IP). The normalised transverse beam emittance ϵ_n is a convenient quantity for the operation of a hadron storage ring and describes the decrease of beam emittance with increasing beam energy during acceleration.

More commonly used is the integrated luminosity $L = \int \mathcal{L} dt$, the integral of the instantaneous luminosity $\mathcal{L}$ over time. The design luminosity of the LHC is $\mathcal{L} = 10^{34}$ cm^{-2}s^{-1}. One year running at design luminosity corresponds to an integrated luminosity of $L = 10$ fb^{-1}. The number of events generated in the LHC collisions is given by:

$$N_{event} = \sigma_{event} L \tag{2.2}$$

where σ_{event} is the cross-section for the event under study and L the integrated luminosity. While it is extremely unlikely that more than one colliding proton pair will produce a high p_T hard scattering event, in general several additional low p_T interactions will take place among other proton pairs in the same bunch crossing, so-called *minimum bias* or *pile-up* interactions. The amount of pile-up events depends

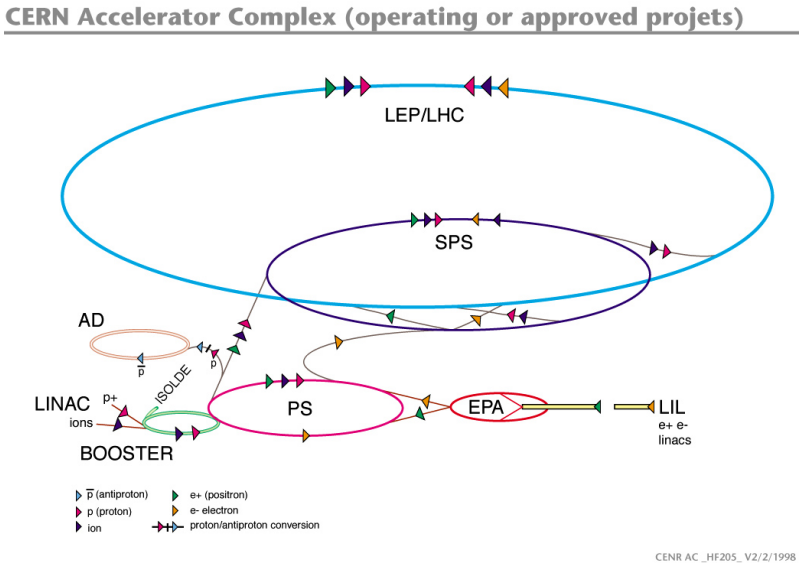

Figure 2.1: Schematic overview of the accelerator complex at CERN. The accelerator chain starts with the linear accelerator (LINAC). A subsequent booster transfers the protons into the Proton Synchrotron (PS) and from there into the Super Proton Synchrotron (SPS) before they are injected in the Large Hadron Collider (LHC).

on the instantaneous luminosity and on the bunch spacing. At design luminosity, on average 23 pile-up interactions are expected.

The LHC has two multipurpose experiments, ATLAS [9] and CMS [10], both designed for a peak luminosity of $\mathcal{L} = 10^{34}\text{cm}^{-2}\text{s}^{-1}$ during proton collisions. Additionally there are LHCb [11] for B-physics; TOTEM [12] foreseen to detect protons from elastic scattering at small angles; and an experiment dedicated to the LHC operation with ion beams, the ALICE experiment [13].

2.2 The ATLAS Detector

The ATLAS (**A** **T**oroidal **L**HC **A**pparatu**S**) detector [9] is a multi-purpose detector designed to fully exploit the discovery potential of the LHC. The detector has a cylindrical symmetry with a radius of 11 m, a length of 44 m, and a weight of about 7000 tons. The overall layout of the ATLAS detector is shown in Figure 2.2. The main components of the detector extend radially, starting from the interaction point.

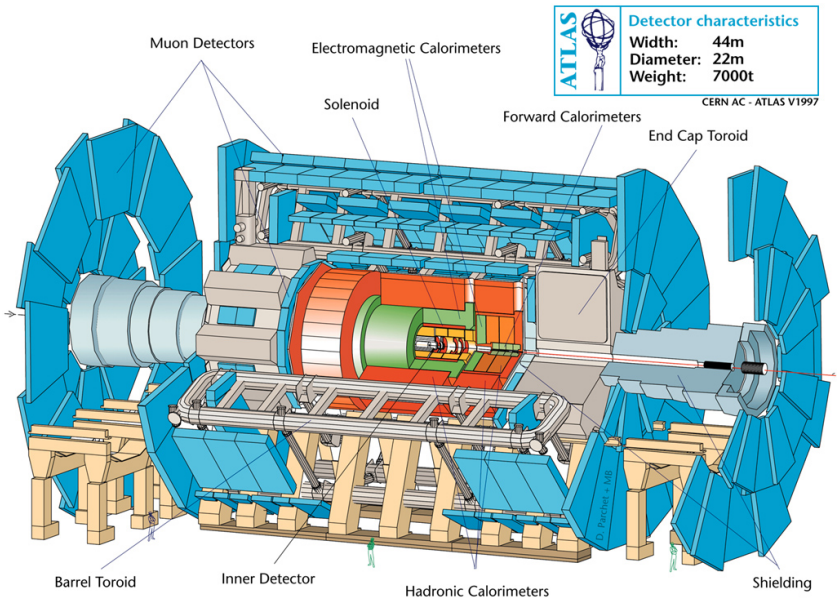

Figure 2.2: Three dimensional drawing of the ATLAS detector showing the main detector components: the inner detector (yellow), the electromagnetic (green) and hadronic (orange) calorimeter and the muon system (blue), as well as the solenoid and toroid magnets.

Centred in the middle of the detector surrounding the interaction point is the inner detector (ID). It is embedded in a solenoidal magnet which generates a roughly homogenous 2 Tesla field parallel to the beam axis. A combination of high-resolution semiconductor pixel and strip detectors around the interaction point and straw-tube tracking detectors with the capability to generate and detect transition radiation in the outer part make it possible to perform pattern recognition, momentum and vertex measurements as well as electron identification.

The calorimeter consists of an electromagnetic (EM) and a hadronic calorimeter, situated outside the solenoid. The high granularity liquid-argon (LAr) electromagnetic calorimeters provide very good performance in terms of energy and position resolution. Located around it is the hadronic calorimeter, a scintillator-tile calorimeter in the central region but using LAr technology in the end-caps.

The calorimeter is surrounded by the outermost layer of the ATLAS detector, the muon spectrometer. An air-core toroid system generates a magnetic field with strong bending power in a large volume within a light and open structure. Excellent

measurement of muon tracks and momenta independent of the inner detector is achieved.

A more detailed description of the ATLAS detector can be found in the technical design report (TDR) [14, 15], which is updated by Ref. [16], on which the present chapter is largely based.

Detector Terminology

The nominal interaction point is the origin of a xyz-coordinate system. The positive x-axis is defined as pointing in the direction of the centre of the LHC ring and the positive y-axis points to the surface. The $x-y$ plane is transverse to the beam and the z-axis follows the beam direction so that the axis system is right-handed. The radial distance r in the transverse plane is defined as $r = \sqrt{x^2 + y^2}$. The azimuthal angle ϕ covers the range of $\phi \in [0, 2\pi]$ and is measured in the $x-y$ plane, originating from the x-axis, so that the positive x-axis has an azimuthal angle of $\phi = 0$ and the positive y-axis an angle of $\phi = \pi/2$. The polar angle θ is measured from the positive z-axis with $\theta = 0$ being the z-axis, covering the range of $\theta \in [0, \pi]$.

Both angles can be expressed using the momentum components as $\tan\phi = p_y/p_x$ and $\cot\theta = p_z/p_T$ where p_x, p_y and p_z denote the components of the momentum corresponding to the axis system and the transverse momentum $p_T = \sqrt{p_x^2 + p_y^2}$ is defined with respect to the beam axis.

In the case of massive objects (such as jets), the rapidity $y = \ln[(E+p_z)/(E-p_z)]$ is used, where E is the energy of the object. For highly relativistic particles, the pseudorapidity η is used as a good approximation within the relativistic limit for the rapidity y. The pseudorapidity is related to the polar angle through the equation:

$$\eta \equiv -\ln\left[\tan\left(\frac{\theta}{2}\right)\right]. \tag{2.3}$$

The distance ΔR in the pseudorapidity-azimuthal angle space is defined as $\Delta R = \sqrt{\Delta\eta^2 + \Delta\phi^2}$.

2.2.1 Inner Detector

The inner detector combines high-resolution detectors at the inner radii with continuous tracking elements at the outer radii, all contained in the solenoid which

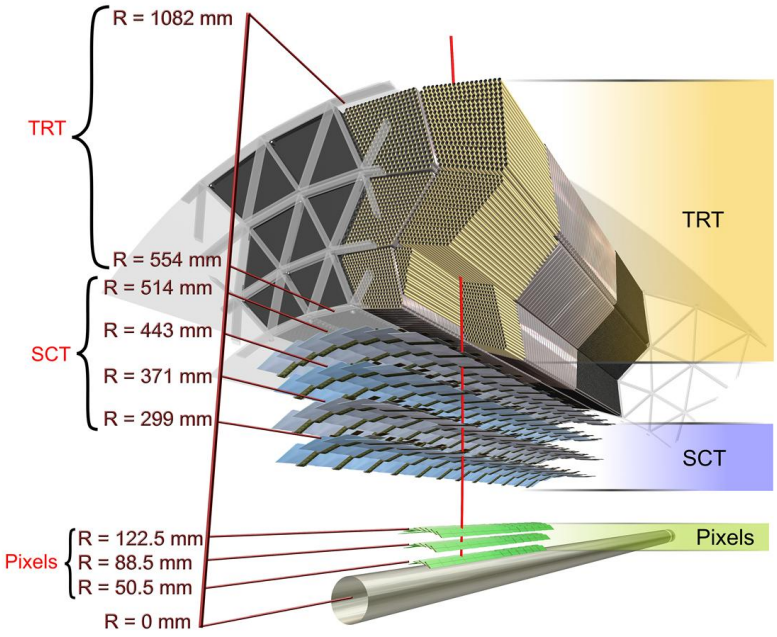

Figure 2.3: Three dimensional view of central part of the inner detector. The high-resolution detectors (pixel detector and Semiconductor Tracker (SCT)) are located at inner radii and the continuous tracking elements at outer radii (Transition Radiation Tracker (TRT)). Taken from [16].

provides a nominal magnetic field of 2 Tesla. It was designed to reconstruct the trajectories of charged particles by combining the energy hits deposited in the various sub-detectors and provides full tracking coverage over a pseudorapidity range of $|\eta| < 2.5$. The layout of the central part of the inner detector is shown in Figure 2.3.

Approximately 1000 particles will emerge from the collision point every 25 ns. This large track density requires the use of tracking layers with high granularity to be able to perform high-precision measurements. To meet these criteria, semiconductor tracking detectors, using silicon micro-strip (SCT) and pixel technologies are used close to the beam pipe in conjunction with the straw tubes of the Transition Radiation Tracker (TRT). In the barrel region, they are arranged in concentric cylinders around the beam axis while in the end-cap regions they are located on

disks perpendicular to the beam axis.

The combination of precision trackers at small radii with the TRT at a larger radius gives very robust pattern recognition and high precision in both $r-\phi$ and z coordinates. The spatial and transverse resolutions for tracking parameters using the inner detector as a whole are given in Table 2.1.

Pixel Detector

The pixel detector is designed to provide a very high-granularity, high-precision set of measurements as close to the interaction point as possible. The barrel part consists of three concentric cylindrical layers and the end-caps of three disks. All pixel sensors are segmented in $r-\phi$ and z and have a minimum pixel size in $r-\phi \times z$ of 50 $\times$ 400 μm^2. Each pixel element has its own readout chip and buffering units for storing the data, while awaiting the trigger decision.

The whole system contains 80.4 million readout channels, providing intrinsic accuracies in the barrel of 10 μm in the $r-\phi$ plane and 115 μm along the z direction and in the disks of 10 μm in the $r-\phi$ plane and 115 μm along the r direction. In general, a charged track will leave energy deposits in three pixel layers. The first of these layers (b-layer) is positioned as close as possible to the interaction region in order to achieve the best possible impact parameter resolution, which is extremely important for an efficient b-jet identification

Semiconductor Tracker (SCT)

The SCT uses small-angle (40 mrad) stereo strips to measure both coordinates. In the barrel region one of these strips is parallel to the beam direction, while in the end-cap region one of them is running radially, both measuring directly $r-\phi$. They consist of two sensors with a strip pitch of 80 μm. Eight strip layers are crossed by each track, corresponding to four space points.

The intrinsic accuracies per module in the barrel are 17 μm ($r-\phi$) and 580 μm (z) and in the disks are 17 μm ($r-\phi$) and 580 μm (r). The total number of readout channels in the SCT is approximately 6.3 million.

Track parameter	$0.25 < \|\eta\| < 0.5$	$1.50 < \|\eta\| < 1.75$
Inverse transverse momentum ($\frac{q}{p_T}$)	0.34 TeV^{-1}	0.41 TeV^{-1}
Azimuthal angle (ϕ)	70 μrad	92 μrad
Polar angle (cotθ)	0.7×10^{-3}	1.2×10^{-3}
Transverse impact parameter (d_0)	10 μm	12 μm
Longitudinal impact parameter ($z_0 \sin\theta$)	91 μm	71 μm

Table 2.1: Expected spatial and transverse inner detector momentum resolutions for tracks in representative regions in η. The momentum and angular resolutions are shown for muons, whereas the impact-parameter resolutions are shown for pions. The values are shown for two η regions, one in the barrel inner detector where the amount of material is close to its minimum and one in the end-cap where the amount of material is close to its maximum. Taken from [16].

Transition Radiation Tracker (TRT)

The TRT was designed to provide a relatively large number of space point measurements at low cost and material. This is achieved by using drift straws of 4 mm diameter which allow tracks up to $|\eta| = 2$ to be reconstructed using a large number of hits (typically 36 per track). The TRT provides $r - \phi$ information only in the barrel, for which it has an intrinsic accuracy of 130 μm per straw. In the barrel region the straws are parallel to the beam axis on three cylinders with a maximum length of 144 cm. The wires are divided into two halves at around $\eta = 0$. Following the design of the SCT, the 37 cm long straws in the end-caps point towards the beam axis and are arranged in 18 wheels on each side. The total number of TRT readout channels is approximately 351,000.

While the intrinsic position resolution of the TRT cannot compete with the resolution of the silicon technology based detectors, the high number of measurements and the long lever arm with respect to the measurements in the silicon layers means that the TRT significantly contribute to the determination of the momentum resolution.

The TRT can also be used for particle identification by detecting transition radiation when a relativistic particle crosses the boundary between two media with

different electrical properties (polypropylene foils between the straws). This allows the separation of electrons from pions and to a much smaller extent the separation of kaons from pions. Light particles like electrons start emitting transition radiation at low momentum ($\sim$ 1 GeV) while heavier charged particles like pions emit transition radiation at high momenta ($\sim$ 100 GeV). By tuning the readout threshold of each straw, particles can be selected and identified.

2.2.2 Calorimeter

While tracking detectors are designed to have a minimal effect on the particle, the calorimeter measures the energy of the incident particle through total absorption. Calorimeters must also be hermetic to achieve a good resolution of the measurement of the missing transverse momentum.

The ATLAS calorimeter has a coverage up to $|\eta| = 4.9$. Different technologies are used across different regions in pseudorapidity, as shown in Figure 2.4. Over the $|\eta|$ range where the calorimeter is surrounding the inner detector, the EM calorimeter is finely segmented to precisely measure electrons and photons, while the rest of the calorimeter is more coarsely segmented for jet reconstruction and missing transverse energy (E_T^{miss}) measurements.

Another design criterion for the calorimeter is to provide good containment for electromagnetic and hadronic showers of particles with energies around the TeV scale in order to minimise the punch-through into the muon system and to provide a good energy resolution. The calorimeter depth is therefore an important design consideration.

Electromagnetic showers are characterised longitudinally by the radiation length (X_0) and have a narrow transverse profile while hadronic showers have a larger lateral spread and a nuclear interaction length (λ) which is, depending on the material, an order of magnitude greater than X_0. The total thickness of the EM calorimeter is $> 22X_0$ in the barrel and $> 24X_0$ in the end-caps. The total thickness of electromagnetic and hadronic calorimeter in nuclear radiation length is 11λ at $\eta = 0$, including 1.3λ from the outer support.

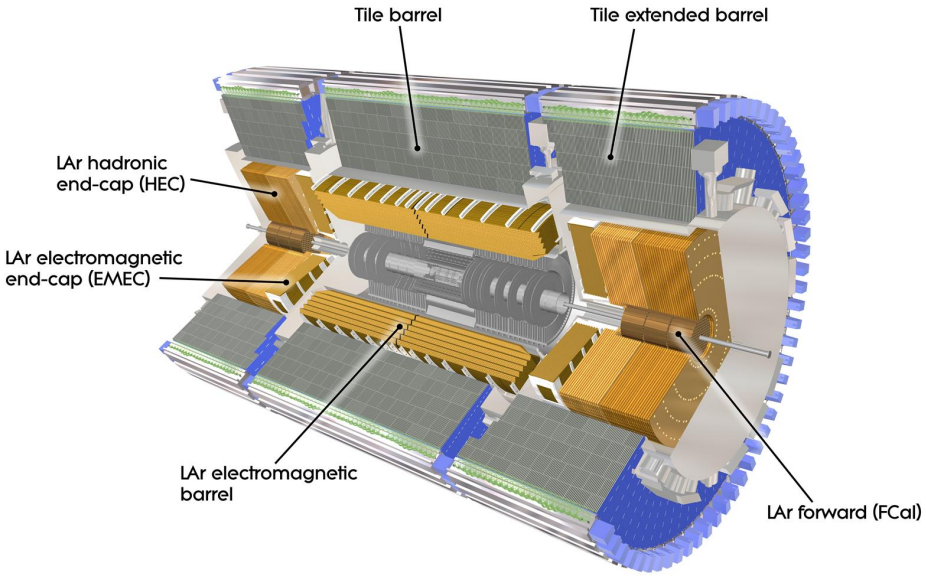

Figure 2.4: Three dimensional view of the ATLAS calorimeter. The liquid argon electromagnetic (LAr EM) calorimeter is divided into a barrel part and two end-caps (EMEC). At outer radii is the hadronic tile barrel and the tile extended barrel. Located just behind the EMEC is the LAr hadronic end-cap calorimeter (HEC) which surrounds the LAr forward calorimeter (FCal).

Electromagnetic (EM) Calorimeter

The EM calorimeter is divided into a barrel part ($|\eta| < 1.475$) and two end-caps ($1.375 < |\eta| < 3.2$), each housed in their own cryostat. The barrel calorimeter consists of two identical half-barrels, separated by a small gap of 4 mm at $z = 0$. Each end-cap calorimeter is mechanically divided into two coaxial wheels: an outer wheel covering the region $1.375 < |\eta| < 2.5$, and an inner wheel covering the region $2.5 < |\eta| < 3.2$.

The EM calorimeter is a liquid argon (LAr) detector with accordion-shaped kapton electrodes and lead absorber plates over its full coverage. The liquid argon was chosen as an active medium because of its intrinsic radiation hardness and good energy resolution. The accordion geometry provides complete ϕ symmetry without azimuthal cracks.

Over the region of the inner detector ($|\eta| < 2.5$), the EM calorimeter is segmented

in three sections in depth. For the end-cap inner wheel, the calorimeter is segmented in two sections in depth and has a coarser lateral granularity than for the rest of the acceptance.

To correct the energy loss due to the material in front of the calorimeter (inner detector, coil and cryostats), a pre-sampler is located in front of the LAr part in the region of $|\eta| < 1.8$. Particles which shower in the material in front of the pre-sampler lead to an increased particle multiplicity which is measured by the pre-sampler. Combining this information with the calorimeter allows an event-by-event measurement of the energy loss.

The readout granularity of all the different layers of the calorimeter is given in [16]. The granularity in η, ϕ in the main ECAL is $\Delta\eta = 0.025$ and $\Delta\phi = 0.025$ in both the barrel and end-caps. The energy resolution for electrons according to test beam data in the barrel is

$$\frac{\sigma(E)}{E} = \frac{10\%}{\sqrt{E(\mathrm{GeV})}} \oplus 0.17\% \tag{2.4}$$

where 10% is the stochastic term and 0.17% is the constant term. The energy response is also linear within ±0.1%. Similar results have been obtained for the end-cap EM calorimeter.

Hadronic Calorimeters

The hadronic calorimeters are subdivided into the tile calorimeter, the LAr hadronic end-cap calorimeters and the LAr forward calorimeter. The tile calorimeter is placed directly outside the EM calorimeter with the barrel covering the region $|\eta| < 1.0$ and the two extended barrels covering the range $0.8 < |\eta| < 1.7$. It is a sampling calorimeter using steel as the absorber and scintillation tiles as the active material. The fractional energy resolution σ_E/E in the tile calorimeter was studied for isolated pions and is according to test beam data [16]:

$$\frac{\sigma(E)}{E} = \frac{56.4\%}{\sqrt{E(\mathrm{GeV})}} \oplus 5.5\%. \tag{2.5}$$

The LAr hadronic end-cap calorimeter (HEC) consists of two independent wheels per end-cap, located directly behind the end-cap electromagnetic calorimeter and

sharing the same LAr cryostats. Similar to the barrel EM calorimeter, LAr technology is used but instead of lead, copper is chosen as the passive material. The energy resolution for isolated pions is according to test-beam data: $\frac{\sigma(E)}{E} = \frac{71\%}{\sqrt{E(\mathrm{GeV})}} \oplus 5.8\%$.

The LAr forward calorimeter (FCal) covers the region of $3.1 < |\eta| < 4.9$. It consists of three modules in each end-cap: the first, made of copper, is optimised for electromagnetic measurements while the other two, made of tungsten, measure predominantly the energy of hadronic interactions. In test beam data, the relative energy resolution of the FCAL is measured as $\frac{\sigma(E)}{E} = \frac{94.2\%}{\sqrt{E(\mathrm{GeV})}} \oplus 7.5\%$.

The combined performance of the barrel LAr electromagnetic and tile calorimeters in test beam data with isolated charged pions was found to be $\frac{\sigma(E)}{E} = \frac{52\%}{\sqrt{E(\mathrm{GeV})}} \oplus 3.1\%$, the result being very close to design specifications.

2.2.3 Muon Spectrometer

The ATLAS muon spectrometer can identify and reconstruct muons completely independently from the other sub-detectors; its layout is shown in figure 2.5. Muons are the only charged particles which are not stopped in the calorimeter and can be cleanly detected in the muon system. The working principle of the muon spectrometer is based on the magnetic deflection of muon tracks in a system of large superconducting magnets, instrumented with separate trigger and high-precision tracking chambers. For good momentum resolution at high energies a large magnetic field over long distances is desirable. A system of three large air-core toroids generates the magnetic field for the muon spectrometer. In the end-cap region, end-cap toroids are inserted in the barrel toroid at each end and lined up with the central solenoid. Each of the three toroids is made of eight coils assembled radially and symmetrically around the beam axis. Contrary to what happens in the inner detector, muons are therefore bent outside the inner detector in the $r - z$ plane.

The muon detector comprises two sub-detectors, one for precision measurements and another with very fast sub-detectors with coarser granularity, used for the online triggering of muon events.

The precision measurements are performed by the Monitored Drift Tube chambers (MDTs), which cover the pseudorapidity region up to $|\eta| = 2.7$ and in the

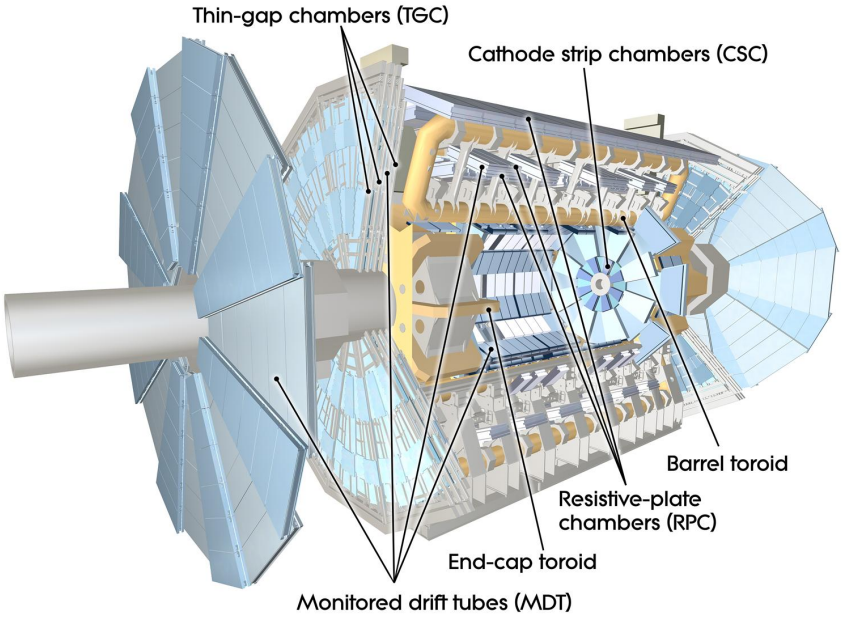

Figure 2.5: Cut-away view of the ATLAS muon system.

forward region of $2 < |\eta| < 2.7$ by Cathode-Strip Chambers (CSCs), used in the innermost tracking layer due to their higher rate and better time resolution.

While the MDT chambers only constrain the muon track in the bending plane (z coordinate) with a precision of 35 μm, the CSCs, being multi-wire proportional chambers with cathode planes segmented into strips in orthogonal direction, provide a measurement both in the r direction of 40 μm precision and in the ϕ direction of 5 mm.

These chambers are complemented by the trigger chambers: Resistive Plate Chambers (RPCs) are used in the barrel ($|\eta| < 1.05$) and Thin Gap Chambers (TGCs) in the end-cap regions ($1.05 < |\eta| < 2.4$). The intrinsic time resolution of these detector components with 1.4 ns for RPCs and 4 ns for TGCs is appropriate for triggering and permits identification of the correct bunch crossing with an accuracy of 99%. The spatial and time resolutions as well as measurements per track of the muon sub-detectors are summarised in table 2.2.

Given the chamber layout of the muon spectrometer, the momentum measurement of a high p_T track will depend on the resolution by which its deviation in the $r - z$ plane in the middle chamber with respect to a straight line, the so-called

Type	Function	Chamber resolution in			Measurements/track	
		z/r	ϕ	time	barrel	end-cap
MDT	tracking	35 μm(z)	-	-	20	20
CSC	tracking	40 μm(r)	5 mm	7 ns	-	4
RPC	trigger	10 mm(z)	10 mm	1.5 ns	6	-
TGC	trigger	$2-6$ mm(r)	3-7 mm	4 ns	-	9

Table 2.2: Resolutions and measurements per track of the muon spectrometer for each chamber type.

sagitta, can be determined. For a high p_T track of 1 TeV, this sagitta will be about 500 μm.

The muon chamber resolution in z using the MDT chambers is better than 10% in the momentum measurements of muons up to 1 TeV, corresponding to the design goals of ATLAS. Measurement of low p_T muons have to be complemented by the measurements in the inner detector, since in general not all muon stations will be reached due to the stronger bending of low p_T particles in the magnetic field.

2.2.4 Forward Detectors

Three smaller detector systems cover the ATLAS forward region, two for determining the luminosity delivered to ATLAS. LUCID (**LU**minosity measurement using **C**erenkov **I**ntegrating **D**etector) is located $\pm$17 m from the interaction point. It detects inelastic $p-p$ scattering in the forward direction and is the main online relative-luminosity monitor for ATLAS. ALFA (**A**bsolute **L**uminosity **F**or **A**TLAS), is at $\pm$240 m, consists of scintillating fibre trackers located inside Roman pots which are designed to approach as close as 1 mm to the beam. The third system, ZDC (**Z**ero-**D**egree **C**alorimeter), plays a key role in determining the centrality of heavy-ion collisions and is located at $\pm$140 m from the interaction point, just beyond the point where the common straight-section vacuum-pipe divides back into two independent beam-pipes.

2.2.5 Trigger System

The ATLAS trigger system is made up of three levels: L1, L2 and the event filter (EF) to efficiently select the events of interest. After the selection of these events, the **d**ata **acq**uisition (DAQ) system transfers the data from the individual sub-detectors to the permanent storage elements for offline reconstruction.

The first level trigger (L1) is a hardware based trigger in contrast to the next two levels which are purely software-based. Together L2 and the event filter are called High Level Trigger (HLT). The first level uses a limited amount of total detector information to make a decision in less than 2.5 μs, reducing the rate to about 75 kHz. The two higher levels access more detector information for a final rate up to 200 Hz with an event size of approximately 1.3 Mbyte.

Trigger Menus

Trigger menus are an important concept of the trigger system. They consist of a series of trigger signatures, combinations of objects which pass different thresholds for different beam energies and luminosities. Depending on the physics they aim to cover, they are grouped together in a coincidence or in a veto. If one or more signatures is satisfied, the event passes the trigger.

Trigger menus are designed to make sure that all interesting physics known and expected is included, but they should also be inclusive to unexpected physics. Trigger menus are constantly evolving in order to achieve the optimal final efficiencies and rejection factors, but they will also be updated during the running of the experiment, once the detector is well understood.

Level 1 Trigger

The L1 trigger performs the initial event selection based on information from the calorimeters and muon detectors. The maximum L1 accept rate which the detector readout systems can handle is 75 kHz (upgradeable to 100 kHz) and the L1 decision must reach the front-end electronics within 2.5 μs after the bunch crossing with which it is associated.

The L1 trigger uses reduced-granularity information from a subset of detectors: the RPCs and TGCs in the muon system and all the calorimeter sub-systems.

The L1 calorimeter trigger (L1Calo) aims to identify high-E_T objects such as electrons and photons, jets and τ-leptons decaying into hadrons, as well as events with large missing energy (E_T^{miss}) or large total transverse energy. Isolation can be required for the electron/photon and τ triggers. This implies that the energetic particle must have a minimum angular separation from any significant energy deposit in the same trigger.

The L1 muon trigger is based on signals in the muon trigger chambers: the RPCs in the barrel and the TGCs in the end-caps. The trigger searches for patterns of hits consistent with high-p_T muons originating from the interaction region.

The output of the calorimeter and muon trigger is passed to the Central Trigger Processor (CTP) which combines the information for different object types and makes the decision according to the trigger menus specifically designed for this level. Trigger menus can be programmed with up to 256 distinct items, each item being a combination of requirements on the input data. The trigger decision is then distributed to the detector front-end and readout systems via the Timing, Trigger and Control (TTC) system. During the time it takes for the trigger decision to be made, all information is stored in pipeline memories.

While the L1 trigger decision is based only on the multiplicity of trigger objects, information about the geometric location of the trigger objects is retained in the muon and calorimeter trigger processors. If the event is accepted by the L1 trigger, this information is sent as a Region of Interest (RoI, a geometrical grouping of detector hits) to the L2 trigger where it is used to seed the selection performed by the HLT.

Level 2 Trigger

The L2 trigger is seeded by the RoIs and uses their information on coordinates, energy and types of signatures to limit the amount of data which must be transferred from the detector readout. The L2 trigger reduces the event rate to below 3.5 kHz with an average event processing time of approximately 40 ms.

The data of an event passed on to the L2 trigger is moved from the pipeline memories to the Read-Out Buffers (ROBs) where they are stored for the whole processing time of L2. Full granularity and full precision data are available from all sub-detectors but only in the RoIs identified by L1. In special cases and only for a small fraction of the events, L2 can access and process data from the full detector with the full granularity and precision within the bandwidth limitations. This applies for example to the processing of all calorimeter cells for an improved calculation of E_T^{miss}.

L2 processes events by running algorithms which are used to identify objects like electrons or jets and determine their properties by grouping together data for each RoI. The sequence of execution of the algorithms is chosen to maximise the physics potential. After each step in the sequence, an algorithm determines whether a given signature is satisfied or not. The processing of any given RoI is stopped as soon as it is clear that it cannot contribute to the selection of the event. The event itself is rejected if none of the signatures in the trigger menu is satisfied.

Event Filter

The EF uses offline analysis procedures on fully-built events to further select events down to a rate which can be recorded for subsequent offline analysis. It reduces the event rate to approximately 200 Hz with an average event processing time of order four seconds and is the last stage of the online selection before the events are transferred to permanent storage. The EF is seeded by the L2 decision and has access to full event data as well as to the full detector geometry with all calibration and alignment information. It uses more sophisticated algorithms which are often similar to the offline reconstruction algorithms.

Chapter 3

Theoretical Framework and Higgs Phenomenology

The Standard Model (SM) [17, 18, 19] of particle physics describes the electromagnetic, weak and strong interactions between all elementary particles. There is one particle predicted by the SM which has not yet been observed, the Higgs boson, which is thought to be the mediator of mass. All physical properties of this particle are predicted by theory, except its mass.

This chapter presents a short overview of the current understanding of elementary particles and fundamental interactions with some emphasis on the Higgs mechanism. The $t\bar{t}H^0(H^0 \rightarrow b\bar{b})$ channel, which is the subject of this thesis, is also presented here. In this thesis, natural units are used, defining $\hbar = 1$ and $c = 1$ (except in Chapter 1).

3.1 The Standard Model - particles and forces

The Standard Model describes the fundamental forces between the elementary particles with Quantum Field Theories. The elementary particles with spin $\frac{1}{2}$ are called *fermions* and are the building blocks of matter. The fermions can be subdivided into two categories and arranged in three generations of progressively more massive doublets. There are six leptons,

$$\begin{pmatrix} \nu_e \\ e^- \end{pmatrix} \begin{pmatrix} \nu_\mu \\ \mu^- \end{pmatrix} \begin{pmatrix} \nu_\tau \\ \tau^- \end{pmatrix} \tag{3.1}$$

and six quarks,

$$\begin{pmatrix} u \\ d \end{pmatrix} \begin{pmatrix} c \\ s \end{pmatrix} \begin{pmatrix} t \\ b \end{pmatrix} \tag{3.2}$$

For each particle there exists an anti-particle with identical mass but opposite quantum numbers.

Additionally, the model contains *vector bosons*, particles responsible for mediating the fundamental interactions:

- the photon γ, the gauge boson for the electromagnetic interaction
- the $W^{\pm}, Z^0$, the three gauge bosons for the weak interaction
- eight gluons, the gauge bosons for the strong interaction

and one *scalar boson*:

- the Higgs boson H, which has not yet been observed.

The Standard Model of particle physics is a special case of a gauge theory, a type of field theory in which the Lagrangian is invariant under a continuous group of local transformations. These local transformations are transformations which are not identically performed at every point in space-time and are referred to as local symmetry or gauge groups.

The requirement of local symmetry places a stringent constraint in the construction of a theory. For local symmetry to be observed, the laws of physics must retain validity when a different transformation is applied at any point in space and time. In order to make a theory invariant with respect to local transformation, a new field has to be added that would compensate for changes from the local transformations. These so-called *gauge fields* arise through the corresponding group generators of the symmetry group and describe the forces of the SM. The quanta of the fields are called *gauge bosons*, they act as carriers of the forces.

The symmetry group of the Standard Model is of the kind $SU(3)_C \otimes SU(2)_I \otimes U(1)_Y$ where $SU(3)_C$ is the *colour* symmetry of strong interactions, $SU(2)_I$ describes the *weak isospin* I for the unified electroweak interactions and $U(1)_Y$ the invariance under *hypercharge* Y transformations. The Lagrangian can be separated into a term for strong interactions $\mathcal{L}_{QCD}$ and a term for electroweak interactions $\mathcal{L}_{EW}$.

Despite its power, the Standard Model in its early form was a theory of massless particles contradicting every day experience. Explicit mass terms in the Lagrangian destroy gauge invariance and make the theory meaningless. However, this can be solved by introducing a scalar field with a quartic potential and by breaking the symmetry of its ground state. This symmetry breaking takes place in the electroweak sector of the Standard Model. In the following sections neutrinos are assumed to be massless, although experimental observations support non-vanishing values for neutrino masses [20].

3.1.1 Strong Interaction

The theory of strong interactions [21, 22, 23] describing the interaction of quarks and gluons is called quantum chromodynamics (QCD). It is based on colour charges and described by the $SU(3)_C$ gauge symmetry.

Interactions between coloured quarks are mediated by eight massless gauge bosons, the gluons. The range of the strong interaction is limited to $\sim 10^{-18}$m. At long distances, QCD becomes strongly interacting and perturbation theory breaks down. In this confinement regime, the coloured partons are transformed into colourless hadrons, a process called *hadronisation*. The *Lund string model* [24] is a phenomenological model of hadronisation: The self-interaction of gluons via 3-gluon and 4-gluon vertices causes the strength to increase with distance. As quarks are separated, the potential energy between them increases until it is favourable for the field to form new quark-anti-quark pairs, continuing until all quarks are bound within colourless objects, either *mesons* ($q\bar{q}$) or *baryons* (qqq).

Since the strong interaction does not discriminate between different quark flavours, QCD has approximate flavour symmetry, which is broken by the differing masses of the quarks. The Lagrangian, describing the dynamics of the quarks and gluons is given by:

$$\mathcal{L}_{QCD} = i \sum_f \bar{q}_f \gamma^\mu D_\mu q_f - \frac{1}{4} G^i_{\mu\nu} G^{\mu\nu}_i, \tag{3.3}$$

where q_f is a colour triplet of quarks with flavour f, γ^μ are the Dirac matrices and

the covariant derivative D_μ is defined as

$$D_\mu = \delta_\mu - ig_3 \frac{\lambda_i}{2} G^i_\mu \tag{3.4}$$

with the $SU(3)_C$ coupling constants g_3. The tensor fields $G_{\mu\nu}$ are defined as

$$G_{i,\mu\nu} = \delta_\mu G_{i,\nu} - \delta_\nu G_{i,\mu} + g f_{ijk} G_{j,\mu} G_{k,\nu}, \tag{3.5}$$

where $G_{i,\nu}$ are the eight gluon fields, λ_i the generators of $SU(3)_C$, the so-called Gell-Mann matrices and f_{ijk} the structure constants of the symmetry group.

3.1.2 Quantum Electrodynamics

The first and simplest local gauge theory was quantum electrodynamics (QED) describing the electromagnetic force and based on the $U(1)_Q$ symmetry. The interaction of a spin-$\frac{1}{2}$ fermion field Ψ of mass m_f with the electromagnetic field of infinite range, the vector potential A_μ, is described by the Lagrangian

$$\mathcal{L}_{QED} = \bar{\Psi}(i\gamma^\mu D_\mu - m_f)\Psi - \frac{1}{4} F_{\mu\nu} F^{\mu\nu} \tag{3.6}$$

with the tensor of the electromagnetic field strength $F_{\mu\nu} = \delta_\mu A_\nu - \delta_\nu A_\mu$ corresponding to the kinetic energy and the covariant derivative $D_\mu = \delta_\mu - ieA_\mu Q$, with the electric unit charge e and the charge operator Q ($Q(\text{electron}) = -1$).

The Lagrangian is invariant under the local transformation

$$\Psi(x) \rightarrow \exp^{i\alpha(x)Q} \Psi(x), \tag{3.7}$$

where A_μ transforms as

$$A_\mu(x) \rightarrow A_\mu(x) + \frac{1}{e} \delta_\mu \alpha(x). \tag{3.8}$$

$\alpha(x)$ is a local phase depending on space and time in a completely arbitrary way without relevance for observable quantities. Local gauge invariance requires the photon field A_μ to be massless because adding an explicit mass term of the form $m_\gamma A_\mu A^\mu$ breaks the gauge invariance. The Abelian nature of $U(1)_Q$ does not allow any self-interaction terms for photons.

3.1.3 Weak Interaction

The charged weak currents do not distinguish left-handed charged leptons and their associated left-handed neutrino. They can therefore be grouped into a doublet $\chi_L = \binom{\nu}{l^-}$ which transforms under the symmetry group $SU(2)_L$ (L for left-handed). The associated inner symmetry is the third component of the weak isospin. The right-handed leptons remain singlets, l_R. The Lagrangian

$$\mathcal{L}_W = i\bar{\chi}_L \gamma^\mu D_\mu \chi_L + i\bar{e}_R \gamma^\mu \delta_\mu e_R \tag{3.9}$$

is invariant under transformations $\chi_L \rightarrow \exp^{\frac{i}{2}\vec{\alpha}(x)\cdot\vec{\tau}} \chi_L$, if the derivative takes the form

$$D_\mu = \delta_\mu + i\frac{g}{2}\vec{\tau} \cdot \vec{W}_\mu(x). \tag{3.10}$$

The Pauli matrices τ_i are generators of $SU(2)$ and g is a coupling constant. Local gauge invariance introduces three vector fields W_1, W_2, W_3 which can be associated with the weak gauge bosons. W_1 and W_2 mix to the physical W bosons:

$$W_\mu^\pm = \frac{1}{\sqrt{2}}(W_\mu^1 \mp W_\mu^2). \tag{3.11}$$

The third component W_3 could be associated with the Z^0 boson, but the next section will show that the situation is slightly more complicated.

3.1.4 Electroweak Interaction

The electroweak (EW) theory is a unified gauge theory of the electromagnetic and weak forces for energies above ~ 100 GeV and based on the $SU(2)_L \otimes U(1)_Y$ gauge symmetry group. The conserved quantity of $SU(2)_L$ is the third component of the weak isospin and the conserved quantity of $U(1)_Y$ is the hypercharge Y, which is related to the electric charge and the weak isospin:

$$Q = \frac{Y}{2} + I_3. \tag{3.12}$$

The $SU(2)_L$ symmetry group is non-Abelian, therefore self-interaction terms are possible for the weak gauge bosons, but not for the electromagnetic force carriers of the Abelian group $U(1)_Y$.

The Lagrangian is given by Eq. 3.9, but the covariant derivative is now

$$D_\mu = \delta_\mu + ig\frac{\vec{\tau}}{2}\vec{W}_\mu + ig'\frac{Y}{2}B_\mu, \tag{3.13}$$

with the coupling constants g, g'. The Lagrangian is invariant under local gauge transformations of the form

$$\chi_L \rightarrow e^{i(\vec{\alpha}(x)\cdot\vec{\tau}+\beta(x)Y)/2}\chi_L, \tag{3.14}$$

$$e_R \rightarrow e^{\beta(x)Y/2}e_R. \tag{3.15}$$

Multiplying out the derivative, the Lagrangian becomes

$$\begin{aligned}\mathcal{L} &= \bar{\chi}_L\gamma^\mu\left[i\delta_\mu - g\frac{1}{2}\vec{\tau}\cdot\vec{W}_\mu - g'\frac{Y}{2}B_\mu\right]\chi_L \\ &\quad \bar{e}_R\gamma^\mu\left[i\delta_\mu - g'\frac{Y}{B_\mu}\right]e_R - \frac{1}{4}\vec{W_{\mu\nu}}\cdot\vec{W^{\mu\nu}} - \frac{1}{4}\vec{B_{\mu\nu}}\cdot\vec{B^{\mu\nu}},\end{aligned} \tag{3.16}$$

where $B_{\mu\nu} = \delta_\mu B_\nu - \delta_\nu B_\mu$ and $W_{\mu\nu} = \delta_\mu\vec{W}_\nu - \delta_\nu\vec{W}_\mu + ig\vec{W}_\mu \times \vec{W}_\nu$. The first two terms describe the kinetic energy of the fermions and their interaction with the gauge fields. The last two terms are the kinetic energy and the self-interaction of the gauge fields. It is the mixing between these four gauge fields that give rise to the photon field A_μ, the Z boson field Z_μ and the charged $W^\pm$ boson fields via

$$A_\mu = \sin\Theta_W W_\mu^3 + \cos\Theta_W B_\mu, \tag{3.17}$$

$$Z_\mu = \cos\Theta_W W_\mu^3 - \sin\Theta_W B_\mu, \tag{3.18}$$

$$W_\mu^\pm = \frac{W_\mu^1 \mp iW_\mu^2}{\sqrt{2}}, \tag{3.19}$$

where Θ_W is the weak mixing angle. The quanta of these fields are the gauge bosons $W^\pm$, Z^0 and γ.

The formalism presented here so far has an important drawback: It does not allow explicit mass terms for gauge bosons and fermions. Mass terms in the Lagrangians break gauge invariance and the theory is no longer renormalisable. But experiments demonstrate that the gauge bosons $W^\pm$ and Z^0 and fermions like the τ lepton and top quark have large masses, so Eq. 3.16 is not an acceptable representation of the phenomenology observed in nature. Only the electromagnetic sector of the $U(1)$ subgroup is described correctly, since the photon is indeed massless. The

next section describes how the introduction of a new fundamental scalar field helps in retaining the concept of local gauge invariance whilst giving mass to the weak gauge boson and the fermions.

3.2 The Higgs Mechanism and Mass Generation

The Lagrangian introduced so far describes a theory of massless particles, which is in clear contradiction with experimental observations. When introducing particle masses, the original gauge invariance of the Lagrangian has to be preserved. This is done by the so-called *spontaneous symmetry breaking*.

Spontaneous symmetry breaking occurs when a system which is symmetric in itself is exposed to an external force and a specific outcome occurs. A commonly used example is a ball sitting on top of a hill. The ball is symmetric in itself, but as soon as some perturbing interaction with the ball is carried out, the ball will roll down the hill in a specific direction, causing the symmetry to break because the direction in which the ball rolled has a feature that distinguishes it from all other directions.

In the SM the introduction of a new fundamental scalar field helps in retaining the concept of local gauge invariance, where the spontaneous symmetry breaking from $SU(3)_C \otimes SU(2)_L \otimes U(1)_Y$ to $SU(3)_C \otimes U(1)_Q$ provides masses to the $W^{\pm}$ and Z^0 bosons, while the photon does not acquire any mass. This is called the Higgs mechanism [25, 26].

The new field introduced by the Higgs mechanism is a doublet of complex scalar fields with appropriate potential. Interactions of fermions and gauge bosons with this field manifest themselves as masses of the particles. The simplest representation of a scalar field, known as the Higgs field Φ is

$$\Phi = \begin{pmatrix} \Phi^+ \\ \Phi^0 \end{pmatrix} = \begin{pmatrix} \Phi_3 + i\Phi_4 \\ \Phi_1 + i\Phi_2 \end{pmatrix}, \qquad \text{with } \Phi_i \text{ real}, Y = 1,\ I_W = \frac{1}{2}. \tag{3.20}$$

By imposing gauge invariance, the symmetry breaking can be described by a La-

grangian

$$\mathcal{L}_{Higgs} = (D_\mu\Phi)^\dagger(D_\mu\Phi) + V(\Phi) \qquad \text{with} \tag{3.21}$$

$$V(\Phi) = -\mu^2\Phi^\dagger\Phi - \lambda(\Phi^\dagger\Phi)^2, \qquad \mu^2, \lambda \in \mathbb{R}, \tag{3.22}$$

$$D_\mu = \delta_\mu + \frac{1}{2}ig\vec{\tau}\vec{W}_\mu + \frac{1}{2}ig'YB_\mu \tag{3.23}$$

The values of μ^2 and λ in the Higgs potential V(Φ) are free real parameters. λ is chosen positive to make the total field energy bounded from below. If μ^2 is chosen positive, the potential has its minimum for $\Phi = 0$, whereas if μ^2 is negative, the minimum is not a single point but a circle in the complex plane as shown in Figure 3.1. The field $\Phi_{1,2}^{min}$ in the minimum of the potential is then given by

$$\Phi_{1,2}^{min} = \sqrt{\frac{-\mu^2}{2\lambda}}\exp^{i\Theta}, \qquad 0 \leq \Theta \leq 2\pi. \tag{3.24}$$

This implies that the state of minimum energy, the vacuum state, is not unique but degenerate. The equations of motion are obtained by expanding the Lagrangian around the minimum, and so one point Φ^{vac} from Eq. 3.24 must be fixed. The common choice is to set $\Theta = 0$, which leads to

$$\Phi_{1,2}^{vac} = \sqrt{\frac{\mu^2}{2\lambda}} := \frac{v}{\sqrt{2}}, \tag{3.25}$$

with the vacuum expectation value v. Choosing one point from the degenerated minimum breaks the symmetry of the potential. The Higgs field must take the form $\Phi_1 = v/\sqrt{2}, \Phi_2 = \Phi_3 = \Phi_4 = 0$, as non-vanishing values for Φ_2, Φ_3, Φ_4 would result in additional unphysical massless fields, associated with Goldstone bosons, which can not be identified with existing particles [27]. Also, the expectation value of the upper component Φ^+ must be zero in order to leave $U(1)_Q$ unbroken.

Small excitations around Φ^{vac} can be written as $\Phi = \frac{1}{\sqrt{2}}\binom{0}{v+H(x)}$ with the real field $H(x)$ and, when inserted into Eq. 3.22, one obtains a part (among many others) that describes a scalar Klein-Gordon field H

$$\mathcal{L}_{KG} = \frac{1}{2}\delta^\mu H\delta_\mu H - \lambda v^2H^2 - \lambda vH^3 - \frac{1}{4}\lambda H^4. \tag{3.26}$$

with mass $m_H = v\sqrt{2\lambda}$ and self coupling according to H^3 and H^4 terms. Mass terms for fermions must be introduced 'by hand' via the Yukawa couplings λ_f of the

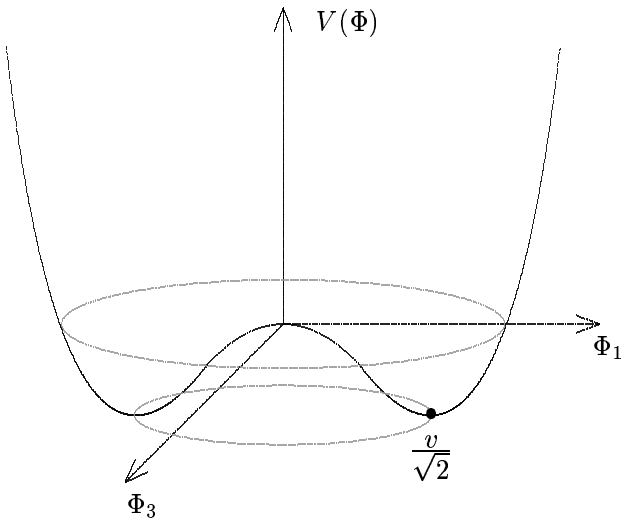

Figure 3.1: The Higgs potential shown as a function of two out of the four field components Φ_i.

Higgs field to fermions, shown here for the first generation of leptons and quarks:

$$\mathcal{L}_{Yukawa} = \lambda_e \chi_e \Phi_{e_R} + \lambda_u \bar{q} \tilde{\Phi} u_R + \lambda_d \chi_d \Phi_{d_R} + h.c., \tag{3.27}$$

where $q = (u, d)$ and $\tilde{\Phi} = i\tau_2 \Phi^*$ is the charge conjugate field which gives mass to quarks with $I_W^3 = +\frac{1}{2}$.

The masses of the fundamental particles are all proportional to the vacuum expectation value of the Higgs field:

$$\begin{aligned} m_{W^\pm} &= v\frac{g}{2}, \\ m_{Z^0} &= v\frac{\sqrt{g^2 + g'^2}}{2}, \\ m_f &= v\frac{\lambda_f}{\sqrt{2}}, \\ m_{H^0} &= v\sqrt{2\lambda} = \sqrt{2}\mu. \end{aligned} \tag{3.28}$$

The vacuum expectation value is related to Fermi's constant:

$$\frac{G_F}{\sqrt{2}} = \frac{1}{2v^2} \rightarrow v = (\sqrt{2}G_F)^{-1/2} \approx 246\,\mathrm{GeV}. \tag{3.29}$$

The Standard Model now gives an acceptable description of what is observed to date. It is a renormalisable quantum gauge theory with massive fermions and

massive weak gauge bosons. The Higgs boson H^0 is a consequence of the mechanism which breaks electroweak symmetry. All its properties are precisely predicted by the model except for its mass m_{H^0}. The following sections describe which bounds can be set on the mass from theory and from direct searches.

3.3 Constraints on the Higgs Boson Mass

3.3.1 Theoretical Bounds

Several theoretical constraints can be derived from assumptions on the energy range in which the SM is valid before perturbation theory breaks down and new phenomena should emerge. These include constraints from unitarity in scattering amplitudes, triviality and stability of the electroweak vacuum. For a more detailed discussion see [28].

Unitarity

The unitarity argument applies to the scattering process of longitudinal gauge bosons $V_L V_L \to V_L V_L$ where V is either a $W^\pm$ or a Z^0 boson in the high energy limit $s \gg m_V^2$. Divergences in the scattering amplitudes of longitudinal gauge bosons require the existence of new physics like the Higgs boson and set in this case an upper bound on the Higgs mass, depending on the scattering process. For $W_L^+ W_L^- \to W_L^+ W_L^-$ a limit of $m_H < 870$ GeV can be found, for the channel $W_L^+ W_L^- \to Z_L Z_L$ the limit can be tightened to $m_H < 710$ GeV.

Similar bounds can also be calculated for other scattering processes, they all constrain the Higgs boson mass to values below 1 TeV [29]. However, these bounds have to be taken with care as they are obtained from high energy limits of pertubative expansions.

Triviality and Vacuum Stability

Another bound on the Higgs mass arises from loop corrections to the classical Higgs potential, due to the dependence of the couplings and masses which appear in the SM Lagrangian. This is also the case of the quartic Higgs self-coupling λ which

monotonically increases with the energy scale Q [30, 31]. This leads to non-trivial constraints on this coupling and therefore on the Higgs boson mass.

The general triviality argument states that for the scalar sector of the SM to remain perturbative at all scales one needs to have a coupling $\lambda = 0$. This means in the SM that the Higgs boson is massless, rendering the theory trivial, i.e. non interacting. However, this argument can be viewed in a different way and an energy cut-off Λ_C can be introduced below which the self coupling λ remains finite. The choice of Λ_C sets a bound on the Higgs mass. In particular, if the cut-off is set at the Higgs boson mass itself, $\Lambda_C = m_H$, the requirement that the quartic coupling remains finite implies that $m_H \geq 700$ GeV. But if λ is too large, one cannot use perturbation theory anymore and this constraint is lost. However, from simulations of gauge theories on the lattice, where the non perturbative effects are properly taken into account, it turns out that one obtains the bound $m_H < 640$ GeV, which is in a remarkable agreement with the bound obtained by naively using perturbation theory.

So far, only the contribution of the Higgs boson itself has been included in the running of the quartic coupling λ, which is justified in the regime where λ is large. For a complete treatment of the running coupling, the contributions from fermions and gauge bosons have to be included. Since the Higgs boson couplings are proportional to the particle masses, only the contribution of top quarks and massive gauge bosons need to be considered. Particularly the top quark contribution can become dominant if the coupling λ is too small, driving it into a negative value which would lead to a scalar potential $V(Q) < V(v)$. That would mean that the vacuum is not stable anymore because it has no minimum. The stability argument requires a scalar potential which is bounded from below and therefore keeps λ positive. This puts a constraint on the Higgs boson mass in the sform of a lower bound, which depends on the value of the cut-off Λ_C, i.e. for $\Lambda_C \sim 10^3$ GeV and $m_H \gtrsim 70$ GeV.

The constraints provided by both the triviality and vacuum stability bounds are shown in Figure 3.2. Choosing Λ_C to be the Grand Unification scale $\Lambda_{GUT} \sim 10^{16}$ GeV, results in a bound on the Higgs boson mass of $130\ \text{GeV} \lesssim m_{H^0} \lesssim 180\ \text{GeV}$.

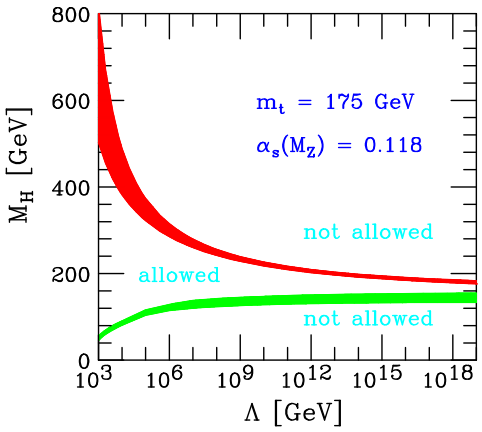

Figure 3.2: The triviality (upper) and vacuum stability (lower) bound on the Higgs boson mass as a function of the new physics energy scale Λ. Taken from Ref. [28].

3.3.2 Experimental Constraints

Indirect Bounds from High Precision Measurements

The Higgs boson contributes via loop diagrams to virtual corrections of fundamental parameters of the SM, like the mass of the W and Z boson, various leptonic and hadronic asymmetries and many other electroweak observables. Many of these parameters have been measured with high precision, so a global fit to these electroweak observables with the Higgs boson mass as a free parameter can result in an indirect measurement of m_{H^0}. The dependence on the Higgs boson mass in electroweak observables is typically logarithmic, so the precision with which the Higgs mass can be determined is limited.

The χ^2 of the electroweak fit is shown in Figure 3.3 (left). The obtained value of the SM Higgs boson mass is $m_{H^0}^{fit} = 89^{+35}_{-26}$ GeV at a 68% Confidence Level (CL) [2]. The fitted value of m_{H^0} is very sensitive to the top quark mass. The global electroweak fit in terms of predicted top quark and W boson masses is shown in a two-dimensional correlation plot in Figure 3.3 (right), together with the correlated Higgs boson mass values.

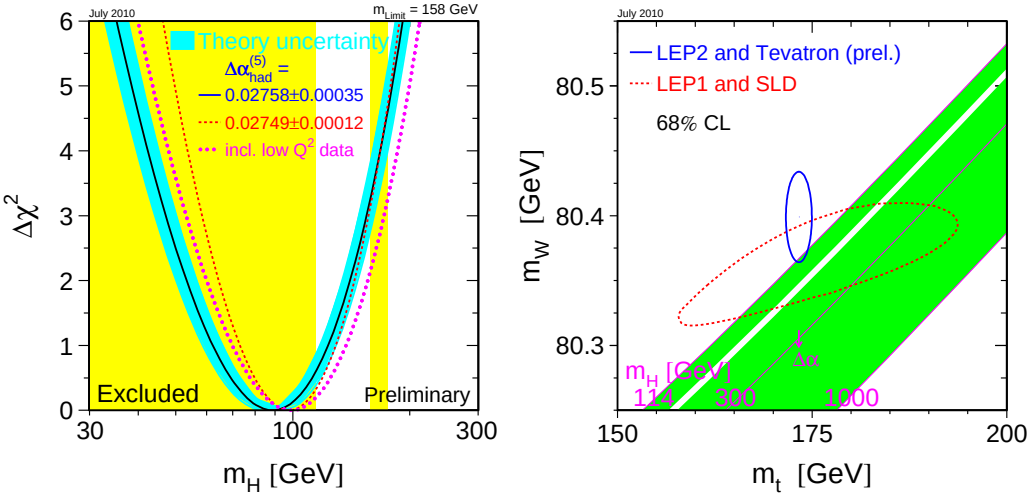

Figure 3.3: Left: The χ^2 distribution of the global fit to parameters of the Standard Model as a function of the Higgs mass m_{H^0}. Taken from Ref [2]. Right: Correlation between the top quark and W boson mass in the electroweak fit, compared with the actual world average (68% confidence level curves, in red for LEP1 and SLD, in blue for LEP2 and Tevatron). The contour lines at $\pm 1\sigma$ with the corresponding values for the Higgs boson mass are also shown. Taken from Ref [2].

Bounds from Direct Searches

At present, the best experimental lower limit on the mass of the SM Higgs boson is from direct searches at LEP2 [1]. The region below $m_{H^0} = 114.4$ GeV was excluded at 95% confidence level, while recent searches at the Tevatron have excluded a Higgs boson mass around the WW mass threshold [32] of $m_{H^0} = 160 - 170$ GeV with 95% confidence level [33] as can be seen in Figure 3.4. The actual exclusion limits, normalised to the expected SM cross-section are shown in Figure 3.4.

3.4 Higgs Phenomenology

One of the main goals of the LHC is to continue the search for the Higgs boson over the full range of possible masses. Precision electroweak measurements indicate that the Higgs mass should be close to the current experimental lower limit [34].

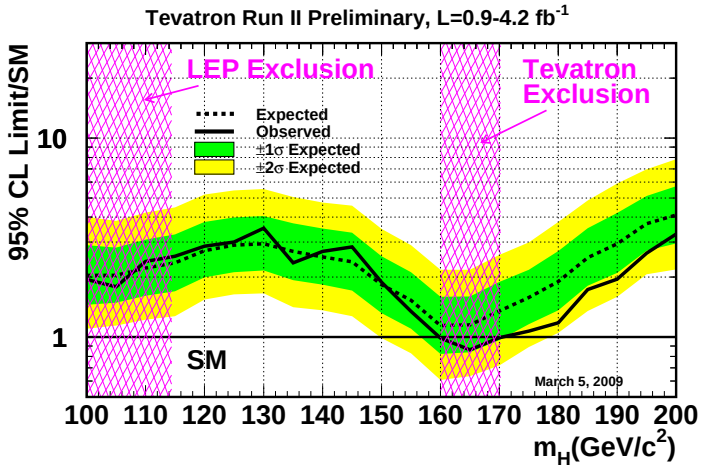

Figure 3.4: Exclusion limits on the presence of a Higgs boson at 95% confidence level, normalised to the expected SM cross-section, as a function of the Higgs boson mass, corresponding to the last updated results from the Tevatron experiments. The full black line shows the actual limit, while the dashed one shows the expected sensitivity of the experiments. It is surrounded by 1 and 2σ bands, showing the 68% and 95% probability regions where the limits can fluctuate, in the absence of signal. The pink band on the left shows what mass range of the Higgs boson has been excluded in the past by the LEP II experiments, while the one on the right is the Tevatron exclusion region. The vertical axis has units of the "times the SM" limits. This means that an exclusion at i.e. 5 times the SM for a mass of 130 GeV implies that a Higgs boson production with a rate five times higher than what the SM predicts is excluded by the experiment; an exclusion of 1.0 or less means that Standard Model Higgs boson is ruled out in the corresponding mass range. Taken from Ref. [32].

This mass range is one of the most challenging for ATLAS with several different production and decay modes. One of these channels involves the Higgs production with an associated top quark pair, where the Higgs boson decays to b quarks. The $t\bar{t}H^0(H^0 \rightarrow b\bar{b})$ channel can therefore contribute to a discovery in the low mass range. Once the Higgs boson has been discovered, it will be important to measure its properties in order to make sure that what has been observed does really correspond to the SM Higgs boson. These properties include, amongst others, a more precise

determination of the Higgs boson mass, of the width of the Higgs boson resonance and the determination of the Higgs boson couplings. The $t\bar{t}H^0(H^0 \rightarrow b\bar{b})$ channel is the only channel in the low mass range to provide a measurement of the directly top-Higgs Yukawa coupling.

3.4.1 Production Modes at the LHC

At the LHC design centre-of-mass energy of $\sqrt{s} = 14$ TeV, the probability to extract a gluon out of a proton (as described by the gluon PDF) is significantly higher than the corresponding probability to extract a quark or antiquark. This is the reason why in general processes initiated by gluons are significantly enhanced with respect to processes initiated by quarks or antiquarks.

The Higgs boson production at the LHC proceeds via four dominant production mechanisms (gluon fusion, vector boson fusion, Higgs-strahlung, and associated production with a $t\bar{t}$ pair) and corresponding example Feynman diagrams are shown in Figure 3.5. Their cross-sections, assuming the nominal centre-of-mass energy of 14 TeV, are shown in Figure 3.6 (right).

Due to the heavy top-quark loop, the loop induced gluon-gluon fusion is the leading production mode at the LHC, followed by the weak boson fusion, $q\bar{q} \rightarrow q\bar{q}H$, where the Higgs boson is produced in association with two forward jets with large rapidity gap between them ($q\bar{q} \rightarrow VH$, $V = W, Z$). With descending cross-section, these processes are followed by the Higgs boson production in association with a W or a Z boson are called Higgs-strahlung and the associated production with a $t\bar{t}$ pair ($gg \rightarrow t\bar{t}H$).

3.4.2 Higgs Decays

The Higgs boson is an unstable particle and can only be detected through its decay products. It couples directly to various particles leading to several decay channels. The branching ratio $BR(H \rightarrow f)$, the fraction of Higgs bosons decaying into a certain decay channel, depends on the Higgs boson mass m_H and is shown in Figure 3.6 (left).

At low Higgs boson masses the decay to a $b\bar{b}$ pair dominates with a BR of 67.7%

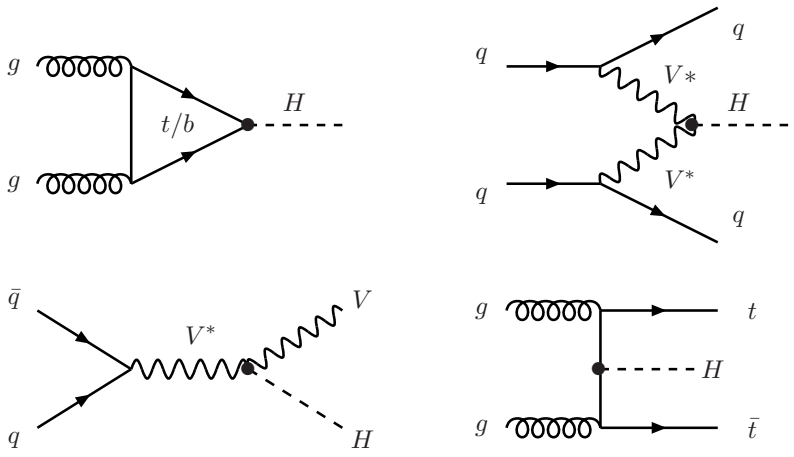

Figure 3.5: The dominant SM Higgs boson production modes at the LHC: gluon fusion (top left), vector boson fusion (top right), Higgs-strahlung (bottom left) and associated production with a $t\bar{t}$ quark pair (bottom right).

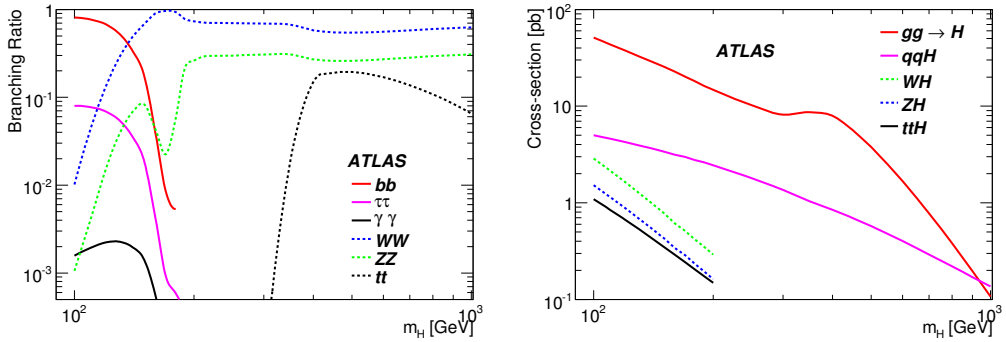

Figure 3.6: Left: Branching ratio of the Higgs boson decaying in the different possible final states as a function of the Higgs boson mass m_H. Right: Cross-sections for the main Higgs boson production modes at the LHC computed at NLO as a function of the Higgs boson mass. Taken from Ref. [5].

for a Higgs boson mass $m_H = 120$ GeV, followed by the $H \to \tau\tau$ channel with a BR of 6.9%. Although the $H \to \gamma\gamma$ decay channel has a very low branching ratio (BR $\approx$ 0.2% for $m_H = 120$ GeV), a signal extraction in the presence of very large continuum backgrounds is possible due to the excellent experimental mass resolution. The Higgs boson branching ratios for $H \to W^+W^-$ and $H \to ZZ$ at low Higgs boson masses

are 13.3% and 1.5%, respectively. The decay to a gluon pair, $H \to gg$ has a BR of $\approx 10\%$ but is impossible to separate from the huge QCD multi-jet background at a hadron collider and is therefore not considered.

At high Higgs masses , the dominant decay modes are the decays into pairs of electroweak gauge bosons ($H \to W^+W^-$, ZZ), in particular for Higgs boson masses above the $2m_W$, $2m_Z$ thresholds. Above $2m_t$, the decay channel $H \to t\bar{t}$ is also significant.

In the intermediate region below the $2m_W$ threshold, decays into WW^* or ZZ^*can occur. These channels are important due to the large HWW and HZZ couplings, though they are suppressed by the fact that one of the two W or Z bosons are off-shell[1].

3.4.3 Discovery Potential with the ATLAS Experiment

For Higgs boson masses below $m_H \approx 130$ GeV the discovery sensitivity has to rely on the combination of different channels, in particular $q\bar{q}H \to q\bar{q}\tau^+\tau^-$ and $H \to \gamma\gamma$. To discover a Higgs boson in the low mass region, a higher amount of integrated luminosity may be needed to claim a 5σ discovery than in the higher mass regions.

In the intermediate mass region of $130 < m_H < 450$ GeV, an integrated luminosity of 10 fb^{-1} is sufficient for a discovery. Here the most significant channels are $H \to W^+W^-$ both in gluon and vector boson fusion and $H \to ZZ$. It should be noted that two important Higgs boson channels, $H \to WW \to (e\nu e\nu, \mu\nu\mu\nu)$ [35], have not yet been considered in the combination.

Figure 3.7 shows the expected significance of a Higgs discovery for the various channels which have been studied, assuming a centre-of-mass energy of $\sqrt{s} = 14$ TeV. The channels considered for the combination are $H \to \gamma\gamma$, $H \to ZZ^* \to 4l$, $H \to \tau\tau$ and $H \to WW \to e\nu\mu\nu$.

The amount of collected data needed discover as well as to exclude the Higgs boson versus its mass is shown in Figure 3.8 .

[1]* denoting an off-mass-shell boson

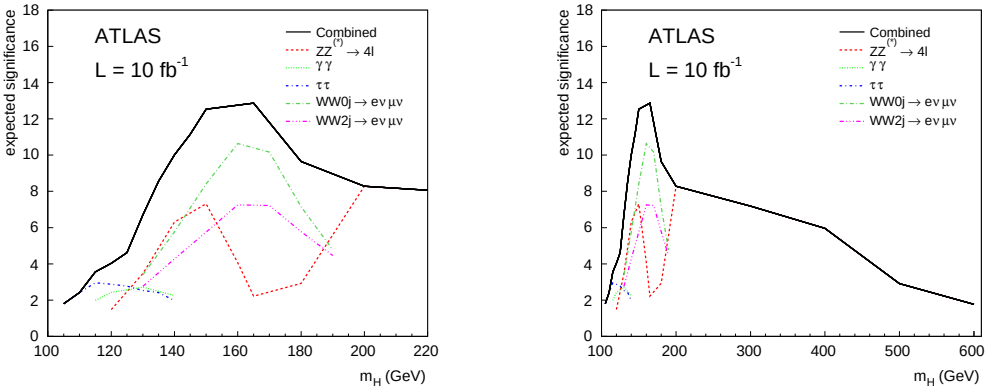

Figure 3.7: ATLAS discovery potential of a SM Higgs boson as a function of the Higgs boson mass, corresponding to an integrated luminosity of 10 fb^{-1}, for the low mass range (left) and up to 600 GeV (right). Taken from Ref [5].

3.4.4 The $t\bar{t}H^0(H^0 \to b\bar{b})$ Channel

For a light Higgs boson in the low mass range up to $m_H \leq 135$ GeV, the decay mode with the highest branching fraction is $H^0 \to b\bar{b}$. It will not be possible to observe this decay channel in the dominant direct production $gg \to H^0$ due to the huge QCD backgrounds. However, the $b\bar{b}$ final state can be observed in the associated production of a Higgs boson with a W or Z boson or a pair of top quarks. The $t\bar{t}H^0(H^0 \to b\bar{b})$ channel is one of the channels that could be added to the low mass combination mentioned in Section 3.4.3.

Signal Process

At the LHC, the production of $t\bar{t}H^0$ is dominated by gluon-gluon interaction (90%) whereas the quark-antiquark interaction contributes to only 10%. For a Higgs boson mass between 115 GeV and 130 GeV the production cross-section times branching ratio to $b\bar{b}$ varies between roughly 0.4 and 0.3 pb at leading order.

The top quarks decay almost exclusively into Wb. Therefore the final states can be classified according to the decays of the W bosons. W bosons decay hadronically in about 2/3 of all cases, and into a lepton and neutrino in about 1/3 of all cases. Table 3.1 lists the relevant branching ratios.

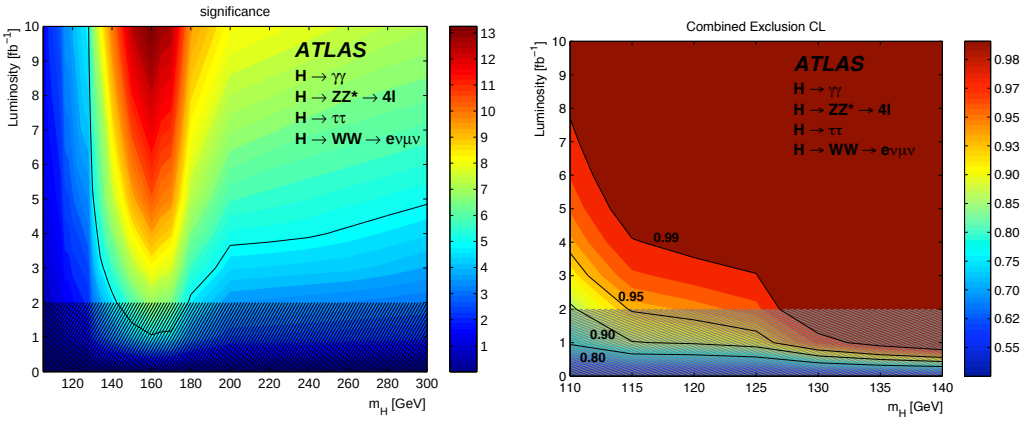

Figure 3.8: Left: Significance contours for different SM Higgs masses and integrated luminosities. The thick curve represents the 5σ discovery contour. Right: The expected luminosity required to exclude a Higgs boson with a mass m_H at a confidence level given by the corresponding colour. In both plots, the hatched area below 2 fb^{-1} indicates the region where the approximation used in the combination are not accurate, although they are expected to be conservative. Taken from Ref [5].

Process	Branching ratio
$t^+ \to Wb$	$> 99.8\%$ (SM prediction)
$W^+ \to l^+\nu$	$(10.68 \pm 0.12)\%$ per lepton family
$W^+ \to$ hadrons	$(67.96 \pm 0.35)\%$

Table 3.1: Branching ratios of top quarks and W bosons [36].

The all-hadronic channel has therefore the highest branching fraction with a value of 43% but the purely hadronic multi-jet final state with moderate transverse momentum of the jets does not allow easy triggering. Only tight requirements on the transverse jet momentum and on the jet multiplicity could lead to a reasonable rate in the first level of the trigger but these requirements come at the expense of the signal efficiency.

The fully leptonic final state with the presence of two isolated leptons is a simpler signature to trigger on. But the branching fraction is very low with a value of 5% (only considering $l = e, \mu$) and the two neutrinos prevent the reconstruction of the

top quarks.

To have a handle for triggering $t\bar{t}H^0$ events, the semileptonic final state is a good compromise with a branching fraction of 28%(only considering $l = e, \mu$). The experimental signature consists of one energetic isolated lepton, a high jet multiplicity with 6 jets, 4 or which are b-jets) and missing transverse energy from the neutrino. An example Feynman diagram is shown in Figure 3.9. In this thesis, only the semileptonic $t\bar{t}H^0$ channel will be investigated.

Background Processes

The main background to the signal process arises from QCD processes with a top-quark pair. Given the high jet multiplicity in the signal process of at least 6 jets, only $t\bar{t}$ events with at least two additional jets from initial or final state gluon radiation contribute. Most of the additional jets are dominated by light flavours, therefore requiring four b-jets in the final state can effectively suppress large parts of this background.

The irreducible background arises from $t\bar{t}b\bar{b}$ production either via QCD or electroweak (EW) interaction with a total cross-section of the order of 9 pb. Figure 3.10 and Figure 3.11 show some of the Feynman diagrams of the QCD and EW production mechanism respectively. Although the QCD production cross-section is ten times larger than the EW production, the EW $t\bar{t}b\bar{b}$ background can contaminate the signal regions due to the large momenta of the b-jets not coming from the $t\bar{t}$ system. Their invariant mass is typically close to the Z boson mass.

Although having a cross-section about 60% higher than the $t\bar{t}b\bar{b}$ production, the $t\bar{t}c\bar{c}$ production is considered negligible as a background for $t\bar{t}H^0$ due to c-jet rejection which is possible when b-tagging jets [5] (see Section 4.4.4).

Other backgrounds are W+jets, tW production and QCD multi-jet production. The W plus 2 jets background has a large inclusive cross-section of about 1200 pb per lepton flavour [37], but it has been shown [38] that this contribution is negligible as long as four b-tags are required. The same applies for the tW background with a cross-section of 9.5 pb [39]. Even when four b-jets are requested in the event, contamination via QCD $b\bar{b}b\bar{b}$ production, which has a cross-section of a few hundred

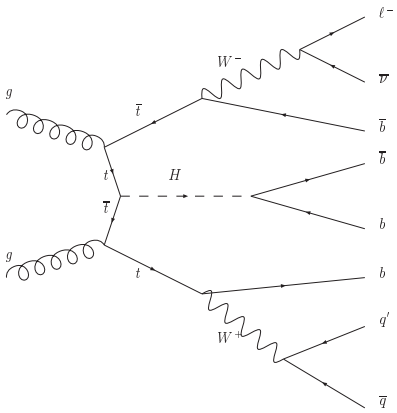

Figure 3.9: Example Feynman diagram of the semileptonic signal process $t\bar{t}H^0(H^0 \to b\bar{b})$.

nb [40], is still possible. But the reconstruction of the $t\bar{t}$ system allows a certain degree of safely against non-top backgrounds.

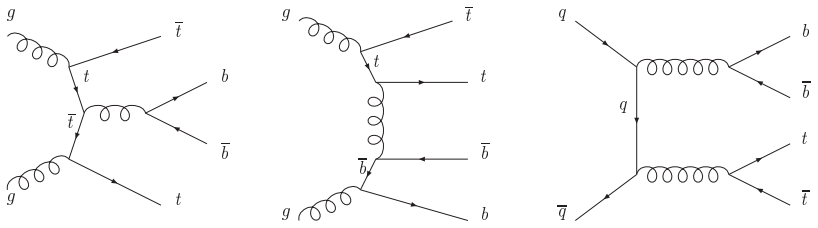

Figure 3.10: Example Feynman diagrams of the $t\bar{t}b\bar{b}$ QCD production.

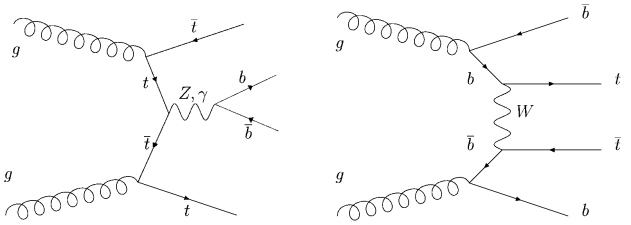

Figure 3.11: Example Feynman diagram of the electroweak $t\bar{t}b\bar{b}$ production.

Chapter 4

Event generation, Detector Simulation and Reconstruction

4.1 Introduction

The Monte Carlo (MC) simulation method is an essential part of high energy physics with various applications. This includes the optimisation of detector layout and performance but also the ability to implement theoretical or phenomenological models to then test them against real data. The simulation of physics events in ATLAS is carried out in two main steps:

1. **Event generation**: The physics process in the collisions of particles (protons for the LHC) is simulated based on theoretical and phenomenological models producing final-state particles as an output with the same average behaviour and the same fluctuations as expected from real data.

2. **Detector simulation**: The detector simulation is a detailed or parameterised simulation of the detector response to the final-state particles produced in the event generation and follows the physics laws of particles travelling through matter.

The next common step, which MC simulated events and events from real data after passing the online trigger selection have in common, is the offline **event reconstruction**. In the ATLAS experiment it is implemented in the software framework

ATHENA [41]. This chapter will give an overview of the event generators and detector simulations used in this thesis. A description of the reconstruction algorithms as implemented in the ATLAS software will be briefly introduced as the reconstruction of the final-states of the analyses relies on these algorithms.
In the following Sections 4.2 and 4.3, the MC generated information will be referred to as *truth* information.

This thesis makes use of high level reconstructed objects (electrons, muons, jets, etc.) that are standard in ATLAS. They are briefly described in Section 4.4.

4.2 Event Generation

The objective of an event generator is to describe the primary interactions of fundamental particles and their resulting production of multiple final-state particles is as much detaile as could be observed by a perfect detector. A typical hadronic event generator simulates (taken from the HERWIG manual [42]) the following subprocesses:

- **Initial-state composition and substructure**: Initially two beams of particles (protons for the LHC) are brought to collision. Each particle is characterised by a set of distributions which define its partonic sub-structure in terms of flavour composition and energy sharing.

- **Elementary hard subprocess**: A pair of incoming beam particles or their constituents interact to produce one or more primary outgoing fundamental objects. The hard, i.e. high momentum, transfer scale Q together with the colour flow of the the subprocess set the boundary conditions for the initial- and final-state parton showers.

- **Initial- and final-state showers**: A shower initiator parton from each beam starts off a sequence of branchings, which build up an initial-state shower. Just like the incoming partons, the outgoing partons may branch as well and produce final-state showers.

- **Heavy object decays**: Massive produced objects such as top quarks and Higgs bosons are unstable and decay further on timescales comparable or shorter to branching times in QCD parton showers. Depending on their nature and decay mode, they may also initiate parton showers before and/or after decaying.

- **Hadronisation and further decay**: The process of the formation of hadrons out of quarks and gluons is based on colour confinement, in which free quarks or gluons cannot exist individually.

The final-state particles represent therefore particles from the primary interaction, additional bremsstrahlung-type particles and a large number of particles from the hadronisation process.

4.2.1 Underlying Event

Additional parton interactions can take place among the components of the same particle which gave rise to the hard scattering process of interest. The outcome of this additional parton interaction is defined as the underlying event (UE). It usually results in very low p_T scattering processes which are difficult to model. There are different multiple parton interaction models. The UE in all samples used in this thesis has either been modelled by the JIMMY Monte Carlo program [43] or the multiple interactions in Pythia [44, 45].

4.2.2 Pile-up

Another source of additional low p_T interactions are pile-up events. These are events which take place among other proton-proton pairs in the same bunches as the hard scattering event. They are completely independent from the hard scattering process and therefore easier to describe than the underlying event. Pile-up interactions have not been included in the generation process of the simulated data used in this thesis because only the hard scatter was of interest in order to obtain the best estimate of possible achieved sensitivity.

4.3 Detector Simulation

The detector simulation is the next step that follows the event generation and describes the interaction of the generated final-state particles with the sensitive and non-sensitive detector material. Decays of non-stable final-state particles are also taken into account. To study the detector response for a wide range of physics processes and scenarios, a detailed simulation has been implemented to produce an output in a format that is identical to that of the true detector.

There are two different ways of simulating a particle interaction with the ATLAS detector, the *full* and *fast* simulation.

The full simulation uses a virtual high precision geometry model of the entire detector, the GEANT4 detector simulation [46] as well as physics laws describing the passage of particles through matter. The event reconstruction is done after digitisation of the hits in the full detector simulation. Track finding algorithms and pattern recognition (e.g. cluster finding algorithms in the calorimeters) work on digit banks to reconstruct the 4-vector momentum and the vertex coordinates, and to determine the particle type.

The principle of the fast simulation (ATLFAST-II [47]) is to replace the calorimeter portion of the full simulation with a faster method which involves adding average energy deposits per particle instead of running GEANT 4.

4.4 Reconstruction

The offline event reconstruction software which is implemented in the ATLAS software framework ATHENA, processes the physics event in many different stages. The outcome can be interpreted generally as final state objects with related four momenta in the form of charged tracks, electrons, photons, jets and muons. This section will only contain a brief description of the principle of the reconstruction algorithms, a more detailed description of reconstruction and performance can be found in [5].

4.4.1 Reconstruction of Charged Particle Tracks

The track reconstruction software [48] includes features covering the requirements of both the inner detector and muon spectrometer reconstruction. In the inner detector the track reconstruction is logically divided into three stages:

- A pre-processing stage, in which the raw data from the pixel and SCT detectors are converted into clusters and the TRT raw timing information is translated into calibrated drift circles. The SCT clusters are transformed into space-points by using a combination of the cluster information from opposite sides of a SCT module.

- A track-finding stage, in which different tracking strategies, optimised for different applications, are implemented.

- A post-processing stage, in which a dedicated vertex finder is used to reconstruct primary vertices. This is followed by algorithms dedicated to the reconstruction of photon conversions and secondary vertices.

The pattern recognition and track finding task is more difficult in a dense jet environment, in particular because hits can be shared between different tracks. This decreases the track reconstruction efficiency and increases the fake rate for tracks reconstructed inside jets. The details on the performance of track reconstruction for isolated charged particles as well as charged particles in jets can be found in [5].

4.4.2 Electron Identification

The default electron identification algorithm starts with a cluster in the electromagnetic (EM) calorimeter, with a transverse energy above 3 GeV and a matching inner detector track. The following criteria have to be satisfied:

- the EM cluster and extrapolated track have to be in the window of $\Delta\eta \times \Delta\phi = 0.05 \times 0.10$;

- the ratio E/p of the cluster energy and track momentum is required to be lower than 10 to ensure that the electron candidates are relatively isolated.

The standard identification algorithm for high-p_T electrons is then based on a combination of cuts, with three reference sets, *loose*, *medium* and *tight*, providing different electron efficiency versus jet rejection power.

Loose Electron Identification

The loose identification criteria are based on limited information from the calorimeters and provide excellent identification efficiency, but low background rejection. Cuts are applied on the hadronic leakage, the ration of E_T of the first sampling of the hadronic calorimeter to EM cluster E_T and on shower shape variables, derived from only the middle layer of the EM calorimeter. These are the lateral width of the shower and also the ratios in η (ϕ) of cell energies in 3×7 (3×3) versus 7×7 (3×7) cells [5].

Medium Electron Identification

The medium selection criteria increase the jet rejection by a factor of $3 - 4$ with respect to the loose identification, reducing the electron selection efficiency by $\sim$10%. This is achieved by adding cuts on shower shapes in the first layer of the EM calorimeter and on the tracking variables. Cuts on the strips in the first layer of the EM calorimter are effective in the rejection of $\pi^0 \rightarrow \gamma\gamma$ decays due to their characteristic energy-deposit pattern of two maxima close together. To reject these decays, a second maximum in energy is looked for in the cells of the first EM layer in a window of $\Delta\eta \times \Delta\phi = 0.125 \times 0.2$ around the cell with the highest E_T. Quality cuts are then applied on various variables (see Ref. [5]). In addition to that, cuts are applied to the track matched to the EM calorimeter cluster, including the number of hits in the pixels, the number of silicon hits (pixel + SCT) and the transverse impact parameter.

Tight Electron Identification

In addition to the cuts used in the medium set, cuts are applied on the number of vertexing-layer hits (to reject electrons from conversions), on the number of hits in the TRT, on the ratio of high-threshold hits to the number of hits in the TRT (to

reject the dominant background from charged hadrons), on the difference between the cluster and the extrapolated track positions in η and ϕ, and on the ratio of cluster energy to track momentum. Different final selections are available in this category: the tight (isol) selection, where an additional energy isolation cut is applied to the cluster within a cone of $\Delta R < 0.2$ around the electron candidate and the tight (TRT) selection, which applies tighter cuts on the TRT information to further remove the background from charged hadrons.

Performance

Table 4.1 shows the expected performance of the mentioned identification criteria. The first two criteria (loose and medium) will be used in the Higgs search analyses presented in this thesis. In the analysis further isolation requirements are applied to reject background from QCD multi-jet events with leptons from heavy flavour decays.

4.4.3 Jet Reconstruction

High quality and highly efficient jet reconstruction is an important tool for almost all physics analyses to be performed with the ATLAS experiment. The principal detector for jet reconstruction is the ATLAS calorimeter system which has been described in Section 2.2.2.

Calorimeter Jets

The ATLAS calorimeter system has about 200 000 individual cells of various sizes with different readout technologies and electrode geometries. For jet finding it is necessary to combine these cell signals into larger signal objects with physically meaningful four-momenta. There are two concepts available, one which is provided by a set of four-momenta representing the energy deposited in calorimeter towers of 0.1×0.1 in $\Delta\phi \times \Delta\eta$, the so-called calorimeter *signal towers*. The other concept is based on *topological cell clusters* (also called topoclusters), which attempts to build up more complex three-dimensional clusters of energy. In this thesis, the input to jet finding are topoclusters; a description of the signal towers can be found here [5].

Cuts	$E_T > 17$ GeV		
	Efficiency (%)		Jet rejection
	$Z \to ee$	$b, c \to e$	
Loose	87.9 ± 0.1	50.8± 1	567 ± 1
Medium	77.3 ± 0.1	30.7 ± 1	2184 ± 1
Tight (TRT)	61.7 ± 0.1	22.5 ± 0.4	(8.9 ± 0.3)·10^4
Tight (isol)	64.2 ± 0.1	17.3 ± 0.4	(9.8 ± 0.4)·10^4

Table 4.1: Expected efficiencies for isolated and non-isolated electrons and corresponding jet background rejections for the loose, medium and tight electron identification. The results shown are for simulated inclusive jet samples corresponding to E_T-thresholds of the electron candidates of 17 GeV. Taken from Ref. [5].

The latter approach has been adopted as the new standard for jet reconstruction and will therefore be described briefly here.

The clustering starts with seed cells with a signal-to-noise ratio $\mathrm{E_{cell}}/\sigma_{\mathrm{noise,cell}} > 4$. All directly neighbouring cells of these seed cells, in all three dimensions, are collected into the cluster. Neighbours of neighbours are considered for those added cells which have a signal-to-noise-ratio above 2. Finally, a ring of guard cells with signal significances above 0 is added to the cluster. After the initial clusters are formed, they are analysed for local signal maxima and split between those maxima if any are found.

Jet Finding Algorithms

The topoclusters are then used as input to the jet finding algorithms. Two main types of algorithms are implemented in ATLAS, seeded fixed cone and sequential recombination algorithms. The theoretical motivations and limitations of the various jet finding algorithms can be found in Ref. [49]. The analyses presented in this thesis make use of the sequential recombination algorithms Anti-$\mathrm{k_T}$ [50, 51] and the Cambridge/Aachen (C/A) algorithm [52, 53], therefore a brief description of both will be given here.

The most common sequential recombination algorithm is the inclusive $\mathrm{k_T}$ algo-

rithm. All pairs of input objects are analysed with respect to their distance measure, defined as:

$$d_{ij} = min(p_{T,i}^2, p_{T,j}^2)\frac{\Delta R_{ij}^2}{R^2}, \quad \Delta R_{ij}^2 = \sqrt{\Delta\phi_{ij}^2 + \Delta y_{ij}^2}, \tag{4.1}$$

where R is a cone-radius like parameter which determines the size of the jets and y the rapidity. In addition, also the distances of the objects i with respect to the beam are considered, since divergences in QCD branching also show up between initial state and final state partons and they are defined as $d_{iB} = p_{T,i}^2$. The minimum d_{min} of all d_{ij} and d_{iB} is determined. If d_{min} is among one of the d_{ij}, then the corresponding objects i and j are merged into a single new object using four-momenta recombination, while if d_{min} is one of the d_{iB}, the object i is considered to be a jet by itself and removed from the list. This procedure is repeated iteratively, updating all distances at each iteration step. The four-momenta recombination scheme is usually chosen to be the simple sum of the two four momenta of the objects i and j. The advantage of the k_T algorithm is that it is by construction collinear and infrared safe, however, it is also more sensitive to picking up soft contributions from pile-up and the underlying event.

The k_T algorithm can be generalised by introducing the following particle-particle and particle-beam measures:

$$d_{ij} = min(p_{T,i}^{2r}, p_{T,j}^{2r})\frac{\Delta R_{ij}^2}{R^2}, \quad \Delta R_{ij}^2 = \sqrt{\Delta\phi_{ij}^2 + \Delta y_{ij}^2}, \tag{4.2}$$

$$d_i = p_{T,i}^{2r}, \tag{4.3}$$

where r is a parameter which is 1 for the k_T algorithm.

Two different algorithms can be obtained: the C/A algorithm by choosing a value of $r = 0$ and the Anti-k_T algorithm by choosing a value of $r = -1$. The C/A algorithm recombines objects close in ΔR iteratively and reflects the angular ordering of QCD radiation, hence it is ideally suited to reconstruct and decompose the various decay components of heavy objects like the Higgs boson [4] or top quarks [54]. It will therefore be used to study boosted Higgs boson decays into a pair of b-quarks in the analysis of jet substructure presented in this thesis (see Chapter 7).

Contrary to the k_T algorithm, the Anti-k_T algorithm first clusters hard objects together, resulting in more regular jets with respect to the k_T and C/A algorithms:

it was recently made the new standard algorithm for jet finding in ATLAS [55], replacing a fixed-cone algorithm which is collinear unsafe. The Anti-k_T algorithm will be used in the cut-based version of the Higgs search analysis in this thesis.

4.4.4 Identification of b-quark Jets

The identification of jets originating from bottom-quarks (*b-tagging*) is important for the high-p_T physics program of ATLAS, for example for top physics and Higgs boson searches and studies. The identification of b-jets takes advantage of several of their properties which makes it possible to distinguish them from jets containing only lighter quarks:

- The fragmentation is hard and the b-hadron retains about 70% of the original b quark momentum [5].
- The mass of b-hadrons is relatively high (> 5 GeV), therefore their decay products have a large transverse momentum with respect to the jet axis and the opening angle of the decay products is large enough to allow separation.
- The lifetime of b-hadrons is relatively long, of the order of 1.5 ps ($c\tau \approx 450\ \mu$m). The resulting displaced vertices can be identified by measuring the impact parameters of the track from the b-hadron decay products. Figure 4.1 shows a schematic drawing of the impact parameter. The transverse impact parameter d_0 is the distance of closest approach of a track to the primary vertex point in the $r - \phi$ direction. The longitudinal impact parameter z_0 is the z coordinate of the track at the point of closest approach in $r - \phi$.
- The semileptonic decays of b-hadron can be used by tagging the lepton in the jet which will, due to the hard fragmentation and the high mass, have a relatively large transverse momentum.

The following will briefly describe the relevant b-tagging algorithms used for the Higgs search analyses in this thesis.

On the basis that the decay point of the b-hadron must lie along its flight path, the impact parameter is signed to further discriminate the tracks originating from a

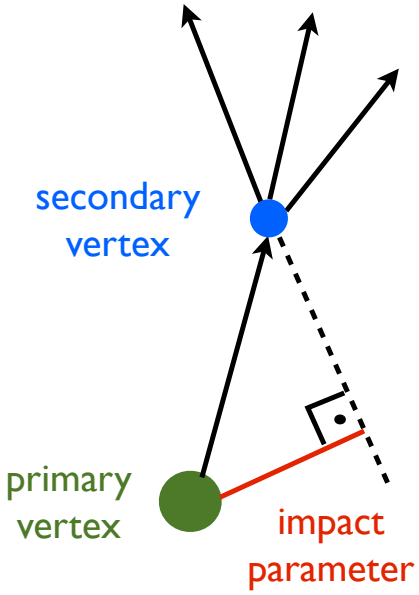

Figure 4.1: Schematic drawing of the impact parameter, the closest approach of a track to the primary vertex.

b-hadron decay from tracks from the interaction point (primary vertex). The significance of the impact parameters of all tracks in a jet is then computed. Three tagging algorithms are defined in this way: IP1D relies on the longitudinal impact parameter, IP2D on the transverse impact parameter whereas IP3D uses two-dimensional histograms of the longitudinal versus transverse impact parameters.

To further increase the discrimination between b-jets and light jets, the secondary vertex (SV) formed by the decay products of the b-hadron is considered.

In the following, two b-tagging algorithms, the two dimensional SV and the JetFitter algorithm, are considered. Both are used in combination with the impact parameter based algorithm IP3D.

According to the conventional definition in ATLAS, a jet is labelled a jet of a certain quark flavour (b, c or light) by exploiting the MC truth information. This labelling procedure is not unambiguous. A jet is labelled as a b-jet if a b quark with $p_T > 5$ GeV is found in a cone of size $\Delta R = 0.3$ around the jet direction. The various labelling hypotheses are tried in this order: b quark, c quark and τ lepton. When

no heavy flavour quark nor τ lepton satisfies these requirements, the jet is labelled as a light-jet. No attempt is made to distinguish between u, d, s quarks and gluon since such a label is even more ambiguous.

A difficulty arises as soon as the jet multiplicity is high and various jet flavours are present in a single event: a jet with ΔR (jet-b) = 0.31 is labelled as a light jet, although tracks from b-hadron decay with high lifetime content are likely to be associated to it. This leads to a decrease of the estimated performance, not related to the b-tagging algorithm itself but to the labelling procedure which strongly depends on the activity of the event. In order to obtain a more reliable estimation of b-tagging performance, a purification procedure has been devised: light jets for which a b quark, a c quark or a τ lepton is found within a cone of size $\Delta R = 0.8$ around the jet direction are not used to compute the rejection [5]. Figure 4.2 shows the rejection of light and c-jets with and without purification versus b-jet efficiency for $t\bar{t}$ events.

Combined b-tagging Algorithm (COMB)

The main idea of the inclusive secondary vertex reconstruction used in the COMB tagger is to maximise the b/c-hadron vertex detection efficiency, keeping the probability low to find a light jet.

The secondary vertex (SV) is found by evaluating all two-track vertices formed by tracks far enough from the primary vertex. Vertices compatible with vertex from K_s^0 and λ^0 decays, $\gamma \rightarrow e^+e^-$ conversions or hadronic interactions in the material are rejected. All tracks from the remaining two-track vertices are then combined into a single inclusive vertex using an iterative procedure removing the worst track until the χ^2 of the vertex fit is good. Once the secondary vertex is found, three of its properties are exploited: the invariant mass of all tracks associated to the vertex, the ratio of the sum of the energies of the secondary vertex tracks to the sum of the energies of all tracks in the jet and the number of two-track vertices. Two SV tagging algorithms make different use of these properties: SV1 relies on a 2D-distribution of the two first variables and a 1D-distribution of the number of two-track vertices, while SV2 is based on a 3D-histogram of the three properties.

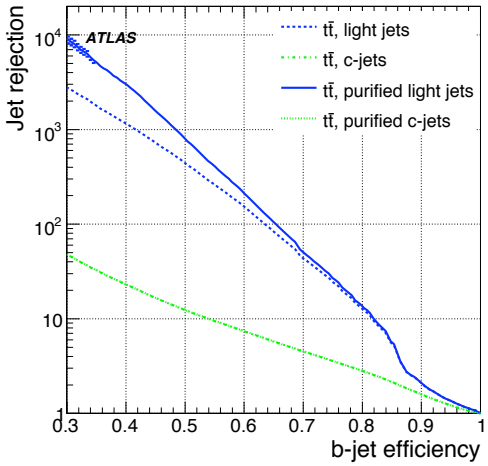

Figure 4.2: Rejection of light jets and c-jets with and without purification versus b-jet efficiency for $t\bar{t}$ events, using the tagging algorithm based on 3D impact parameter and secondary vertex. The distribution for c-jets and purified c-jets (both green lines) are on top of each other.

The default b-tagging algorithm COMB in ATLAS is a likelihood combination of the impact parameter IP3D and the secondary vertex SV1 algorithms, where the weight of a jet is found as the sum of the weights for each of the algorithms. A description of the method can be found in Ref. [56].

For the combination of the SV1 and IP3D, a likelihood ratio method is used: the measured value S_i of a discriminating variable is compared to pre-defined smoothed and normalised distributions for b- and light jet hypotheses, $b(S_i)$ and $u(S_i)$. The ratio of these probabilities defines the track or vertex weight, which can be combined into a jet weight W_{jet}:

$$W_{jet} = \sum_{i=1}^{N_T} lnW_i = \sum_{i=1}^{N_T} ln\frac{b(S_i)}{u(S_i)} \tag{4.4}$$

JetFitter Vertex Reconstruction Algorithm (JetFitterCOMBNN)

The JetFitter algorithms (JetFitterCOMBNN) [57] uses a new inclusive secondary vertex reconstruction algorithm combined with the pure impact parameter based algorithm IP3D. The combination of the JetFitter and IP3D algorithm is realised by using a neural network. This secondary vertex reconstruction algorithm [57] exploits

the topological structure of weak b- and c-hadron decays inside a jet. The default secondary vertex based b-tagging algorithm in ATLAS selects displaced tracks and fits a single vertex [58]. But the underlying hypothesis of having a single geometrical vertex is not correct. If the distance between the decay vertices of the b- and c-hadron is significant compared to the vertex resolution in the flight direction, the tracks from one of the two vertices can be lost in the fit.

The JetFitter algorithm assumes that the b- and c-hadron decay vertices lie on the same line defined through the b-hadron flight path. All charged particle tracks from either the b- or c-hadron decay thus intersect this b-hadron flight axis. From the physics point of view this hypothesis is justified through the kinematics of the particles involved as defined through the hard b-quark fragmentation function and the masses of b- and c-hadrons. The lateral displacement of the c-hadron decay vertex from the b-flight path is small enough to not get resolved due to the tracking detector resolution and therefore not to violate the basic assumption. More details about the implementation of this algorithm can be found in Ref. [57].

4.4.5 Muon Identification

There are two main strategies to identify and reconstruct muons and only the baseline algorithms adopted as standard in the reconstruction will be briefly described here. The direct approach is to reconstruct muons *standalone* by finding tracks in the muon spectrometer and to extrapolate them then to the beam line. The other approach which yields *combined* muons, is to match standalone muons to inner detector tracks and to then combine the two measurements. Some efficiency is recovered and *tagged* muons are found by extrapolating all tracks reconstructed in the inner detector and looking for unused hits in the muon system along their extrapolated path.

The reconstruction of the standalone muons starts from building track segments in each of the three muon stations. These segments are then linked together and the track is extrapolated to the beam line. The enlargement of the track parameter errors due to multiple scattering in the detector material has to be taken into account. Standalone muons can be reconstructed up to $|\eta| = 2.7$, extending the inner detector

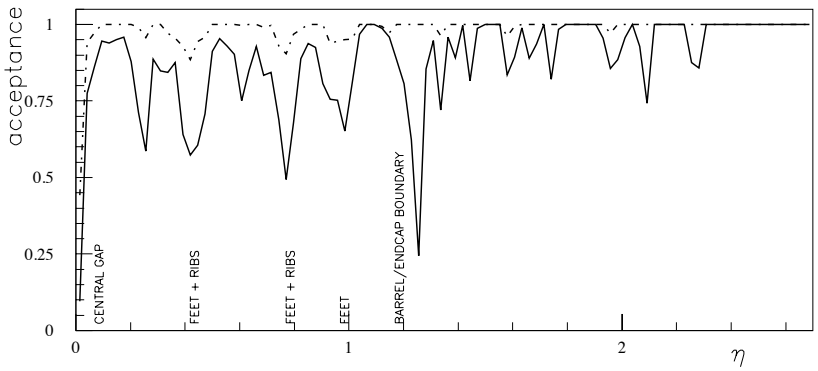

Figure 4.3: Acceptance for the requirements of one superpoint (dash-dotted line) and three superpoints (solid line) in the three stations of the precision chamber system as a function of pseudorapidity and averaged over azimuthal angle. A superpoint is a coincidence of at least six hits in six different sensitive planes in one chamber. Taken from [14].

coverage of up to $|\eta| = 2.5$, but with the most dominant acceptance holes around the central gap at $\eta = 0$ and at $|\eta| = 1.2$ where the barrel/end-cap boundary is. Figure 4.3 shows the limitations of the barrel system.

The combination of standalone muons and inner detector tracks relies on a χ^2_{match} which is defined by the probability that the track parameters of the inner detector and muon system standalone tracks are compatible with each other within their experimental errors. A simple statistical combination of the two tracks is then performed. Combined muons reduce the rate of so-called fake muons by around 40%. Fake muons originate mainly from muons produced by π and K decays in the calorimeter.

4.4.6 Missing Transverse Energy

Missing energy at a hadron collider can only be measured in the transverse plane (E_T^{miss}), since an unknown fraction of the longitudinal momenta of the incoming protons is carried away by the proton remnants leaving the detector outside its acceptance region after the hard scattering has occurred. E_T^{miss} is primarily reconstructed from energy deposits in the calorimeter and reconstructed muon tracks.

Apart from the hard scattering process of interest, many other sources, such as the underlying event, multiple interactions, pile-up and coherent electronics noise, lead to energy deposits and/or muon tracks. Classifying the energy deposits into various types (e.g. electrons or jets) and calibrating them accordingly is the essential key for an optimal E_T^{miss} measurement. In addition, the loss of energy in dead regions and readout channels make the E_T^{miss} measurement a real challenge. Simulation studies on typical physics events show that the E_T^{miss} can be reconstructed with a response which is linear to within 5%.

Chapter 5

Cut-based Analysis of the $t\bar{t}H^0(H^0 \to b\bar{b})$ Channel

5.1 Introduction

The search for the Higgs boson will be one of the major tasks of the experiments at the LHC. In the low Higgs boson mass range (up to about $m_{H^0} = 135$ GeV) the decay mode with the highest branching fraction is $H^0 \to b\bar{b}$. The analysis of reconstructing the associated production of a Higgs boson with a top quark pair in the semileptonic final state is presented in this chapter.

A recent study of the $t\bar{t}H^0(H^0 \to b\bar{b})$ channel presented in [5] (which will be referred to as the CSC analysis) uses cut- and likelihood-based approaches to separate signal and backgrounds. The study was carried out at a centre-of-mass energy of $\sqrt{s} = 14$ TeV. The cut-based approach lead to an accepted cross-section of about 1 fb at a signal-to-background ratio of roughly 10% and a statistical significance of $S/\sqrt{B} = 1.82$ for an integrated luminosity of 30 fb^{-1}.

The LHC run plan had foreseen a centre-of-mass energy of $\sqrt{s} = 10$ TeV for the first physics run. The cut-based analysis which is presented here follows previous work [5] and aims at exploiting the sensitivity of the $t\bar{t}H^0(H^0 \to b\bar{b})$ channel at this centre-of-mass energy. It has been performed with Monte Carlo samples produced at a centre-of-mass energy of $\sqrt{s} = 10$ TeV and an assumed integrated luminosity of 100 fb^{-1}, using a realistic detector simulation. The signal samples have been

generated using the full detector simulation, whereas the background samples have been generated using the fast simulation (see Section 4.3 for details).

This chapter is organised as follows. First, the simulated samples which have been used are described. Then the analysis itself is described, starting with the lepton and jet preselection, the trigger requirements and the reconstruction of the $t\bar{t}$ system before finally reconstruction the Higgs boson. The reconstruction of the $t\bar{t}H^0$ final state is followed by the significance estimation together with a comparison of the results to the previously performed CSC analysis performed at $\sqrt{s} = 14\,\text{TeV}$. Finally the systematic uncertainties are discussed.

5.2 Simulated Samples

The signal and all background samples have been generated at leading order with a centre-of-mass energy of 10 TeV, a Higgs boson mass of $m_H = 120$ GeV and a top quark mass of $m_{top} = 172.5$ GeV [36]. As backgrounds, those described in Chapter 3.4.4 have been considered. Section 5.2.2 will give a brief explanation of the choice of centre-of-mass energy.

5.2.1 Signal and Background Samples

The signal sample has been generated using Pythia 6.401 [44] separately, depending on the charge sign of the lepton from the semileptonic top decay. A lepton filter is applied, requiring the lepton to have a transverse momentum of $p_T^l \geq 10$ GeV and to be within $|\eta| \leq 2.7$. The simulated samples for the signal processes of the semileptonic channel $t\bar{t}H^0(H^0 \rightarrow b\bar{b})$ are summarised in Table 5.1.

The irreducible $t\bar{t}b\bar{b}$ background via QCD or electroweak (EW) interactions have been generated in two separate samples. AcerMC [59] has been chosen as matrix element (ME) generator for the irreducible EW $t\bar{t}b\bar{b}$ background sample. Extra decays, parton showering, fragmentation and hadronisation have been modelled by Pythia as the supervising generator. The top quarks have been forced to decay semileptonically. The hard process of the likewise irreducible $t\bar{t}b\bar{b}$ QCD background has been generated by ALPGEN [60], interfaced to HERWIG 6.5 [61] as supervising generator and JIMMY [43] to model the underlying event. The generated processes

Dataset number	105870	105871
Process	Semileptonic $t\bar{t}H^0(H^0 \to b\bar{b})$ (positive lepton)	Semileptonic $t\bar{t}H^0(H^0 \to b\bar{b})$ (negative lepton)
Production mode	gg, $q\bar{q}$	
$t\bar{t}$ decays included	Semileptonic (e, μ)	
Q scale ($m_T^2 = m^2 + p_T^2$)	$\max(m_T^2(t), m_T^2(\bar{t}))$	
PDF set used	CTEQ6L1	
Supervising generator	Pythia 6.401	
Cross-section (fb)	21.64	21.52
Detector simulation	Full	
Filter type	LeptonFilter	
Filter efficiency	0.96	0.96
Decays	Semileptonic (e, μ)	
Final cross-section (fb)	20.77	20.72

Table 5.1: Summary of the simulated $t\bar{t}H^0$ signal sample produced in two separate sub-samples depending on the charge sign of the lepton from the W decay.

are $pp \to t\bar{t}b\bar{b}$ +X with all $t\bar{t}$ system decays possible. The ATLAS Monte Carlo event filter *TTbarPlusJetsFilter* has been applied at generator level to both samples. The filter ensures that only events with a minimum number of jets are selected to enrich the samples with high multiplicity jet events for the $t\bar{t}H^0$ analysis. It applies loose cuts on hadron-level jets, which are reconstructed using a seeded fixed-cone algorithm with a cone size of $\Delta R = 0.4$ (see Jet Reconstruction Performance Chapter in [5]):

- at least 6 jets with $p_T > 15$ GeV and $|\eta| < 5.2$ to ensure that the minimum number of final state jets is present in the event,
- at least 3 jets with $p_T > 15$ GeV and within the inner detector acceptance of $|\eta| < 2.7$, to be able to b-tag the jets.

Additionally, a cut on all other jets of $|\eta| < 6$ has been applied at matrix element

level. Since the $t\bar{t}b\bar{b}$ QCD samples contain all $t\bar{t}$ decays, a selection for semileptonic events with electrons and muons was applied and the cross-sections are summarised in Table 5.2.

Dataset	109627	109626
Process	$t\bar{t}b\bar{b}$(QCD)	$t\bar{t}b\bar{b}$(EW)
Production mode	gg, $q\bar{q}$	gg
$t\bar{t}$ decays included	All	All
ME generator	ALPGEN 2.13	AcerMC
ME cross-section (fb)	3703.5	195.4
Q scale ($m_T^2 = m^2 + p_T^2$)	232.5 GeV	$\hat{s}$
PDF set used	CTEQ6L1	CTEQ6L
Cuts	$\lvert\eta_{\text{light jet}}\rvert < 6$	-
ME cross-section at Q=232.5 GeV (fb)	3703.5	315.2
Supervising generator	HERWIG	Pythia
Enforced decays	-	Semileptonic e, μ
Cross-section before filter (fb)	3703.5	90.78[a]
Detector simulation	ATLFAST II	
Filter type	TTbarPlusJetsFilter	TTbarPlusJetsFilter
Filter efficiency	0.72	0.78
Semileptonic e,μ selection efficiency	0.2492	1.0
Final cross-section (fb)	661.53	70.99

Table 5.2: Summary of the simulated $t\bar{t}b\bar{b}$ background samples contributing as irreducible backgrounds.

[a]by-hand multiplication of ME cross-section with semileptonic (e, μ) BR based on current PDG values: 28.8%

The reducible $t\bar{t}X$ background has been generated in four sub-samples containing between zero and three additional light partons, where a light parton is defined here as g, u, d, s or c. These samples have been generated with ALPGEN 2.13 [60] as

Dataset	109620	109621	109622	109623
Process ($t\bar{t}$ + X partons)	$t\bar{t}+0$	$t\bar{t}+1$	$t\bar{t}+2$	$t\bar{t}+3$
Production mode	gg,$q\bar{q}$			
$t\bar{t}$ decays included	Semileptonic (e,μ,τ)			
ME generator	ALPGEN 2.13			
ME cross-section (fb)	95360	121220	91370	50480
Q scale ($m_T^2 = m^2 + p_T^2$)	$\sum m_T^2$ over all (final state partons)			
PDF set used	CTEQ6L1			
Cuts	$p_T^{\text{light jet}} > 20$ GeV, $\lvert\eta_{\text{light jet}}\rvert < 6$ ΔR(light jet, light jet) > 0.7			
ME cross-section at Q=232.5 GeV (fb)	105196	139197	108649	62880
MLM matching efficiency	0.39	0.29	0.22	0.16
Supervising generator	HERWIG			
Cross-section before filter (fb)	41363.1	39893.9	23479.0	10274.6
Detector simulation	ATLFAST II			
Filter type	TTbarPlusJetsFilter			
Filter efficiency	0.17	0.45	0.80	0.97
AOD cross-section (fb)	6920.05	17868.48	18665.81	9930.40
Semileptonic e,μ selection efficiency	0.5394	0.5910	0.6417	0.6607
Cross-section after filter (fb)	3732.67	10560.27	11977.85	6561.02
Cross-section after overlap removal (fb)	3588.44	10060.23	11261.51	6011.77

Table 5.3: Summary of the simulated $t\bar{t}X$ background samples, simulated in four sub-samples containing between zero and three additional light partons. The cross-sections after removing the overlap (see text and Chapter 6 for details) are also given.

ME generator, interfaced to HERWIG [42, 61] and Jimmy [43]. The events in the samples correspond to the processes $pp \to t\bar{t} \to q\bar{q}'bl\nu b$ with $l = e, \mu, \tau$. The four samples are made exclusive by MLM matching [62] between the additional light partons and jets found in the HERWIG event record after processing. The necessity for applying MLM matching is due to the separate generations and the difficulty to unambigously separate the components of the event which belong to the hard process from those developing during its evolution (described by parton shower). The MLM matching procedure is therefore applied to avoid double counting of events by matching partons from matrix element calculations to jets reconstructed after the pertubative shower. Events that are not fully matched are rejected.

Additional cuts on the light partons not coming from the $t\bar{t}$ system are applied at ME level:

- $p_T > 25$ GeV and $|\eta| < 6$
- $\Delta R > 0.7$ between jets.

These cuts are applied to ensure the possibility of reconstructing these light partons by requiring the partons to not be too close together or be too soft.

The reducible $t\bar{t}X$ and irreducible $t\bar{t}b\bar{b}$ background contributions have been generated separately from each other to be able to study their contributions and behaviour individually. However, this creates an overlap of events since the addition of b-quarks to $t\bar{t}$ events via parton showering in HERWIG produces events that are included in the matrix-element cross-section calculation for the $t\bar{t}b\bar{b}$ sample. Therefore it was necessary to develop a procedure to remove this overlap which is described in detail in Chapter 6. This overlap removal procedure is applied to the $t\bar{t}X$ background and the cross-sections of the simulated samples after the overlap removal are given in Table 5.3.

5.2.2 Centre-of-mass Energy Considerations

The LHC is designed to collide proton beams with a centre-of-mass energy of $\sqrt{s} = 14\,\text{TeV}$. However, for the first physics run in the beginning of the LHC operation a centre-of-mass energy of $\sqrt{s} = 7\,\text{TeV}$ has been chosen. At the time of

generating the MC samples for this thesis, the run plan had foreseen a longer run with $\sqrt{s} = 10\,\text{TeV}$, which is why the MC samples used in this thesis were generated at $\sqrt{s} = 10\,\text{TeV}$.

In order to compare results of this thesis with results previously obtained with simulated data at a centre-of-mass energy of $\sqrt{s} = 14\,\text{TeV}$, a simple preselection has been applied to $t\bar{t}H^0$ events, generated with Pythia 6.4 [44] and with $\sqrt{s} = 7$ TeV, 10 TeV and 14 TeV. The cuts are applied at parton level, with jets reconstructed with the cone jet algorithm using an R-parameter of 0.4. The cuts applied are similar to the preselection cuts applied in the following cut-based analysis to ensure the presence of the basic physics objects used. An event passes the preselection if exactly one lepton with $p_T > 15$ GeV and $|\eta| < 2.5$ and at least six jets with a minimum transverse momentum of $p_T > 20$ GeV in $|\eta| < 5$ are found. At least four of which have to be b-tagged (assumed b-tagging efficiency 70%, light-jet efficiency 1%) and lie within $|\eta| < 2.5$.

The cross-sections before and after preselection as well as the efficiencies for the lepton and jet preselection are summarised in Table 5.4. The resulting cross-section scaling factor for signal S and backgrounds B between the 10 TeV and 14 TeV sample is 2.05 and 2.71 between the 7 TeV and 10 TeV sample. Since the significance is $S/\sqrt{B}$ and both S and B scale by 2.05, the obtained significances for this analysis have to be scaled by a factor of $\sqrt{2.05} = 1.43$ to compare them to the significances obtained in the 14 TeV analysis carried out in the CSC note [5].

The method of obtaining a scaling factor to adapt for the different centre-of mass energies is an approximate method, that assumes no change in the analysis efficiencies after the preselection and also that both signal and background scale by the same amount. The first assumption seems reasonable since the preselection efficiencies themselves are quite close together (as shown in Table 5.5).

5.3 Analysis Overview

The analysis of the $t\bar{t}H^0(H^0 \to b\bar{b})$ channel aims at reconstructing the complete final state of the event to minimise the combinatorial background when assigning two of the four b-jets to the Higgs boson decay. The cut-based method consists of

$\sqrt{s}$	cross-section	preselection efficiency		cross-section
	before preselection	lepton	jet	after preselection
7 TeV	8.12 fb	65.62%	10.85%	0.58 fb
10 TeV	21.98 fb	63.91%	11.16%	1.57 fb
14 TeV	51.96 fb	62.92%	9.85%	3.22 fb

Table 5.4: Cross-sections before and after the preselection carried out at parton level for simulated $t\bar{t}H^0$ events at centre-of-mass energies of $\sqrt{s}$ = 7 TeV, 10 TeV, 14 TeV and the selection efficiencies of the lepton and jet preselection. The resulting cross-section scaling factor between the 10 TeV and 14 TeV sample is 2.05 and 2.71 between the 7 TeV and 10 TeV sample.

three steps:

- A preselection to ensure the fundamental physics objects like leptons and jets necessary to reconstruct the $t\bar{t}H^0$ system are present and reconstructed in the event.
- The reconstruction of the $t\bar{t}$ system.
- The reconstruction of the Higgs decay.

The identification and association of decay products is directly related to the quality of the reconstructed Higgs boson signal. It mainly suffers from the mis-association of the four b-tagged jets to the original partons.

In the following analysis the concept of *correct jets* is defined by finding the closest reconstructed jet to each parton, after the final state radiation. The jets are matched to partons in ΔR and must be closer than 0.2. A W or Higgs boson is correctly matched if both of the jets used to reconstruct the candidate are associated to the partons from its decay, while for a top quark the matching refers to the b quark jet only.

5.4 Preselection

To select only events compatible with the signal topology of four b-jets, two light jets and one lepton, a preselection is applied and requires:

- exactly 1 isolated lepton, where a lepton can be either an electron or a muon ($\ell = e, \mu$); taus are not considered in this analysis
- at least 6 jets of which at least 4 must be tagged as b-jets.

5.4.1 Lepton Preselection

Leptons (electrons and muons) have to pass the kinematic and geometrical cuts on the transverse momentum $p_T > 15$ GeV and pseudorapidity $|\eta| < 2.5$ as well as some lepton-type specific cuts to be accepted as a candidate electron or muon coming from the semileptonic decay of the $t\bar{t}$ system. These cuts were chosen following the recommendations of the dedicated electron and muon identification groups in ATLAS.

Electrons are required to pass the ATLAS loose electron-ID selection (isEM = ElectronLoose) (see Section 4.4.2 for more detail). An isolation cut is also applied to the candidate electrons in the form an upper limit of 0.15 on the ratio of the transverse momentum of additional tracks inside a cone of size $\Delta R = 0.2$ around the electron track to the electron p_T:

$$\frac{p_{T,cone}(\Delta R = 0.2)}{p_T(e)} < 0.15 \tag{5.1}$$

Figure 5.1 shows the p_T , η, and track isolation for all reconstructed electrons and those which could be matched to an electron from the semileptonic top decay.

For a muon to be accepted as the candidate lepton from the semileptonic top decay, it must be reconstructed using a combination of the inner detector and muon spectrometer, a so-called combined muon (see Section 4.4.5). Additionally, a loose isolation criterion on the ratio between the transverse energy deposited inside a cone of size $\Delta R = 0.2$ around the muon track and the muon p_T is required to be satisfied:

$$\frac{E_{T,cone}(\Delta R = 0.2)}{p_T(\mu)} < 0.3 \tag{5.2}$$

To remove muons generated by the decay of long-lived mesons, a cut on the transverse impact parameter of 0.05 is applied. Figure 5.2 shows the distributions of the muons properties which are used to select the candidate muon.

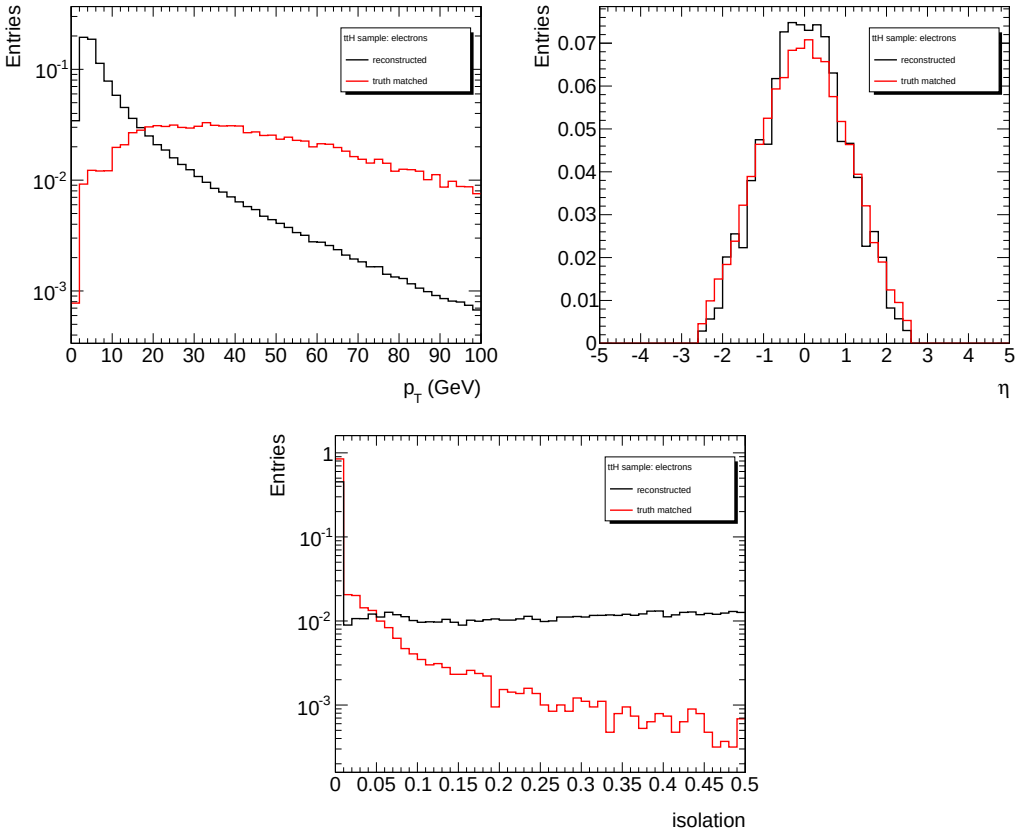

Figure 5.1: p_T, η and track isolation distribution for all reconstructed electrons and those which could be matched to an electron from the semileptonic top decay in the signal sample. Distributions are normalised to unit area.

If more than one lepton passes the selection cuts, the event will be rejected. Vetoing events with two or more isolated leptons is intended to remove additional sources of background, like *e.g.* the fully leptonic $t\bar{t}$ process. Figure 5.3 shows the number of reconstructed leptons for cases when one or more than one lepton are found in the signal sample. The lepton preselection efficiency in the signal is 61.3%, efficiencies for all samples can be found in Table 5.5.

5.4.2 Jet Preselection

The Anti-k_T jet algorithm is used to reconstruct jets using an R parameter of $R = 0.4$, with topoclusters as input. This jet algorithm was found to exhibit the best jet reconstruction efficiency for jets at low p_T and, specifically for the Higgs recon-

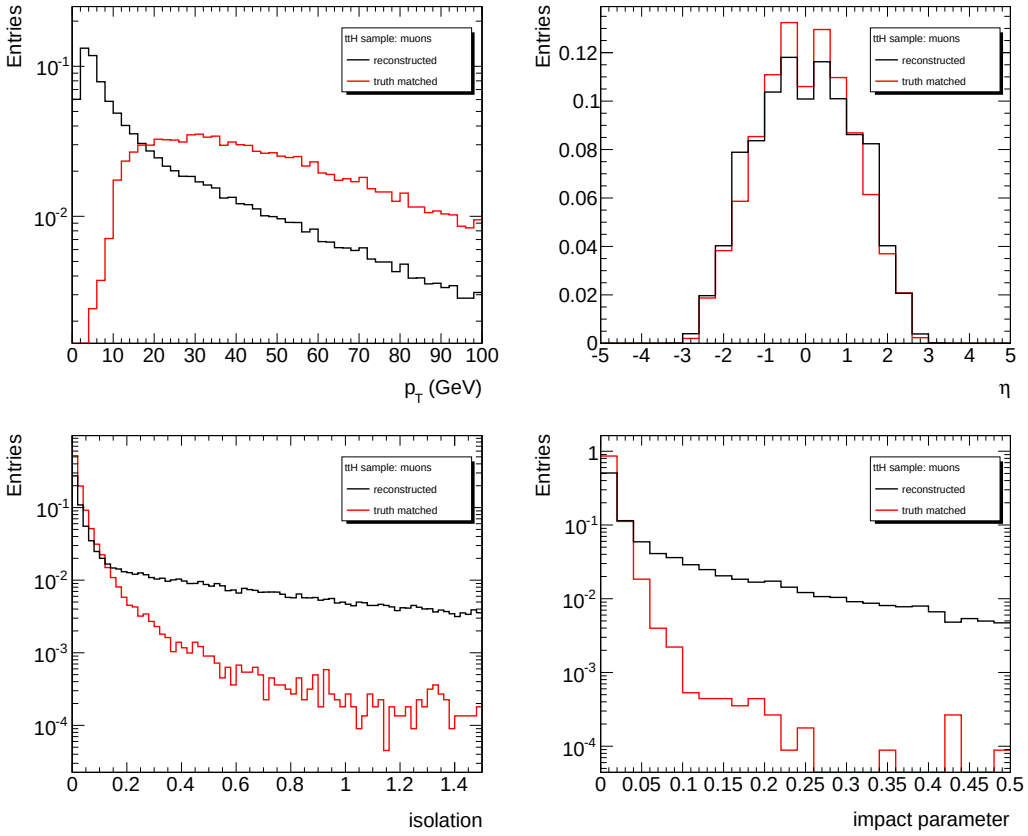

Figure 5.2: p_T, η, energy isolation and transverse impact parameter distribution for all reconstructed muons and those which could be matched to a muon from the semileptonic top decay in the signal sample. Distributions are normalised to unit area.

struction in the $t\bar{t}H^0$ channel, to give the best mass reconstruction and the highest signal efficiency [55]. Jets are required to have a transverse momentum $p_T > 20$ GeV and be within the pseudorapidity of $|\eta| < 5$. At least six jets are required to reconstruct the signal state, four of which have to be b-tagged and therefore lie within the inner detector acceptance of $|\eta| < 2.5$.

b-tagging

Two b-tagging algorithms have been considered in this analysis: the "JetFitter" based algorithm (*JetFitterCOMBNN*) and the combined b-tagging algorithm (*COMB*) (see Section 4.4.4). Both b-taggers are based on a weight which is trained to get the

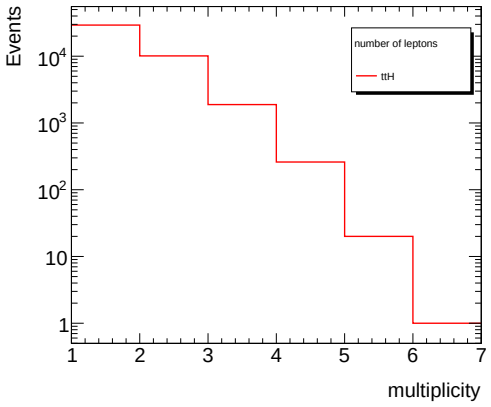

Figure 5.3: Lepton (e, μ) multiplicities for events in which one or more lepton are found in the signal sample.

best possible separation of of b-jets from light-quark jets.

In order to determine the optimal b-tagging strategy for the present analysis, the significance $\frac{S}{\sqrt{B}}$ has been analysed as a function of the b-tagging weight of the JetFitterCOMBNN and COMB tagger. This is shown in Figure 5.4 (left), the significances are obtained by applying the $t\bar{t}$ and Higgs reconstruction as described in the CSC analysis. Based on this, the b-tagging algorithm chosen for this analysis is the JetFitterCOMBNN and jets are tagged as b-jets if the cut on the weight of the jet $W_{jet} > 1$ is satisfied.

Figure 5.5 shows the distribution of b-tagging weights for the JetFitterCOMBNN for jets passing the kinematic and acceptance cuts and matched to b, c or light (u, d, s) quarks.

The efficiency ϵ_b to tag a jet of flavour q as a b-jet is defined as:

$$\epsilon_b = \frac{\text{Number of jets tagged as } b\text{-jets}}{\text{Number of } b\text{-jets}} \tag{5.3}$$

Usually ϵ_b is called tagging efficiency whereas ϵ_{udsc} is called mistagging rate. The so-called b-tagging rejection is the inverse of the mistagging rate: $r_{udsc} = 1/\epsilon_{udsc}$. A light ($c$-) jet rejection of 100 translates as one light (c-) jet in a hundred being mistagged as a b-jet.

The b-tag efficiency of the two considered algorithms versus the b-tagging weight is shown in Figure 5.4 (right) and Figure 5.6 shows the light (left) and c (right) jet

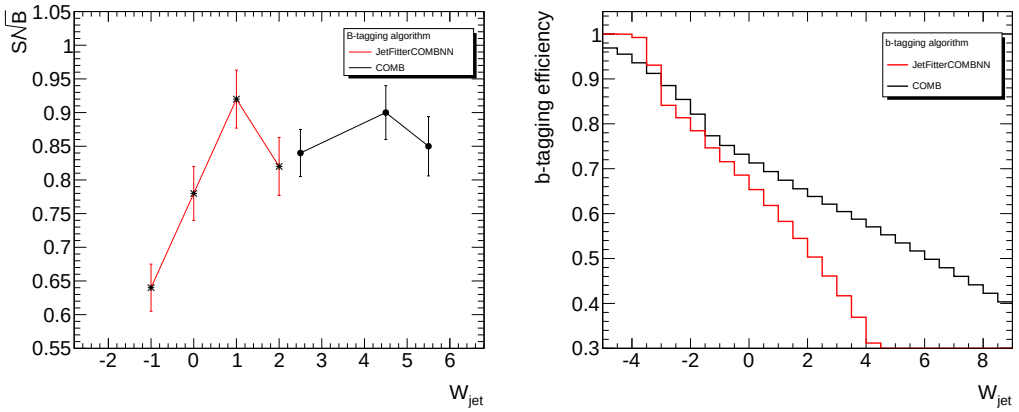

Figure 5.4: Left: Statistical significance as a function of the b-tagging weight corresponding to a certain cut on the b-tagging weight for the two considered b-tagging algorithms COMB and JetFitterCOMBNN, for the $t\bar{t}H^0$ samples. Right: b-tagging efficiency versus b-tagging weight for the b-tagging algorithms JetFitterCOMBNN and COMB.

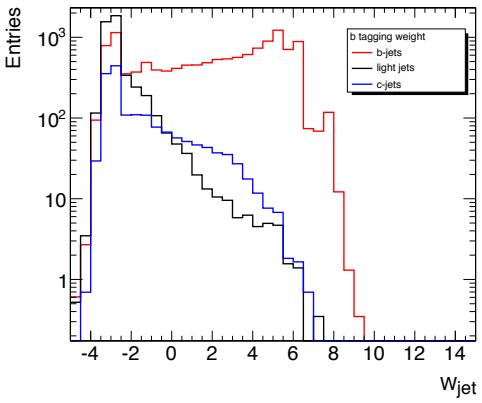

Figure 5.5: Distribution of b-tagging weight for $b-, c-$ and light jets in $t\bar{t}H^0$ events, using the JetFitterCOMBNN tagger.

rejection factor versus the b-tagging efficiency. For $W_{jet} > 1$, using the JetFitterCOMBNN algorithms, the b-tagging efficiency is 58.3%, with a light jet rejection factor of 73.6 and a c-jet rejection factor of 8.6. The highest significance for the COMB tagger is at $W_{jet} = 4.5$ which implies a b-tagging efficiency of about 55.3%, a light jet rejection factor of 83.2 and a c-jet rejection factor of 9.7.

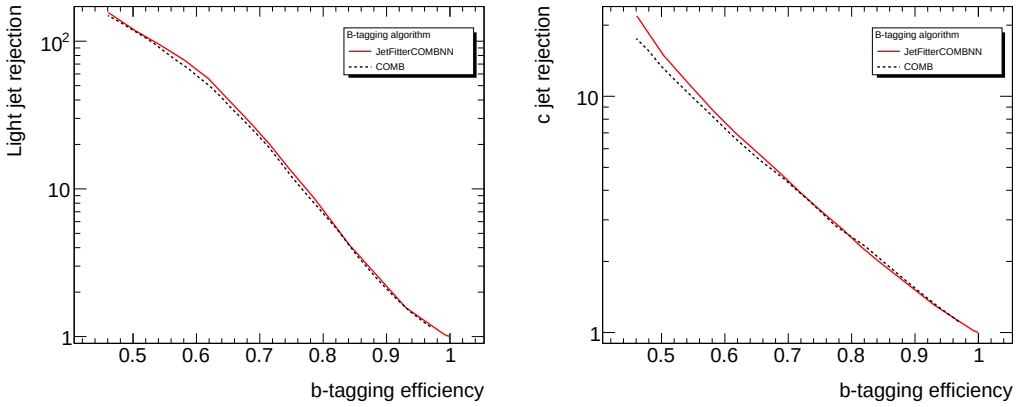

Figure 5.6: Left: Light jet rejection versus b-tagging efficiency of the b-tagging algorithms JetFitterCOMBNN and COMB. Right: c-jet rejection versus b-tagging efficiency of the b-tagging algorithms COMB and JetFitterCOMBNN.

Jet-electron Overlap Treatment

Most electrons are also reconstructed by the jet algorithm due to the electromagnetic showers they leave in the calorimeters. It therefore becomes necessary to identify these jets and remove them in order to avoid double counting. Each jet matching an electron which passed the electron preselection cuts (see Section 5.4.1) within a ΔR of 0.2 and for which the ratio of the electron to the jet transverse momenta is greater than 0.75 [5], is discarded from the sample. About 4% of the jets in the signal sample are removed by this procedure, 99% of them being true electrons.

Low p_T Muons Treatment

About 20% of the time a B-hadron decay cascade gives rise to a muon. With a four b-jet signature in this channel, these so-called *soft muons* are present in about 2/3 of the events [5]. In order to improve the estimate of the momentum of the original b quark, these muons must be used to correct the jet four-momenta by adding the muon four-momentum to a jet. Any muons found within $\Delta R < 0.4$ of the jet axis are considered for addition into the jet. More details and the resulting effects of the jet correction on the reconstructed Higgs boson mass can be found in [5].

Multiplicities and Selection Efficiencies

Additionally to jets originating from the hard process, there can be jets from initial- or final-state gluon radiation which increases the combinatorial problem when assigning reconstructed objects to the particles from the hard process. This is visible when looking at Figure 5.7 (left) which shows the jet multiplicity of all reconstructed jets without any kinematic or quality cuts applied compared to Figure 5.7 (right) which shows all jets with $p_T > 20$ GeV and $|\eta| < 5$. Most of the jets from Figure 5.7 (left) have low momentum and therefore do not pass the preselection cuts. Figure 5.8 shows the number of b-tagged jets (left) and light jets (right) with a momentum $p_T > 20$ GeV and $|\eta| < 2.5$ for b-jets and $|\eta| < 5$ for light jets for signal and background events. The mean number of jets passing the kinematic cuts is 6.3 and on average 2.2 b-jets are found in $t\bar{t}H^0$ events. The jet preselection efficiency for events which passed the lepton preselection in the signal sample is 6.6%, efficiencies for all samples can be found in Table 5.5.

5.5 Trigger Requirements

The presence of one high-p_T lepton, together with missing transverse momentum, is a distinct signature of W boson production. These leptons can generally be used to trigger on W production with high efficiency.

An important concept of the trigger system are the trigger menus. Trigger menus are combinations of objects, which pass different thresholds and are then grouped together depending on the physics they aim to cover. The trigger menu considered here is the menu which was foreseen for a luminosity of 10^{31} cm^{-2}s^{-1}. It contains various relevant lepton trigger signatures but also various jet and missing energy signatures. The signatures considered here are unpresecaled unless stated otherwise. A prescale of N entails that only one in N passed events are sent to the next level for further processing.

Trigger menus are constantly evolving in order to achieve the optimal final efficiencies and rejection factors and will also be updated during the running of the experiment, even when the detector performance is well understood. The study

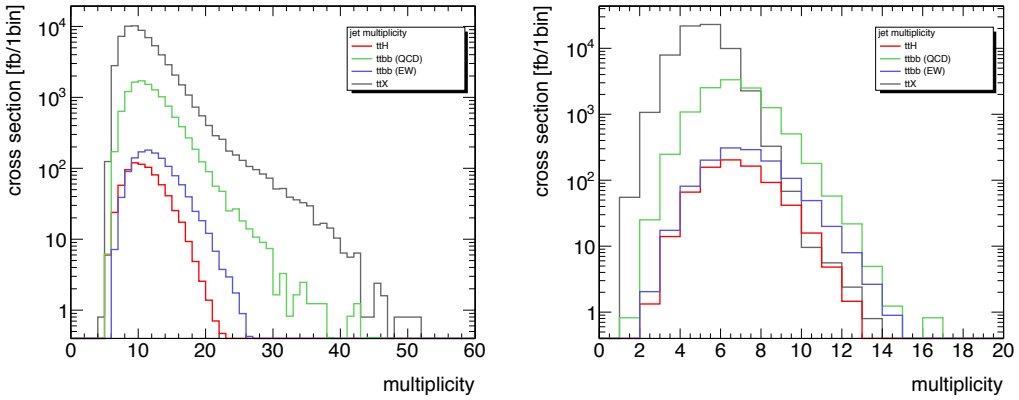

Figure 5.7: Jet multiplicities for all jets (left) and for jets with $p_T > 20$ GeV, reconstructed with the Anti-k_T algorithm. Both distributions are normalised to 30 fb^{-1}.

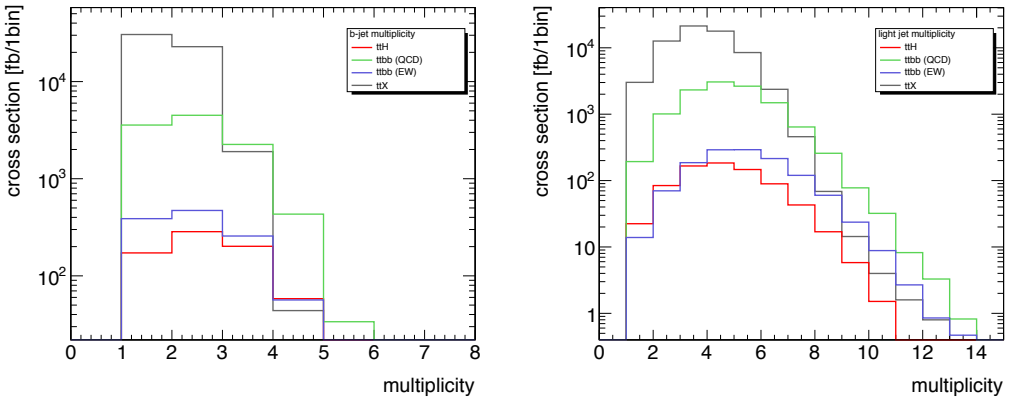

Figure 5.8: Jet multiplicities for b-tagged jets (left) and light jets with $p_T > 20$ GeV, reconstructed with the Anti-k_T algorithm. Distributions are normalised to 30 fb^{-1}.

Step of analysis	$t\bar{t}H^0$	$t\bar{t}b\bar{b}$ EW	$t\bar{t}b\bar{b}$ QCD
Lepton preselection	61.3% (61.3%)	60.3% (60.3%)	59.2% (59.2%)
Jet preselection	6.6% (4.0%)	4.3% (2.6%)	3.4% (2.0%)
Leptonic W	95.7% (3.8%)	96.8% (2.5%)	97.1% (1.9%)
Hadronic W	69.6% (2.7%)	72.7% (1.8%)	68.4% (1.3%)
$t\bar{t}$ system	91.9 % (2.5%)	91.6% (1.7%)	90.6% (1.2%)
Higgs	95.9% (2.4%)	96.3% (1.6%)	97.6% (1.1%)

Step of analysis	$t\bar{t}$+ 0	$t\bar{t}$+ 1	$t\bar{t}$+ 2	$t\bar{t}$+ 3
Lepton preselection	61.7% (61.7%)	60.7% (60.7%)	59.4% (59.4%)	56.6% (56.6%)
Jet preselection	0.03% (0.02%)	0.04% (0.02%)	0.09% (0.05%)	0.2% (0.10%)
Leptonic W	100% (0.02%)	98.9% (0.02%)	95.1% (0.05%)	97.2% (0.10%)
Hadronic W	54.2% (0.01%)	47.7% (0.01%)	52.3% (0.03%)	65.7% (0.06%)
$t\bar{t}$ system	76.9% (0.01%)	90.2% (0.01%)	81.2% (0.02%)	84.1% (0.05%)
Higgs	100.0% (0.01%)	97.3% (0.01%)	91.5% (0.02%)	97.0% (0.05%)

Table 5.5: Efficiencies of each step of the analysis for the signal and $t\bar{t}b\bar{b}$ backgrounds (top) and $t\bar{t}X$ samples ($t\bar{t}$ + 0, 1, 2, 3 extra partons) (bottom). The efficiencies are calculated on a tool-by-tool basis and as cumulative efficiencies in brackets. The Higgs reconstruction efficiency quoted is for the reconstruction method using the two b-jets with the highest b-weight.

presented here is aimed at providing feedback to the ATLAS trigger group in order to optimise the performance of the various trigger signatures.

The efficiencies for the three trigger levels have been studied in the fully-simulated $t\bar{t}H^0$ samples only since the fast-simulated background samples have no trigger simulation. In order to provide feedback of the performance of various lepton signatures, the efficiencies are calculated from events after the preselection. That way, the presence of an offline reconstructed isolated lepton is ensured and the actual signature efficiency is determined.
Furthermore the study of the trigger signatures at this step of the analysis is based on higher statistics than after the $t\bar{t}$ and Higgs reconstruction and the $t\bar{t}$ and Higgs reconstruction have been found to not interfere significantly with the trigger efficiency due to the offline lepton preselection.

The trigger signatures can be classified into categories of which those relevant for this thesis are:

- *Primary trigger*: a trigger used to acquire the data sample for a physics or performance study.
- *Supporting trigger*: a trigger used to measure some property of a primary trigger, including trigger efficiency measurements, monitoring HLT decisions, studying the tracking, studying the isolation for use at higher luminosities and multi-object trigger for use at higher luminosity.
- *Test trigger*: a trigger used only in the Monte Carlo menu for testing purposes.

Following these categorisations the only primary trigger signatures which can be considered for this analysis are the $e20\_loose$ and $mu10$ trigger. For instance, *e20_loose* means that 1 electron with $p_T > 20$ GeV is required and loose calorimeter and tracking identification cuts are applied, whereas *mu10* means that 1 muon with $p_T > 10$ GeV is required. Table 5.6 summarises the L1 item and HLT chains for all considered signatures. Table 5.7 gives the detailed cuts for the primary signatures for each trigger level.

Other signatures which in principle could be used to trigger on $t\bar{t}H^0$ events are the *e20i_loose* (supporting trigger) as well as the test trigger signatures *e25i_loose*, *e25_loose*, *e22i_tight* for electrons and *mu20* and *mu20i_loose* for muons. Each trigger signature consists of a L1 item and L2 and EF chains. Chains are list of sequences at each trigger level, each sequence consisting of executing a series of algorithms.

All these trigger signatures have been studied and their efficiencies have been calculated as:

$$\epsilon = \frac{\text{number of events with a lepton passing the L1/L2/EF trigger}}{\text{number of events with a lepton from a } W \text{ decay (truth)}}. \tag{5.4}$$

Table 5.8 summarises the single electron and single muon trigger efficiencies respectively.

The primary lepton signatures chosen for combination through a logical OR are the *e20_loose* as electron trigger and the *mu10* signature as trigger for muons. Figure 5.9 and 5.10 show the efficiencies for each trigger level versus the p_T and η of the truth lepton in the event for both signatures.

The non-flat efficiency in η of the *e20_loose* L2 and EF chain can be explained by observed losses in the inner detector end-caps in data.

The *mu10* trigger efficiency as a function of η is not completely flat due various inefficiencies around $\eta = 0$. These inefficiencies arise from the geometrical coverage of the muon trigger detector system [16] which limits the overall acceptance for triggering on muons at L1, as shown in Figure 5.11. The barrel trigger system covers approximately 80% of the $|\eta| < 1.0$ region, while the end-cap trigger extends over approximately 96% of the relevant $\eta - \phi$ space. The limitations of the barrel system can be seen in Figure 4.3 and are dominated by the crack at $|\eta| < 0.1$ (largely to accommodate inner-detector and calorimeter services), by the regions occupied by the feet of the experiment at $|\eta| \approx 1$ and by the space taken by the barrel toroid ribs.

The efficiencies for the logical OR combination of the lepton trigger signatures *mu10* and *e20_loose* are given in Table 5.9. The trigger efficiency is approximately 82.0% for those semileptonic $t\bar{t}H^0$ events which would otherwise pass the offline analysis. The trigger efficiencies obtained with the lepton triggers will not be applied to the analysis presented in this thesis to not interfere with the actual reconstruction

Signature	L1 item	HLT chain (L2_ / EF_)	explanation
e20_loose	L1_EM18	e20_loose	1 electron with $p_T > 20$ GeV
e20i_loose	L1_EM18I	e20i_loose	1 isolated electron with $p_T > 20$ GeV
e25_loose	L1_EM18	e25_loose	1 electron with $p_T > 25$ GeV
e25i_loose	L1_EM18I	e25i_loose	1 isolated electron with $p_T > 25$ GeV
e22i_tight	L1_EM18I	e22i_tight	1 isolated electron with $p_T > 22$ GeV
mu10	L1_MU10	mu10	1 muon with $p_T > 10$ GeV
mu20	L1_MU20	mu20	1 muon with $p_T > 20$ GeV
mu20i_loose	L1_MU20	mu20i_loose	1 isolated muon with $p_T > 20$ GeV

Table 5.6: The studied trigger signatures with their corresponding L1 items and HLT chain name.

efficiencies and also to not further limit the statistics of the simulated samples.

5.6 Reconstruction of the $t\bar{t}$ System

To be able to reconstruct the $t\bar{t}$ system, the hadronically and leptonically decaying W bosons have to be reconstructed. b-jets are then associated with the W candidates to form top candidates. All jets considered b-tagged satisfy the weight cut of 1. If more than four b-tagged jets ($W_{jet} > 1$) are found, the jets with the highest weight are used for the reconstruction.

5.6.1 Leptonic W Reconstruction

To fully reconstruct the leptonic W decay, the four-vector of the neutrino momentum has to be reconstructed using the missing transverse energy. Due to the incomplete coverage of the detector around the beam pipe, the z-component of the neutrino momentum p_z cannot be estimated directly from measured quantities. However it is

Trigger level	*e20_loose*	*mu10*
L1	$E_T > 18$ GeV	$E_T > 10$ GeV
L2	E_T(cluster)> 19 GeV	$p_T > 9.8$ GeV for $0 < \|\eta\| \leq 1.05$
	E_T(hadronic) < 3 GeV	$p_T > 9.5$ GeV for $1.05 < \|\eta\| \leq 1.5$
	$R_{\text{core}} > 0.89$	$p_T > 9.6$ GeV for $1.5 < \|\eta\| \leq 2.0$
	$E_{\text{ratio}} > 0.6$	$p_T > 9.7$ GeV for $2.0 < \|\eta\| \leq 2.5$
	p_T(track) > 3 GeV	
	$\Delta\eta$(track-cluster) < 0.03	
	$\Delta\phi$(track-cluster) < 0.15	
EF	$E_T > 20$ GeV	$p_T > 9.77$ GeV for $0 < \|\eta\| \leq 1.05$
		$p_T > 9.67$ GeV for $1.05 < \|\eta\| \leq 1.5$
		$p_T > 9.62$ GeV for $1.5 < \|\eta\| \leq 2.0$
		$p_T > 9.57$ GeV for $2.0 < \|\eta\| \leq 2.5$

Table 5.7: Cuts applied at L1, L2 and EF to the primary trigger signatures *e20_loose* and *mu10*. E_T(cluster) is the transverse energy calculated from the energies in the electromagnetic calorimeter layers in $\Delta\eta \times \Delta\phi = 3 \times 7$, E_T(hadronic) is the leakage into the hadronic calorimeter within $\Delta\eta \times \Delta\phi = 0.2 \times 0.2$. R_{core} is the ratio of energy contained in a $\Delta\eta \times \Delta\phi = 3 \times 7$ window to that in a 7×7 window in the second sampling of the EM calorimeter. E_{ratio} is the ratio of the first energy peak to any second energy peak, to discriminate against $\pi \to \gamma\gamma$ decays. $\Delta\eta$(track-cluster) and $\Delta\phi$(track-cluster) is the difference in η and ϕ between the cluster and the extrapolated track to the calorimeter surface. The transverse energy at EF is calculated using the energies of all EM calorimeter layers in $\Delta\eta \times \Delta\phi = 3 \times 7$.

possible to recover some information by solving the equation for the W boson mass:

$$\begin{aligned} M_W^2 &= (E^\nu + E^l)^2 - (p_x^\nu + p_x^l)^2 - (p_y^\nu + p_y^l)^2 - (p_z^\nu + p_z^l)^2 \\ &= m_l^2 - 2(p_x^\nu p_x^l + p_y^\nu p_y^l) \\ &+ 2E_l\sqrt{((E_T^{miss})^2 + (p_z^\nu)^2)} - 2(p_z^\nu p_z^l) \end{aligned} \tag{5.5}$$

with $p_x^\nu = p_x^{miss}$, $p_y^\nu = p_y^{miss}$ and assuming the neutrino to be massless, $m_\nu = 0$ so that $E_\nu = |\vec{p_\nu}|$. Due to the limited measurement resolution on the transverse

Trigger level	*e20_loose*	*e20i_loose*	*e22i_tight*	*e25_loose*	*e25i_loose*
L1	99.9%	91.4%	91.4%	99.9%	86.1%
L2	80.7%	73.6%	68.6%	75.7%	68.8%
EF	77.4%	72.6%	68.0%	72.1%	67.8%

Trigger level	*mu10*	*mu20*	*mu20i_loose*
L1	91.5%	85.8%	85.8%
L2	88.2%	76.8%	57.3%
EF	86.4%	74.4%	55.3%

Table 5.8: Single electron (top) and muon (bottom) trigger efficiencies for each trigger level. The efficiencies are calculated according to Eq. 5.4 for events with a truth electron or muon from a W d ecay and after the lepton and jet preselection.

Trigger level	*mu10* OR *e20_loose*
L1	(95.6 ± 0.1)%
L2	(84.6 ± 0.1)%
EF	(82.0± 0.1)%

Table 5.9: Efficiencies for the combination of the *mu10* and *e20_loose* trigger using a logical OR. This trigger combination is used to select $t\bar{t}H^0(H^0 \to b\bar{b})$ events.

missing energy, for a significant fraction of events the quadratic constraint equation does not have a real solution. In this case two different approximations can be made: The "($\Delta = 0$) approximation" by dropping the imaginary part of solutions with complex roots or the "collinear approximation" by assuming that the W boson decay products are produced preferentially in the same direction due to the large top quark mass boosting the W boson. For the collinear approximation the assumption $p_z^l = p_z^\nu$ is made.

In the CSC analysis, it was found that 72% of the time $p_{z,\nu}$ has real solutions with a resolution of 19.5 GeV. In this case, both solutions are carried forward into the analysis and the best performing final state solution is used. In the other 28% of cases with no real solutions, the approximations mentioned can be used. In this analysis the "$\Delta = 0$" approximation is used which was found to have a $p_{z,\nu}$ resolution

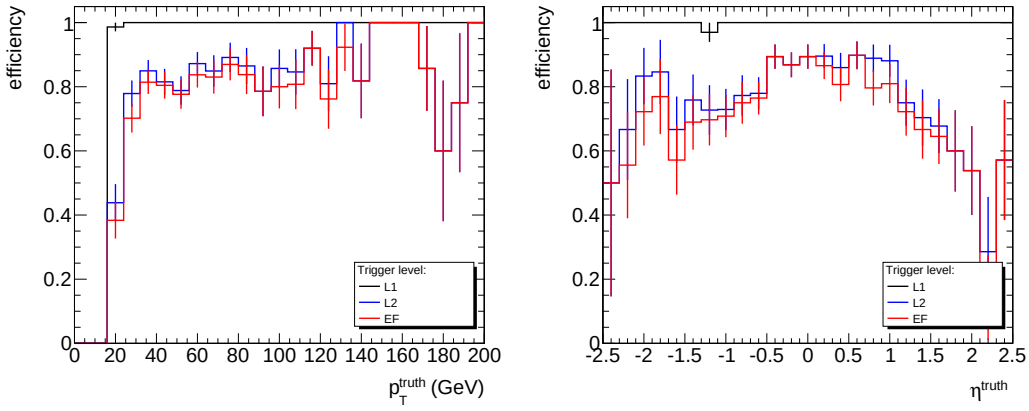

Figure 5.9: Trigger efficiency for each trigger level for the *e20_loose* signature shown for the truth p_T and η of the lepton from the top decay.

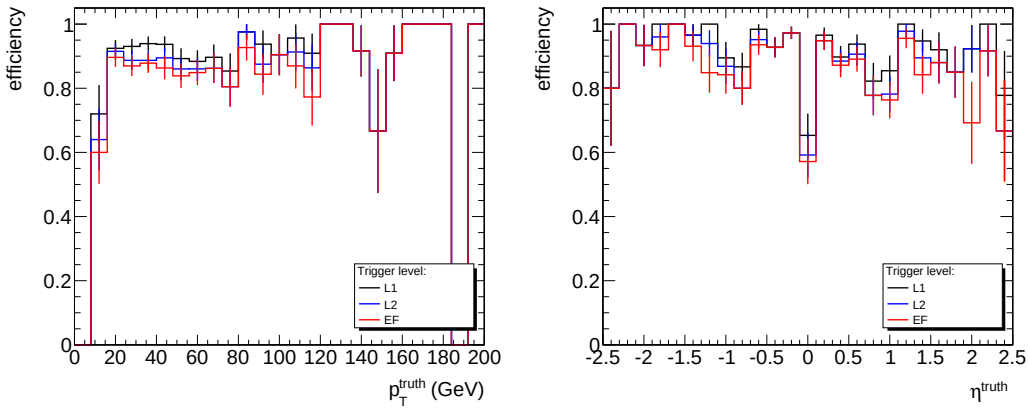

Figure 5.10: Trigger efficiency for each trigger level for the *mu10* signature shown for the truth p_T and η of the lepton from the top decay.

of 40 GeV and therefore to perform better than the collinear approximation where the $p_{z,\nu}$ resolution is 54 GeV.

Since the mass constraint is lost when using the "$\Delta = 0$ approximation" (the same would be true for the collinear approximation), there is an actual cut on the reconstructed W boson mass. To remove extreme cases, only W candidates of $m_W < 140$ GeV are considered [5]. The reconstructed leptonic W boson mass is shown in Figure 5.12 (right) together with the numbers of reconstructed leptonic W candidates per event (left).

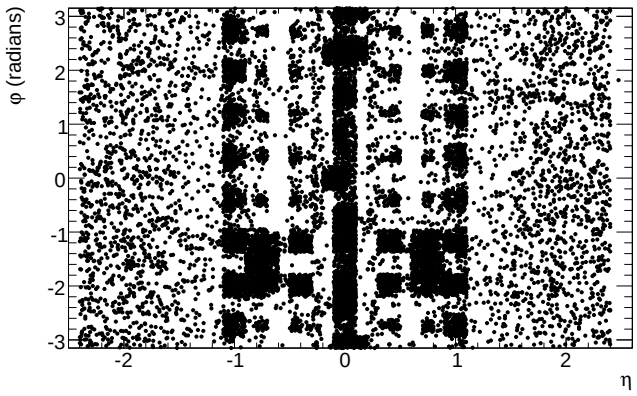

Figure 5.11: Acceptance in the $\eta - \phi$ space for the L1 muon trigger, which covers the η-range $|\eta| < 2.4$. The black points represent regions not instrumented with L1 trigger detectors because of the presence of various supports and services. Taken from [16].

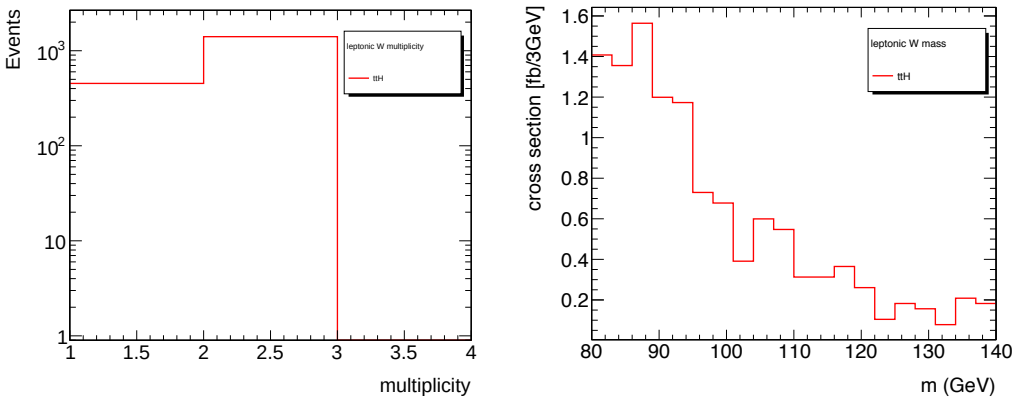

Figure 5.12: Left: Number of reconstructed leptonic W candidates in the signal sample. Right: Invariant mass spectrum of the leptonically decaying W bosons where the "$\Delta = 0$ approximation" is used.

5.6.2 Hadronic W Reconstruction

For the reconstruction of the hadronic W decay only jets not tagged as b-jets are considered. All possible two-jet combinations are formed and jet-pairs within $m_{jj} = m_W \pm 25$ GeV are kept. Due to the many jet-jet combinations, the W candidate multiplicity is rather high, for the signal sample on average about 4 W candidates are

found. Figure 5.13 shows the multiplicity and mass distribution of all W candidates.

In the CSC analysis, the nominal value $m_W = 80.4$ GeV was used to select the reconstructed candidates. Although the jets used for reconstruction are calibrated for instrumental effects with the jet energy scale (JES) being independent of detector effects, they are not corrected for physics effects. There are a number of effects that can contribute to this energy loss such as clustering, fragmentation, initital and final state radiation, underlying event and from energy lost outside the jet (out-of-cone energy) etc. have to be in principle applied [5]. When reconstructing massive objects such as the W boson, the effect of the energy loss of uncalibrated jets will be reflected in a lower mass peak than the nominal W mass. In the CSC analysis, a residual calibration was applied to account for these effects. It was derived from full simulation, so that the jet four-momentum was corrected by a flavour dependent rescaling factor. This calibration improved the mass peak location of the Higgs boson and improved (together with the treatment of low p_T muons) the significance by 0.3. Such a calibration has not been derived and applied to jets in this analysis, instead the mean mass of the reconstructed objects (W and Higgs boson, top quarks) has been determined and the mass window was chosen around this mean mass instead of the nominal value.

Therefore the mean mass of the correctly reconstructed jet pairs is used to place the mass window of ± 25 GeV instead of the nominal W boson mass as in the CSC analysis. Figure 5.14 shows the mass of the reconstructed W candidates, where the correct jets have been used for reconstruction. Based on the Gaussian fit applied, the mass distribution peaks at 75.4 GeV and has a width of 10.9 GeV.

At this point of the analysis all combinations of jet pairs inside the acceptance window are kept and the decision, which pair is chosen for the hadronic W boson reconstruction is made in the process of the top quark reconstruction. The efficiencies for reconstructing the hadronic W boson for signal and background samples are given in Table 5.5.

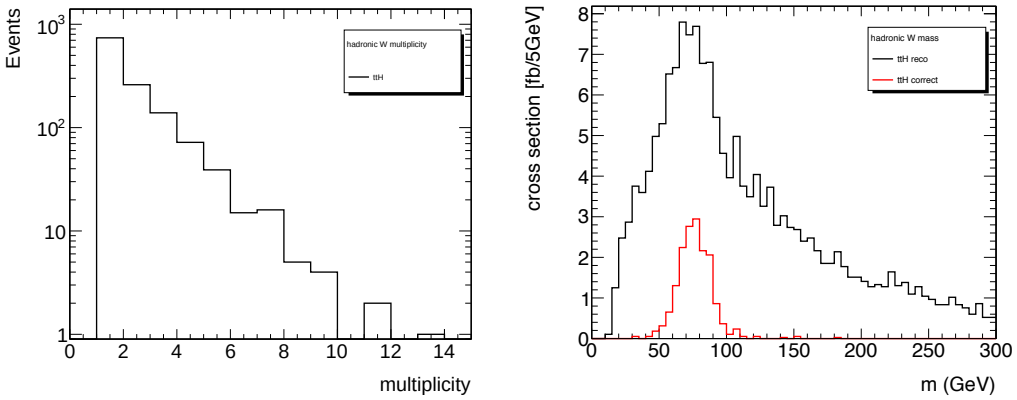

Figure 5.13: Left: Number of reconstructed hadronic W candidates within 25 GeV of the true W mass in the signal sample. Right: Invariant mass spectrum of the two-jet combinations to reconstruct the hadronic W. The red line shows the combinations where the jets from the W are correctly matched.

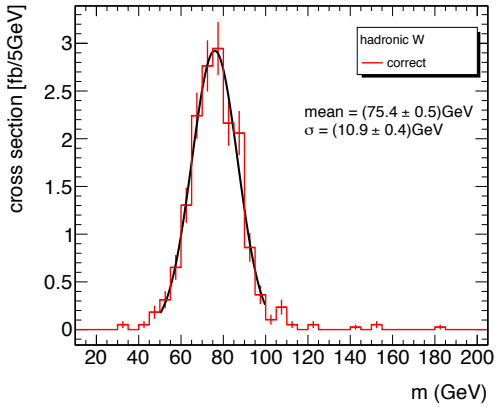

Figure 5.14: Invariant mass spectrum of the correctly reconstructed W candidates to which a Gaussian distribution has been fitted.

5.6.3 $t\bar{t}$ Reconstruction

After the reconstruction of the leptonic and hadronic W decays, the appropriate b-jets from the decay of the top quark have to be found. The reconstruction of the $t\bar{t}$ system is done simultaneously for both top quarks by finding the combination of one charged lepton, the solution for p_z^ν, two b-jets and two light jets which minimise

the χ^2 expressed as:

$$\chi^2 = \left(\frac{m_{jjb} - m_{top}^{had}}{\sigma_{m_{jjb}}} \right)^2 + \left(\frac{m_{l\nu b} - m_{top}^{lep}}{\sigma_{m_{l\nu b}}} \right)^2 \tag{5.6}$$

where $\sigma_{m_{jjb}}$ and $\sigma_{m_{l\nu b}}$ are the reconstructed mass resolutions. Figure 5.15 shows the invariant mass of the reconstructed hadronic and leptonic top candidates where the b-jets have been correctly assigned. The peaks around 130 GeV and 220 GeV in Figure 5.15 (left) might be due to W candidates which have been matched to a truth W boson in ΔR space but do not match in energy. The $\sigma_{m_{jjb}}$ and $\sigma_{m_{l\nu b}}$ have been found to be on average 17.8 GeV and 25.4 GeV respectively based on the Gaussian fit applied. The fit windows have been chosen to be $100 - 210$ GeV for the hadronic and $100 - 200$ GeV for the leptonic top. The nominal top mass of 172.5 GeV is not used in the χ^2 given in Equation 5.6, instead the mean masses of the hadronic and leptonic tops are also taken from the Gaussian fit, so that $m_{top}^{had} = 158.6$ GeV and $m_{top}^{lep} = 163.4$ GeV.

Figure 5.16 shows the resulting distributions of the reconstructed top masses m_{jjb} and $m_{l\nu b}$ for the $t\bar{t}$ system with the smallest χ^2 value. The tails of the mass distributions are dominated by events with incorrect pairing. Such events are rejected by requiring that the reconstructed top quark masses lie within $|m_{jjb} - m_{top}^{had}| <25$ GeV and $|m_{l\nu b} - m_{top}^{lep}| <25$ GeV. A Gaussian fit to the mass peaks for the correctly reconstructed hadronic and semileptonic tops has been applied and the mass peaks for the hadronic and leptonic top mass window cut are found to be $m_{top}^{had} = 160.2$ GeV and $m_{top}^{lep} = 164.4$ GeV (see Figure 5.17).

The efficiencies for the reconstruction of the $t\bar{t}$ system for signal and background samples are given in Table 5.5. For the signal sample, in about 91.9% of events with a hadronic and leptonic W, a the $t\bar{t}$ system can be reconstructed.

5.7 Higgs Reconstruction

The two remaining b-tagged jets are now assigned to the Higgs boson candidate. In case of more than two remaining b-jets, two different approaches are considered: the reconstruction of the Higgs boson with the two highest p_T b-jets (CSC approach) or with the two b-jets with the highest b-weight.

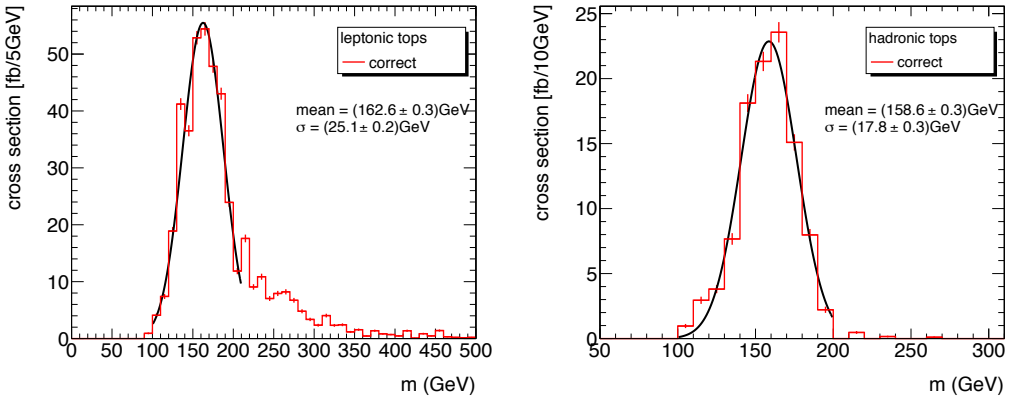

Figure 5.15: Reconstructed invariant masses for all correct hadronic (right) and semileptonic tops (left) for signal events where the b-jet has been assigned correctly. A Gaussian has been fitted to both distributions.

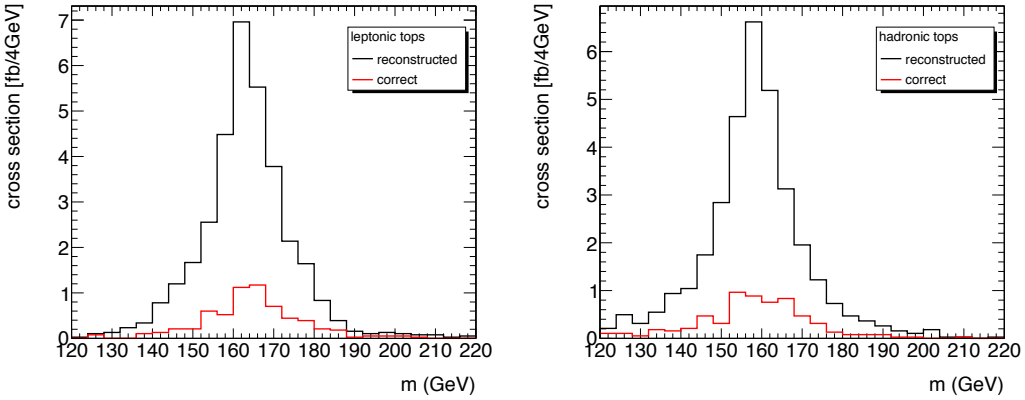

Figure 5.16: Reconstructed invariant mass for selected semileptonic tops (left) and hadronic tops (right) for signal events, forming the best $t\bar{t}$ system found, normalised to 30 fb^{-1}. The red line indicates candidates formed by assigning the correct b-jets to the $t\bar{t}$ system considered.

5.7.1 Transverse Momentum Ordering

The approach of choosing the two highest p_T remaining b-jets and combining them to form a Higgs candidate was used in the CSC analysis. The resulting Higgs boson mass for the signal sample is shown in Figure 5.18 (left) and the signal and background distributions for the invariant Higgs mass are shown in Figure 5.19. Here, no clear mass peak is visible, showing the difficulty of the analysis, requiring

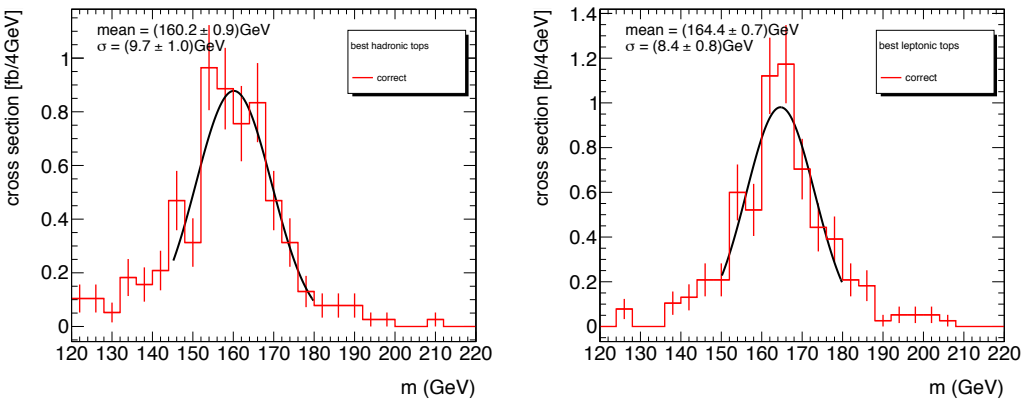

Figure 5.17: Reconstructed invariant mass for selected hadronic tops (left) and semileptonic tops (right) for signal events, forming the best $t\bar{t}$ system found in the event where the correct b-jets has been assigned to the top candidates. A Gaussian fit has been applied to both distributions.

dedicated studies to measure the background normalisation and its shape in data.

For estimating the significance and signal-to-background ratio, the CSC analysis applied a mass window cut of ± 30 GeV around the nominal mass of the Higgs boson for which the signal samples had been generated. Given the uncalibrated jets used to reconstruct the Higgs candidate, a Gaussian fit is applied to those Higgs candidates which have been correctly reconstructed to estimate the mean reconstructed Higgs mass. The result of this fit is shown in Figure 5.18 (right), a mass peak at 108.8 GeV has been found. Based on this, the mass window in which the significance is going to be calculated is chosen to be 80 GeV $< m_H <$ 140 GeV. A significance of is $\frac{S}{\sqrt{B}}$ $= 0.94\sigma$ (1.72σ) and signal-to-background ratio of $\frac{S}{B} = 0.09$ (0.09) for an integrated luminosity of 30 fb^{-1} (100 fb^{-1}) is found.

A Higgs candidate is found in 95.9% of the events which passed the $t\bar{t}$ reconstruction. Out of these events, in 12.4% the correct b-jets have been used for the Higgs candidate reconstruction and 34.3% of the reconstructed candidates were found to lie within the Higgs mass window.

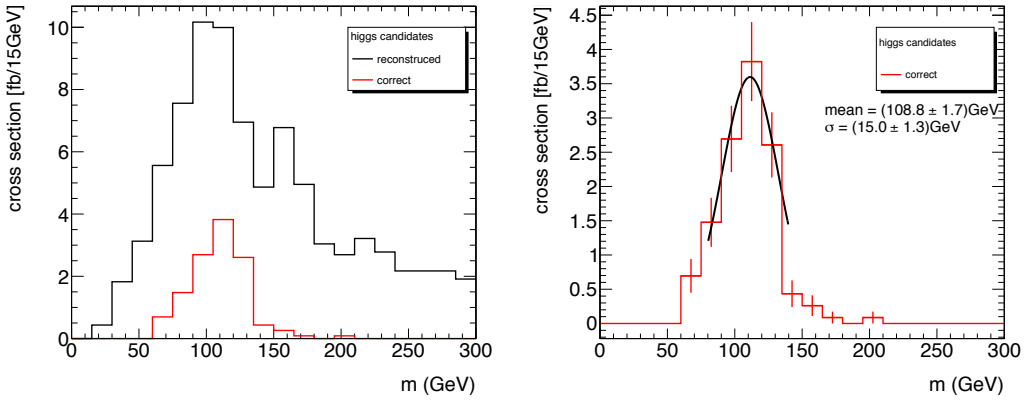

Figure 5.18: Left: Invariant Higgs boson mass reconstructed from the two highest p_T b-jets for the signal sample for $m_{H^0} = 120$ GeV. The red line indicates Higgs candidates formed by assigning the correct b-jets and the distribution is normalised to 30 fb^{-1}. Right: Gaussian fit applied to the correctly reconstructed Higgs candidates (from the highest two p_T jets) formed by assigning the correct b-jets.

5.7.2 b-weight Ordering

An alternative to using the two highest p_T b-jets is to use the pair with the highest b-weights. The reconstructed Higgs boson mass for the signal sample is shown in Figure 5.20 (left). Figure 5.21 shows the reconstructed Higgs mass spectrum for signal and backgrounds after the cut-based selection.

For the final significance estimation of the cut-based analysis and to discriminate against $t\bar{t}$ events where no Higgs boson is produced, only events in a mass window of ±30 GeV around the mean Higgs boson mass of the correct combinations are considered. Figure 5.20 (right) shows the invariant mass of correctly reconstructed Higgs candidates to which a Gaussian fit is applied with a mass peak at 108.7 GeV with a width of 14.5 GeV. This implies a mass window of (110±30) GeV to evaluate the significance, but given the tail towards lower masses of the correctly reconstructed Higgs candidates, a mass window of (105±30) GeV may also be a sensible choice.

The highest significance of this analysis is achieved with a mass window of (105±30) GeV and is found to be $\frac{S}{\sqrt{B}} = 1.10\ \sigma$ (2.01σ) for an integrated luminosity of 30 fb^{-1} (100 fb^{-1}) and a signal-to-background ratio of $\frac{S}{B} = 0.09$ (0.09). The results only vary slightly if the mass window is chosen to be (110±30) GeV

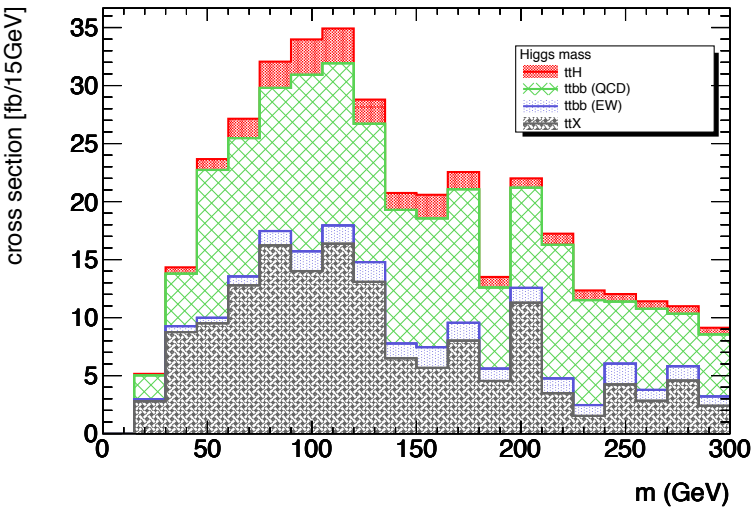

Figure 5.19: The reconstructed Higgs boson mass from the two highest p_T b-jet combination for signal and backgrounds, normalised to 30 fb^{-1}.

with a significance of $\frac{S}{\sqrt{B}} = 1.06\sigma$ (1.95σ) for an integrated luminosity of 30 fb^{-1} (100 fb^{-1}) and a signal-to-background ratio of $\frac{S}{B} = 0.09$ (0.09).

In about 95.9% of $t\bar{t}H^0$ events where the $t\bar{t}$ system has been reconstructed successfully, a Higgs candidate has been found. Out of these events, 44.5% lie within the Higgs mass window of (105±30) GeV. Overall 19.4% of the Higgs candidates were found to be reconstructed from the correct b-jets. The Higgs reconstruction efficiencies of all background samples are given in Table 5.5.

With this Higgs reconstruction, a higher proportion of events are found to lie within the Higgs mass window compared to the CSC analysis as well as a higher fraction of correctly identified Higgs candidates.

5.8 Significance Estimate and Comparison of Results

The statistical significance for the $t\bar{t}H^0(H^0 \rightarrow b\bar{b})$ channel is computed with the number of remaining Higgs candidates (one per event) in the Higgs boson mass window of 30 GeV around Higgs boson mass of (105±30) GeV obtained from a Gaussian fit in Section 5.7.2. Higgs candidates have been reconstructed from the two remaining b-jets with the highest b-weight in the event. This statistical significance for the

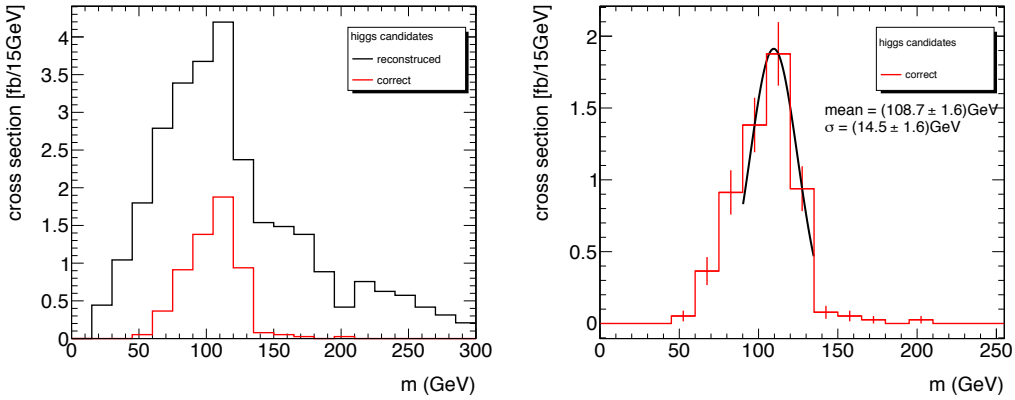

Figure 5.20: Left: Invariant Higgs boson mass reconstructed from the two b-jets with the highest b-weight for the signal sample for $m_{H^0} = 120$ GeV, the red line indicates Higgs candidates formed by assigning the correct b-jets. The distribution is normalised to 30 fb^{-1} Right: Gaussian fit applied to the correctly reconstructed Higgs candidates formed by assigning the correct b-jets.

$t\bar{t}H^0(H^0 \to b\bar{b})$ channel in which the signal and backgrounds are very much alike, is not the most relevant figure of merit, but it is still useful to compare this analysis to the CSC analysis [5] and the boosted $t\bar{t}H^0$ analysis presented in Chapter 7.

Table 5.10 summarises the number of signal and background events found for the analysis using the highest b-weighted jets to reconstruct the Higgs candidate for an integrated luminosity of 30 fb^{-1} and 100 fb^{-1}. A significance of 1.1σ and 2.01σ for an integrated luminosity of 30 fb^{-1} and 100 fb^{-1}, respectively, is achieved with a signal-to-background ratio of 0.09.

integrated luminosity	Signal	Backgrounds			S/B	$S/\sqrt{B}$
		$t\bar{t}b\bar{b}$ QCD	$t\bar{t}b\bar{b}$ EW	$t\bar{t}X$		
30 fb^{-1}	13.6	67.0	11.2	75.0	0.09	1.10
100 fb^{-1}	45.4	223.4	37.2	249.9	0.09	2.01

Table 5.10: Number of signal and background events, signal-to-background ratio S/B and the statistical significance $S/\sqrt{B}$ for the analysis presented in this thesis using the highest b-weighted jets for the Higgs reconstruction and a mass window of (105±30) GeV for an integrated luminosity of 30 fb^{-1} and 100 fb^{-1}.

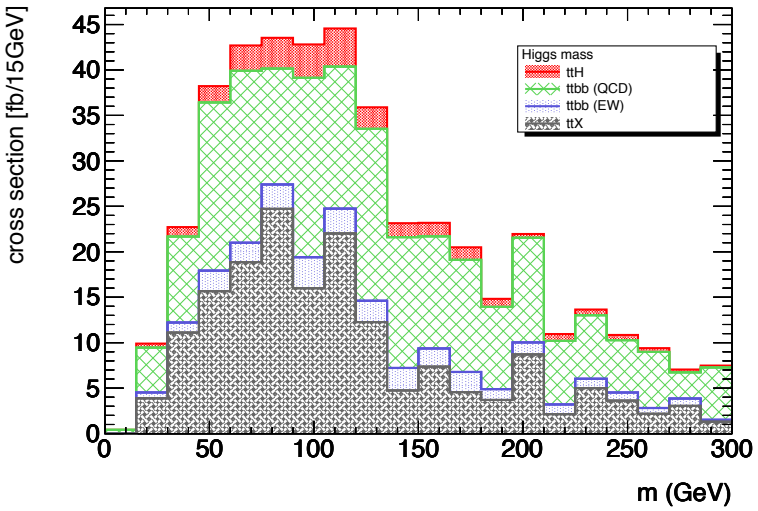

Figure 5.21: The reconstructed Higgs boson mass from combining the two b-jets with the highest b-weight for signal and backgrounds, normalised to 30 fb^{-1}.

In order to compare the results of the analysis carried out in this thesis to the cut-based CSC analysis, a scaling factor has to be applied due to the different centre-of-mass energies at which the simulated data has been generated and therefore different cross-sections of the samples. This cross-section scaling factor was determined to be 2.05 between the 10 TeV and 14 TeV sample (see Section 5.2.2). Therefore to obtain the significance for a centre-of-mass energy of 14 TeV, the analysis presented here has to be scaled by a factor of $\sqrt{2.05} = 1.43$, resulting in a statistical significance of $\frac{S}{\sqrt{B}} = 1.57$ for an integrated luminosity of 30 fb^{-1}.

The significance achieved with the cut-based CSC analysis was found to be 1.82 with a signal-to-background ratio of 0.11 for an integrated luminosity of 30 fb^{-1} at a centre-of-mass energy of 14 TeV.

The results of the analysis presented in this thesis and the result obtained with the cut-based CSC analysis are not in perfect agreement, with the presented analysis performing slightly worse. However, there are various differences in Monte Carlo samples used in the analyses, as well as in the reconstruction of the events, which can explain those discrepancies. The Monte Carlo datasets used in the CSC analysis

have been generated with different generators and settings: The $t\bar{t}H^0(H^0 \rightarrow b\bar{b})$ sample was generated in same same way as the sample used in this analysis. It has been generated with PYTHIA 6.403 and a lepton filter was applied, requiring at least one lepton (electron or muon) with pseudorapidity $|\eta| < 2.7$ and transverse momentum $p_T > 10$ GeV.

For both $t\bar{t}b\bar{b}$ QCD and EW samples AcerMC (version 3.4 for $t\bar{t}b\bar{b}$ QCD and version 3.3 for $t\bar{t}b\bar{b}$ EW for the hard process) was used and interfaced to PYTHIA 6.403 for the initial and final state radiation, hadronisation and decay. The lepton filter is also applied to these samples. In this analysis, only the EW $t\bar{t}b\bar{b}$ sample has been generated with AcerMC, interfaced to PYTHIA, while the QCD $t\bar{t}b\bar{b}$ sample has been generated with ALPGEN and interfaced to HERWIG (see Section 5.2.1 for more details). The reducible $t\bar{t}$ background events are generated with the MC@NLO [63] 3.1, interfaced to HERWIG 6.510 (parton showering, hadronisation) and Jimmy (underlying event). The lepton filter is applied with an increased cut on the transverse momentum of p_T >14 GeV compared to the filter applied in this analysis. Additionally, requirements on jets are applied which are reconstructed using a seeded-cone algorithm with a cone size of $\Delta R = 0.4$. At least six jets with $p_T > 14$ GeV and $|\eta| > 5.2$ and four jets with $p_T > 14$ GeV and $|\eta| > 2.7$. The $t\bar{t}$ background in this thesis has been generated at LO with ALPGEN interfaced to HERWIG, with the TtbarPlusJetsFilter applied (see Section 5.2.1 for details).
The properties and settings of the samples generated for the CSC analysis and the analysis presented here are summarised in Table 5.11, as well as the cross-sections for each sample. The biggest reason for the difference of cross-sections of the different samples is the centre-of-mass energy used to generate the samples.

To have a common factorisation and renormalisation scale Q in the simulated datasets used for this thesis, it has been scaled to $Q = 232.5$ GeV for all samples, while no common scale has been chosen to the samples used in the CSC analysis. While the full cross-section of a process is independent of the scale Q^2, the lower order approximations used on the way to an all-orders calculation can strongly depend on the chosen scale [64], [59]. A sensible choice of Q^2 is therefore important when generating events at leading order (LO). The Q^2 value should reflect the

energy scale of the physical final state and is generally chosen to be around half the transverse mass of the final state. This choice is based on observations that lower values of Q^2 result in a LO cross-section that is closer in magnitude to that obtained at higher orders.

Another more general difference between the simulated datasets of the current analysis and the CSC analysis is the top quark mass used in the generation. The CSC samples have been generated with a top mass of $m_t = 175$ GeV, while the samples from the current analysis have been generated with a top mass of $m_t = 172.5$ GeV. Figure 5.22 shows the total $t\bar{t}$ cross-section as a function of the top mass m_t. Using a top mass of $m_t = 172.5$ GeV will result in a cross-section which is roughly 10% higher than generating $t\bar{t}$ events with a top mass of $m_t = 175$ GeV.

The overlap arising for the separate generation of the $t\bar{t}X$ and $t\bar{t}b\bar{b}$ (QCD) backgrounds has been treated differently in both analyses. The approach in the CSC analysis was to remove all events with b-quarks from the $t\bar{t}X$ sample resulting in removing about 10% of the events from the $t\bar{t}X$ sample. The approach taken in this analysis was to distinguish between the origin of the b-quarks coming from the hard process or the underlying events (see Chapter 6 for details). With the new and more refined approach 5.6% of the events have been identified as $t\bar{t}b\bar{b}$ events and have been removed and the difference in significance between applying and not applying the overlap removal to the $t\bar{t}X$ sample has been found to be 0.02σ higher when applying the overlap removal. This means that in the CSC analysis, events which could have potentially passed the final selection have been removed, underestimating the background contribution of the $t\bar{t}X$ background. Unfortunately a difference in significance between applying and not applying the overlap removal to the $t\bar{t}X$ of the CSC analysis had not been evaluated at that time, therefore no estimate of how much this contributes to the observed difference in significance between the two analyses can be made, however it is expected to be rather small.

To account for higher order effects (next-to-leading order (NLO), next-to-next-to-leading order (NNLO) etc.), cross-sections are typically multiplied by a k-factor which usually takes values between 1 and 2. The cross-sections for the processes considered in this analysis have been calculated at leading order. No k-factors have

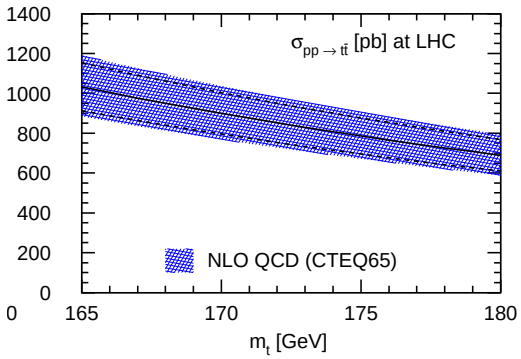

Figure 5.22: The $t\bar{t}$ cross-section to next-to-leading oder (NLO) QCD as a function of m_t at the LHC. The solid line is the central value for $\mu = m_t$, the dashed lower and upper lines correspond to $\mu = 2m_t$ and $\mu = m_t/2$, respectively. The band denotes the additional PDF uncertainty of the CTEQ6.5 set. Taken from [65].

been applied. In the CSC analysis most processes have been calculated to leading order (LO) with the exception being the $t\bar{t}X$ sample in the CSC analysis which has been generated at NLO.

As for more reconstruction-specific differences between the analyses, the dominant differences lie within the jet reconstruction. The jet reconstruction algorithm was chosen to be a seeded fixed-cone algorithm with a cone size of $\Delta R = 0.4$ for the CSC analysis, while for the analysis presented in this thesis the Anti-k_T algorithm with a R-parameter of 0.4 has been chosen. The Anti-k_T algorithm has been found to exhibit the best jet reconstruction efficiency for small and large jets at low p_T [55]. In particular, it gives the best performance for event topologies with close-by jets and the smallest flavour dependence. For high p_T isolated jets, all algorithms perform well. Specifically for the Higgs reconstruction in the $t\bar{t}H^0$ channel, the Anti-k_T algorithm gives the best mass reconstruction and the highest signal efficiency. However, the study carried out in [55] does not evaluate the efficiencies of the backgrounds nor the difference in significance when using Anti-k_T jets, so it is unclear whether usage of Anti-k_T jets actually improves the significance.

Finally, in the CSC analysis, an improvement in significance of 0.3 was found by adding low p_T muons and the residual jet calibration. The jet calibration is Monte

CSC analysis at $\sqrt{s} = 14$ TeV				
Process	Generator	σ (fb)	Factorisation and Renormalisation Scale	PDF set
$t\bar{t}H^0$ (LO)	Pythia	100	$Q^2 = m_t^2 + \max(p_{T,t}^2, p_{T,\bar{t}}^2)$	CTEQ6L1
$t\bar{t}b\bar{b}$ QCD (LO)	AcerMC, Pythia	2371	$Q = m_H/2 + m_t$ $= 232.5$ GeV	CTEQ6L1
$t\bar{t}b\bar{b}$ EW (LO)	AcerMC, Pythia	255	$Q = m_H/2 + m_t$ $= 232.5$ GeV	CTEQ6L1
$t\bar{t}X$ (NLO)	MC@NLO, HERWIG	109487	$Q^2 = m_t^2 + \frac{1}{2}(p_{T,t}^2 + p_{T,\bar{t}}^2)$	CTEQ6M
Analysis at $\sqrt{s} = 10$ TeV				
$t\bar{t}H^0$ (LO)	Pythia	41.49	$Q^2 = \max(p_{T,t}^2, p_{T,\bar{t}}^2)$	CTEQ6L1
$t\bar{t}b\bar{b}$ QCD (LO)	ALPGEN, HERWIG	661.53	$Q = m_H/2 + m_t$ $= 232.5$ GeV	CTEQ6L1
$t\bar{t}b\bar{b}$ EW (LO)	AcerMC, Pythia	70.99	$Q^2 = \hat{s}$	CTEQ6L
$t\bar{t}X$ (LO)	ALPGEN, HERWIG	30921.95	$Q^2 = \sum m_T^2$	CTEQ6L1

Table 5.11: Summary of the different samples used for the CSC analysis (top) and for the cut-based analysis presented in this thesis (bottom). The cross-sections include the branching fractions and filter efficiencies (see Section 5.2) and the scaling to Q = 232.5 GeV (bottom only). A Higgs mass of $m_H = 120$ GeV and a top mass of $m_t = 175$ GeV (CSC) ($m_t = 172.5$ GeV for this analysis) are used. $\max(p_{T,t}^2, p_{T,\bar{t}}^2)$ corresponds to the higher of the two values of p_T^2 when both the top and anti-top quark are considered. Taken from [5].

Carlo based and has been derived to take residual calibrations such as out-of-cone and neutrinos into account. Such a calibration has not been applied at the stage of the jet preselection. Therefore it is likely that fewer jets and therefore events pass the jet preselection cuts. Lowering the p_T cut on the jets is not possible because a cut on light jets of p_T(light jets) > 20 GeV has been applied to the $t\bar{t}X$ samples.

To correct for the effects of using non-calibrated jets, later on in the analysis the mass window cuts for the W boson, the top and the Higgs boson have been adjusted to the mean mass found by fitting a Gaussian distribution to the correctly reconstructed objects.

5.9 Systematic Uncertainties

The systematic uncertainties affecting this channel are of vital importance to this analysis and a comprehensive treatment was made in the CSC study, which will be summarised here. A robust method to determine background shapes and normalisation from data is necessary and still has to be developed. While the theoretical uncertainties for the signal and background normalisation are quite large, their impact can be reduced by making direct measurements in data.

The estimation of systematic uncertainties due to the standard detector effects is summarised in Table 5.12. It is noticeable how important the jet uncertainties are for both signal and background. Indeed the knowledge of the jet energy and of the b-tagging performance have a crucial impact on the kinematic quantities used for the reconstruction of the $t\bar{t}$ system and for the correct identification of the b-jets used for the analysis. The lack of statistics for the $t\bar{t}X$ sample give rise to large fluctuations on the background estimations, resulting in a relative statistical error up to 20%. The large systematic uncertainties estimated in Table 5.12 provide a clear indication that a data driven background estimation is necessary. The knowledge of the jet energy and of the b-tagging performance have a crucial impact on the kinematic quantities used for the reconstruction of the $t\bar{t}$ system and for the correct identification of the b-jets used for the analysis. Large fluctuations on the background estimations arise due to the lack of statistics for the $t\bar{t}X$ sample, giving rise to a relative statistical error up to 20%.

To understand how the background uncertainty propagates into the sensitivity of this channel, the statistical uncertainty on the background $\sqrt{B}$ is summed up in quadrature with the systematic uncertainty ΔB. The corrected significance then takes the form $\frac{S}{\sqrt{B+\Delta B}}$. This corrected significance is shown in Figure 5.23 as a function of $\frac{\Delta B}{B}$. The statistical significance of 1.1σ is found to be reduced to about

Source		signal	background
Electron	energy scale	± 0.5%	± 2%
	resolution	± 0.5%	± 0.6%
	efficiency	± 0.2%	± 2%
Muon	energy scale	± 0.7%	± 3%
	resolution	± 0.8%	± 0.6%
	efficiency	± 0.3%	± 0.1%
Jet	energy scale	± 9%	± 5%
	resolution	± 0.3%	± 7%
	b-tag	± 16%	± 20%
	b-mis-tag	± 0.8%	± 5%
summed in quardature		± 18%	± 22%

Table 5.12: Effect of the various systematic uncertainties on the signal and background efficiencies. Taken from [5].

0.7σ in the case of a 10% uncertainty and to roughly 0.4σ in the case of a 20% uncertainty on the background for an integrated luminosity of 30 fb^{-1}.

5.10 Conclusion

The analysis presented here is a baseline sensitivity study for the detection of a Standard Model Higgs boson in the $t\bar{t}H^0(H^0 \rightarrow b\bar{b})$ channel. After a preselection to ensure the presence of the fundamental objects in the event, a cut-based analysis has been carried out, based on the reconstruction of the W candidate masses, $t\bar{t}$ system and finally the Higgs candidates in the remaining events.
The statistical significance obtained is 1.10 (2.01) for an integrated luminosity of 30 fb^{-1} (100 fb^{-1}) at a signal-to-background ratio of 0.09. When scaling the results from 10 TeV to 14 TeV, a significance of 1.57 for an integrated luminosity of 30 fb^{-1} is obtained.

The results presented in this thesis can be compared with a previous ATLAS study [5] performed at a centre of mass energy of $\sqrt{s} = 14$ TeV which resulted in a significance of 1.82 and a signal-to-background ratio of 1.1 for an integrated

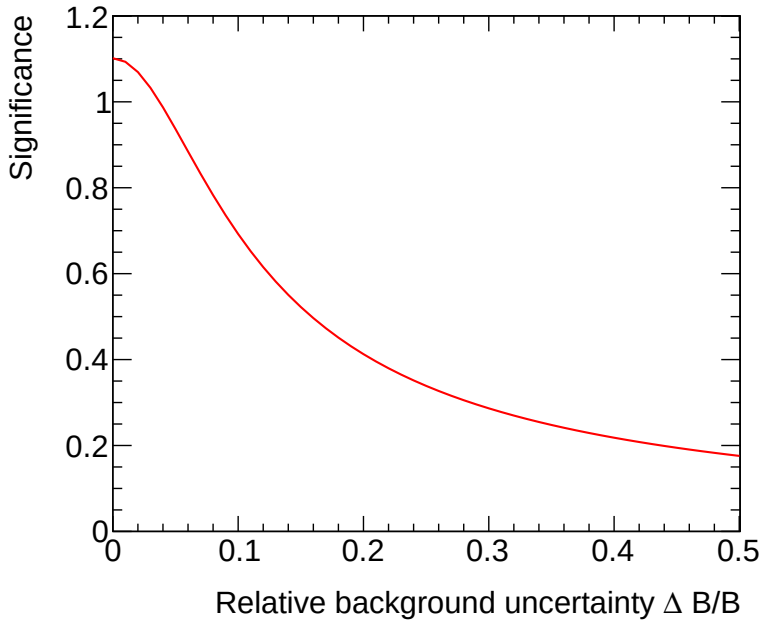

Figure 5.23: Discovery significance for a 120 GeV Higgs boson as a function of the systematic uncertainty on the background $\frac{\Delta B}{B}$ for an integrated luminosity of 30 fb^{-1} for the cut-based analysis. No further systematic uncertainties are considered here.

luminosity of 30 fb^{-1}. The main differences are discussed in Section 5.8 and are namely the different generators used for the Monte Carlo production, a refined $t\bar{t}b\bar{b}$ overlap removal procedure (see Chapter 6) and the lack of jet calibration.

One of the possible areas for improvement for this analysis is the development of a strong b-tagging algorithm which is important to suppress the $t\bar{t}X$ background and also helps to reduce the combinatorial background by improving the hadronically decaying W boson and the Higgs candidates. Furthermore, as the result of the reconstruction of the Higgs candidates using the two highest b-weighted jets performs better than when using the two highest p_T jets, more studies can be made in terms of varying the b-weight cut on preselected jets, as well as jets used for the $t\bar{t}$ and Higgs reconstruction.

Additionally to improving the analysis, different ways of reconstructing the $t\bar{t}H^0$ channels can be exploited as well. A recent study has shown that exploiting a highly boosted Higgs boson can help to indeed extract this channel with a reasonable statistical significance and a much reduced sensitivity to systematics. The implementation

of this analysis in the ATLAS environment and the results are described in Chapter 7 of this thesis. Chapter 8 then studies the complementarity of the low p_T analysis, described in this chapter, and high p_T analysis, described in Chapter 7, and how a combination of the two analyses can improve the significance.

Chapter 6

Removal of the Overlap between the Matrix Element and Parton Shower in $t\bar{t}X$ Backgrounds

6.1 Introduction

The main background for the $t\bar{t}H^0(H^0 \to b\bar{b})$ process is the production of $t\bar{t}$ events. This background can be divided into a reducible and an irreducible component, depending on whether or not the final state particles are identical to those in $t\bar{t}H^0(H^0 \to b\bar{b})$ (see Section 3.4.4).

The reducible background is the $t\bar{t}$ background with extra jets from the hadronisation of light quarks and will be described as the $t\bar{t}X$ background in the following, whereas the irreducible background arises from $t\bar{t}b\bar{b}$ production via QCD and electroweak (EW) interactions.

To be able to study the contributions and behaviour of these backgrounds individually (especially with respect to their different b-tagging response), they are all simulated separately from each other, resulting in three different Monte Carlo (MC) samples: the reducible $t\bar{t}X$ sample and the irreducible samples $t\bar{t}b\bar{b}$ (EW) and $t\bar{t}b\bar{b}$ (QCD).

However, this creates an overlap of events since the addition of b-quarks to $t\bar{t}$ events via parton showering in HERWIG produces events that are included in the

matrix-element cross-section calculation for the $t\bar{t}b\bar{b}$ sample. This is illustrated in Figure 6.1 which shows example Feynman diagrams for events in which the b-quark pair could be produced by parton showers or matrix elements and can be found in both MC samples.

This chapter describes a new procedure for the overlap removal developed for the study of the $t\bar{t}H^0(H^0 \to b\bar{b})$ channel as an improvement to the technique used in the CSC analysis [5].

Section 6.2 gives a brief description of the parton shower and matrix element approaches. The generated background samples which are relevant for this study are described in Section 6.3, Section 6.4 gives details about the identification of overlapping events and Section 6.5 describes the effect of the overlap removal on the $t\bar{t}H^0(H^0 \to b\bar{b})$ analysis. Section 6.6 contains a discussion of these results and prospects for future background treatments in $t\bar{t}H^0$.

6.2 Parton Shower and Matrix Elements

Monte Carlo event generators model events in different stages as briefly described in chapter 4.2.

There are two ways of modelling partons in an event: One is to include them in the hard process and calculate the hard interaction and its cross-section perturbatively using the matrix element approach. Matrix element calculations give a description of a specific parton topology, which is valid when the partons are energetic and well separated. Furthermore, it includes interference between amplitudes with the same external partons but different internal structure. However, for soft and collinear kinematics, the description in terms of a fixed order of emissions is not valid, because it does not include the interference between multiple gluon emissions which cannot be resolved. The latter effect is known as *Sudakov suppression*. However, the computational work required for this increases approximately factorially with the order, so it is not realistically possible to calculate high-multiplicity events using purely this method.

Another way to add partons to an event is through parton showers. Here the

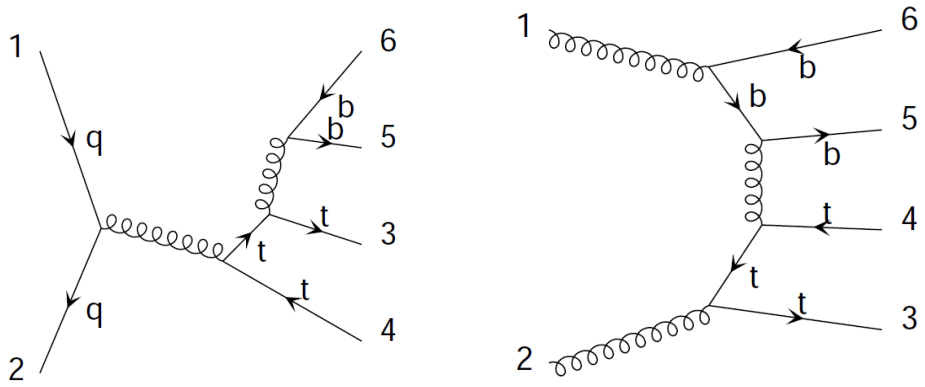

Figure 6.1: Example of events in which the b-quark pair could be produced by either parton showers or matrix elements (left) and which would only be found in a matrix element $t\bar{t}b\bar{b}$ sample (right) [66].

starting point is a fixed-order matrix element calculation with a final state of n_{ME} partons. The parton shower acts iteratively by causing successive $i \to jk$ branchings, driven by an *evolution variable*. This variable can either be the virtuality of the incoming parton (for Q^2 ordered parton showers), the relative transverse momentum of the two partons (p_T ordered) or the angle between the two partons.

Specifically, the HERWIG parton shower evolution is done in terms of the parton energy fraction $z_j = \frac{E_j}{E_i}$ and an angular variable $x_{jk} = \frac{(p_j \cdot p_k)}{(E_j E_k)}$. The values of z are chosen according to the *Altarelli-Parisi splitting functions* [67, 68] which mathematically express the probability of gluon radiation ($q \to qg$) and gluon splitting ($g \to gg$) taking place. The distribution of x_{ij} values is determined by the *Sudakov form factor*. The Sudakov form factor expresses the probability that no splittings take places between a starting scale Q_{start} and the splitting scale Q_{split}. It basically normalises the branching distributions to give the probabilistic interpretation needed for a Monte Carlo simulation.

The full available phase space is restricted to an angular-ordered region. Angular ordering implies that each x value must be smaller than the x value for the previous branching of the parent parton.

In our case, the $t\bar{t}b\bar{b}$ (QCD) events are generated using the matrix element calculations. However, it is possible that events with the same final state arise from

parton showers in the $t\bar{t}X$ sample. This overlap between the two samples has to be removed to avoid overestimating the background contribution for this channel.

6.3 Monte Carlo Samples and Cross-sections

The simulated signal and background samples used in this study have been described in detail in Section 5.2. All samples have been generated at leading order with a centre-of-mass energy of 10 TeV, a Higgs boson mass (m_H) of 120 GeV and a top quark mass (m_{top}) of 172.5 GeV. Tables 5.2 and 5.3 summarise the relevant samples for this study, the irreducible $t\bar{t}b\bar{b}$ QCD background and the reducible $t\bar{t}X$ background.

6.4 Identification of Overlapping Events and their Removal

After HERWIG and JIMMY have run, the events are converted to a HepMC event record [69] which stores the events in a graph structure, physically similar to a physics event as shown in Figure 6.2. Entries within the event record are separated into particles and vertices. The vertices are the connection nodes between particles and are a container class for particles. Therefore each particle belongs to at least one vertex. Particles and vertices are, amongst other things, composed of a particle identification number, status information and a unique *barcode*. The barcode is an integer which is meant to be a persistent label for a particular instance.

The approach taken in this study to identify the overlap is to first look at the number of all pairs of b-quarks originating from a common vertex. Events with one or more such $b\bar{b}$ pairs could reasonably be considered as overlap events and removed from the $t\bar{t}X$ background.

Figure 6.3 shows the multiplicity of all $b\bar{b}$ pairs found for each $t\bar{t}X$ sample (right) and compares the $b\bar{b}$ pair multiplicity for the $t\bar{t}X$ and $t\bar{t}b\bar{b}$ backgrounds. The background samples have been scaled according to their cross-sections. It is clear that the number of b pairs increases with the number of extra partons. Events from the $t\bar{t}b\bar{b}$ sample have a minimum of one $b\bar{b}$ pair as expected, since there must be one pair

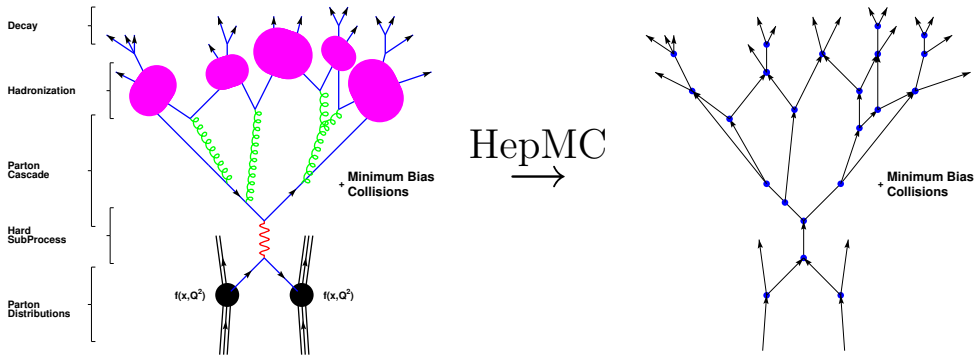

Figure 6.2: Events in the HepMC are stored in a graph structure (right), similar to a physicist's visualisation of a collision event (left). Taken from Ref. [69].

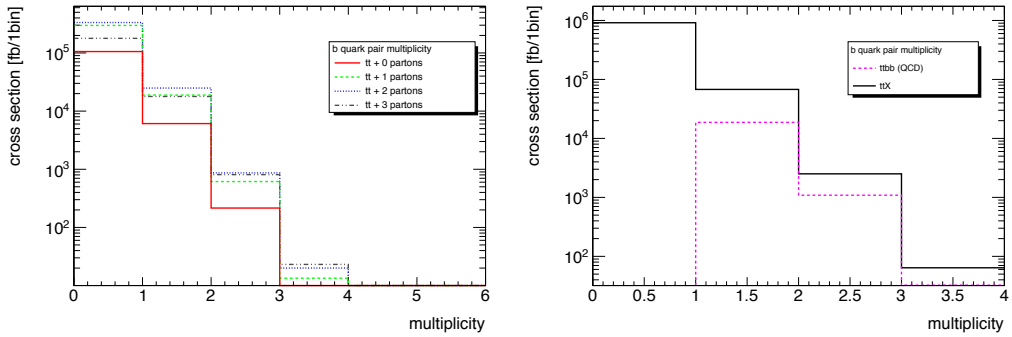

Figure 6.3: Multiplicity of $b\bar{b}$ pairs comparing all $t\bar{t}$ backgrounds (left) and the $t\bar{t}X$ and $t\bar{t}b\bar{b}$ backgrounds (right). These histograms include $b\bar{b}$ pairs from the underlying event.

produced in the hard process.

It is also found that b-pairs can originate from the additional $g - g$ interaction vertices put in by JIMMY to model underlying event. $b\bar{b}$ pairs originating from such a vertex should not be considered in the overlap removal procedure as they do not form part of the diagrams contributing to the $t\bar{t}b\bar{b}$ matrix element calculation.

Figure 6.4 shows a sketch of a proton-proton collision at high energies. The signal (hard) process is shown in red, the underlying event in pink. The additional scatters from the underlying event can be easily identified in the HepMC record as particles with the id 0 and status 120, which represent the total 4-momentum of the

Process	$t\bar{t}$+0p	$t\bar{t}$+1p	$t\bar{t}$+2p	$t\bar{t}$+3p	$t\bar{t}X$	$t\bar{t}b\bar{b}$
Dataset	109620	109621	109622	109623		109627
total number of events	140321	378529	412334	238391	1169575	48275
overlapping events	5422	17924	24660	20005	68011	
(in %)	3.86%	4.74%	5.98%	8.39%	5.57%	
$t\bar{t}b\bar{b}$ cross-section (fb)	144.23	500.05	716.35	549.25	1909.88	661.53

Table 6.1: Cross-sections of the removed overlap events from the simulated $t\bar{t}X$ background compared to the total cross-section of the $t\bar{t}b\bar{b}$ sample.

centre-of-mass frame of the extra vertex.

Taking this into account, the $t\bar{t}b\bar{b}$ overlap sample is now defined as $t\bar{t}X$ events that contain at least one $b\bar{b}$ pair whose parent does not have id 0 and status 120.

Table 6.1 summarises the cross-sections of the overlap events for the $t\bar{t}X$ background. As a cross check we can compare the cross-section of the removed events with the cross-section of the full $t\bar{t}b\bar{b}$ background sample (see Table 6.1). We find the $t\bar{t}X$ overlap cross-section to be almost 3 times larger than the $t\bar{t}b\bar{b}$ sample. This large disparity may be due to the fact that b-quarks added by parton showers are more likely to be softer and collinear than those predicted by the matrix element approach. In high multiplicity final states such as $t\bar{t}H^0(H^0 \to b\bar{b})$, where the number of emitting partons is higher, we may expect this effect to be most significant. This is discussed further in Section 6.6.

To minimise the effect of the different b-quark kinematics between the two samples, we compare the cross-sections after applying the jets and lepton preselection of the semileptonic $t\bar{t}H^0(H^0 \to b\bar{b})$ analysis. A description of the analysis and the resulting cross-sections are given in the following section.

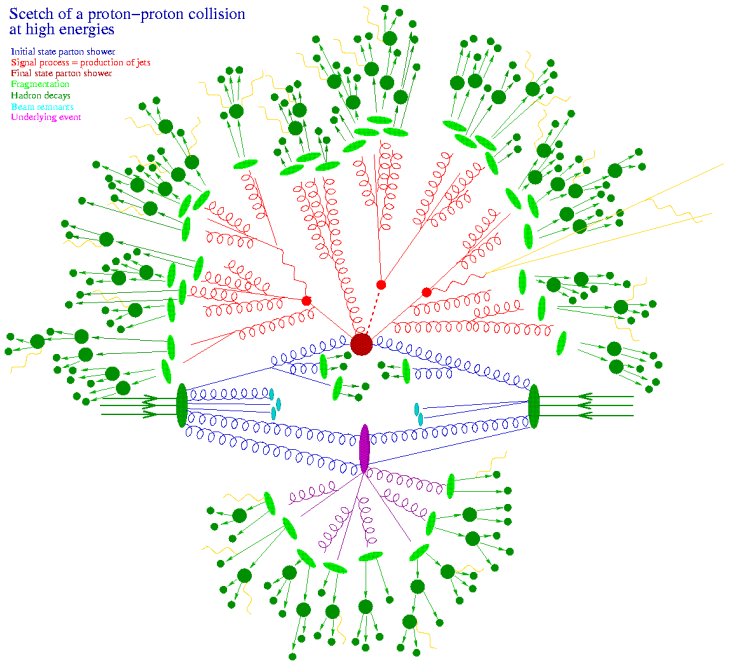

Figure 6.4: Sketch of a proton-proton collision [70].

6.5 Impact of the Overlap Removal on the $t\bar{t}H^0(H^0 \to b\bar{b})$ Analysis

The $t\bar{t}H^0(H^0 \to b\bar{b})$ analysis consists of an initial preselection requirement which is applied to the events to ensure that the fundamental physics objects from the decays of the top quark pair and the Higgs boson are present. Three different analysis techniques are then implemented to reconstruct the top quark pairs and the Higgs boson [5]. The analysis technique used in this study is the cut-based approach. Differences with respect to the baseline analysis [5] are detailed below.

6.5.1 Preselection

For this study, the preselection includes off-line criteria that require the presence of exactly one isolated, identified electron or muon and at least six jets with $p_T >$ 20 GeV. Jets have been reconstructed with a $\Delta R = 0.4$ Anti-k$_\mathrm{T}$ algorithm [50, 51]. No trigger requirements have been applied.

At least four jets have to be identified by a b-tagging algorithm whose discrimi-

nating variable is a weight based on the impact parameters and secondary vertices of tracks in each jet, exploiting the long decay lifetime of b-quarks [56]. Only the four jets with the largest b-tag weights are then treated as b-jets.

Table 6.2 compares the $t\bar{t}X$ cross-sections of the removed events before and after the preselection cuts to the total $t\bar{t}b\bar{b}$ cross-section. We now find the cross-section of the removed events to be about 0.8 times the cross-section of $t\bar{t}b\bar{b}$ events passing the preselection. This is much closer than before and implies that parton showers and matrix elements agree much better at higher transverse momentum. The factor of 0.8 may be consistent with the expectation that the $t\bar{t}b\bar{b}$ cross-section should be slightly higher due to additional diagrams that cannot be reproduced by simply adding extra b-quarks using the parton shower approach.

6.5.2 Cut-based Analysis

The cut-based approach to the $t\bar{t}H^0(H^0 \to b\bar{b})$ analysis starts with the reconstruction of the hadronic and leptonic W bosons. The W candidates are then paired with b-jets to reconstruct the top quark candidates, applying a mass cut on the hadronic W boson and the top quark masses to reduce the considered number of combinations. A χ^2 is defined to evaluate the deviation of the reconstructed top masses from their nominal values. The combination with the smallest χ^2-value is selected. The two remaining b-jets are then assigned to the Higgs boson decay. Figure 6.5 shows the invariant mass of the reconstructed Higgs boson for the signal and all

Process	$t\bar{t}$+0p	$t\bar{t}$+1p	$t\bar{t}$+2p	$t\bar{t}$+3p	$t\bar{t}X$	$t\bar{t}b\bar{b}$
Dataset	109620	109621	109622	109623		109627
$t\bar{t}b\bar{b}$ cross-section (fb) before preselection	144.23	500.05	716.35	549.25	1909.18	661.53
$t\bar{t}b\bar{b}$ cross-section after preselection (fb)	0	0.22	1.98	2.59	4.77	5.92

Table 6.2: Cross-sections of the removed overlap events before and after the preselection for the simulated samples $t\bar{t}X$ and $t\bar{t}b\bar{b}$ (QCD).

backgrounds before and after the overlap removal is applied to the $t\bar{t}X$ sample.

Figure 6.6 shows a comparison of the distribution for the overlapping events from the $t\bar{t}X$ sample with the distribution of $t\bar{t}b\bar{b}$ events in the invariant Higgs mass spectrum. As indicated in Table 6.2, the cross-sections of the two samples are similar. The reasons for this are discussed in the Section 6.6.

The statistical significances have been calculated for two cases: firstly in which the $t\bar{t}X$ sample including the $t\bar{t}b\bar{b}$ events is used instead of the $t\bar{t}b\bar{b}$ QCD sample and secondly in which the overlap from the $t\bar{t}X$ sample has been removed and the $t\bar{t}b\bar{b}$ QCD sample is used to describe the $t\bar{t}b\bar{b}$ events. For the first case, the significance is 1.01σ, whereas for the second case, the significance is 1.03σ.

6.6 Concerns and Further Improvements

A procedure has been developed for removing the fraction of the $t\bar{t}X$ sample that overlaps with the $t\bar{t}b\bar{b}$ QCD sample. It has been shown that the ratio of the cross-sections of the removed overlap and the $t\bar{t}b\bar{b}$ QCD sample is almost 3, reducing to 0.8 after the analysis preselection is applied. The b-quarks in the final state not originating from top decays are introduced via parton showers in the $t\bar{t}X$ sample and matrix elements in the $t\bar{t}b\bar{b}$ (QCD) sample and this needs to be explored further to understand the different cross-sections.

Figures 6.7 and 6.8 show the $p_T(b)$ and $\Delta R(b\bar{b})$ distributions for b-quark pairs in the $t\bar{t}b\bar{b}$ and $t\bar{t}X$ sample before any selection cuts have been applied. They have been plotted for different regions of$\Delta R(b\bar{b})$and $p_T(b)$ respectively. It is observed in Figure 6.7 that while $t\bar{t}X$ dominates the regions up to $\Delta R < 0.7$, the $t\bar{t}b\bar{b}$ dominates the region of high p_T (above 30 GeV) and high ΔR (> 0.7). More generally, Figure 6.8 demonstrates that $t\bar{t}b\bar{b}$ is quite evenly distributed in $\Delta R(b\bar{b})$while $t\bar{t}X$ is peaked towards lower values. This may be consistent with expectations since there are regions of phase space where the $b\bar{b}$ pair is more correctly modelled by the parton shower approach and others where the leading order matrix element approach is expected to be more correct. For parton showering, this is expected to be the low $\Delta R(b\bar{b})$, low $p_T(b)$ region and for the matrix element approach the region of high $\Delta R(b\bar{b})$ and high $p_T(b)$. It is often the case that a region exists where both

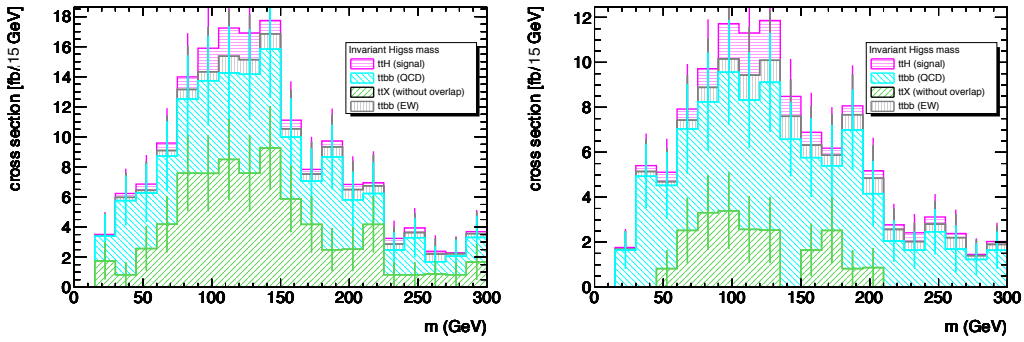

Figure 6.5: Invariant Higgs mass before (left) and after (right) the overlap removal for the tt+X sample.

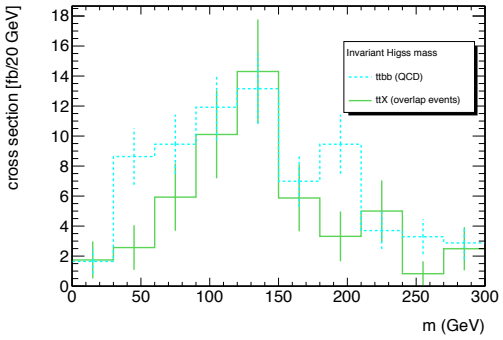

Figure 6.6: Comparison of the invariant Higgs mass distribution of the overlapping events from tt+X sample and the events from the $t\bar{t}b\bar{b}$ sample.

approaches behave similarly although this is not evident here.

The same plots are shown in Figures 6.9 and 6.10 after applying the analysis preselection. Due to the decrease in statistics, it is very difficult to draw conclusions except that it is still possible to see the parton shower $b\bar{b}$ pairs peaking toward lower values in $\Delta R(b\bar{b})$.

It is clear that the b-quark pairs from parton showers and matrix elements in the $t\bar{t}b\bar{b}$ final state exhibit kinematic differences. In fact, the problem of accurately combining parton shower and matrix element results is not restricted to this analysis and has been extensively investigated in many recent publications, such as [71]. It is recommended by the authors that when generating $t\bar{t}$ + jets backgrounds for $t\bar{t}H^0(H^0 \to b\bar{b})$ in future, priority should be given to selecting a Monte Carlo genera-

tor that can most accurately combine the parton shower and matrix element b-quark contributions in a single sample. This would remove the need for an overlap removal and would improve accuracy.

With the background samples considered here, there is no clear way to accurately combine the parton shower and matrix element $t\bar{t}b\bar{b}$ samples. The approach taken will therefore be to apply the overlap removal technique presented in this thesis and use the difference in signal significance given in Section 6.5 to represent the uncertainty. This is $1.03\sigma - 1.01\sigma = 0.02\sigma$, so not significant.

6.7 Conclusion

In this study a way of removing the overlap from irreducible and reducible $t\bar{t}$ + jets background Monte Carlo samples for the semileptonic $t\bar{t}H^0(H^0 \to b\bar{b})$ channel has been presented. Overlapping events in the $t\bar{t}$ + jets sample have been identified as events that contain at least one $b\bar{b}$ pair that does not originate from the underlying event and the procedure of how to remove those events has been described.

It has also been shown that the overlapping events have a relatively large effect on the final invariant Higgs mass plot due the additional $b\bar{b}$ pairs as they can mimic the $b\bar{b}$ pair from the Higgs decay. Therefore applying this overlap removal is very important as otherwise it may lead to an overestimation of the background contribution and underestimation of the significance.

It has been shown that the parton shower and matrix element $t\bar{t}b\bar{b}$ samples behave differently and it is recommended that future $t\bar{t}H^0(H^0 \to b\bar{b})$ analyses use a background generator that combines these components automatically and removes the need for an overlap removal. An uncertainty of 0.02σ is assigned to the signal significance here to account for any effects introduced by the overlap removal.

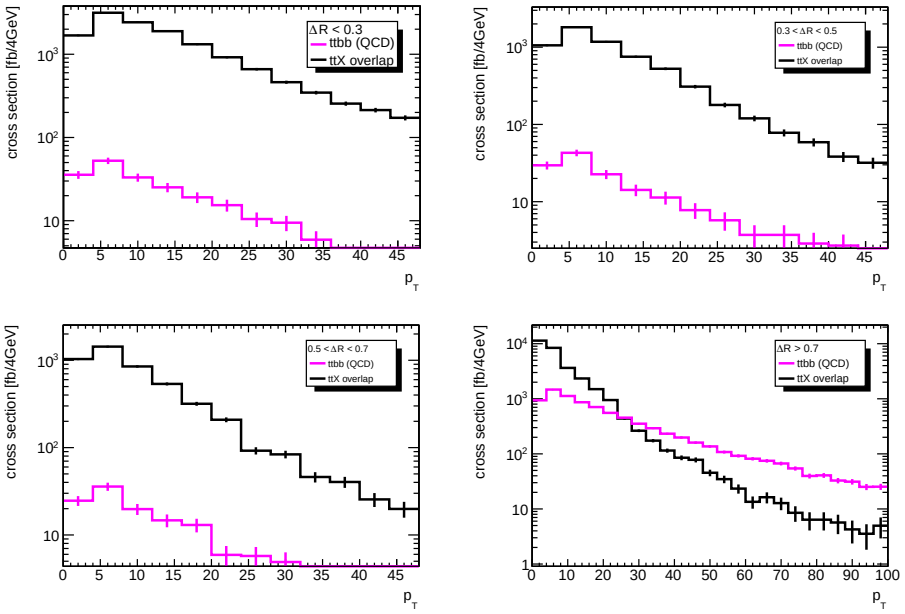

Figure 6.7: Numbers of b quark pairs distributed in $\mathrm{p_T}$ for the different regions of phase space for the $t\bar{t}b\bar{b}$ and $t\bar{t}X$ sample before any analysis cuts have been applied.

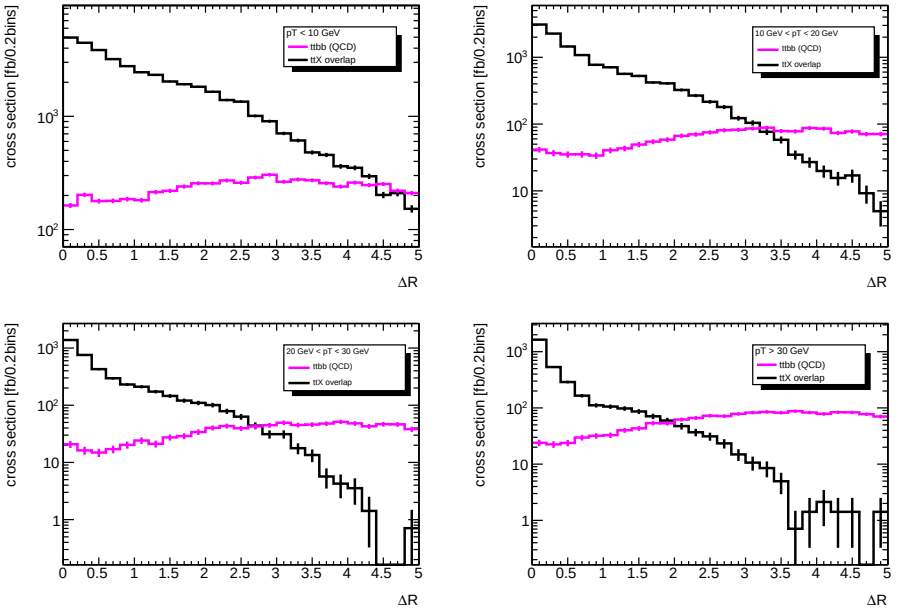

Figure 6.8: Numbers of b quark pairs distributed in $\Delta\mathrm{R}(b\bar{b})$ for the different regions of phase space for the $t\bar{t}b\bar{b}$ and $t\bar{t}X$ sample before any analysis cuts have been applied.

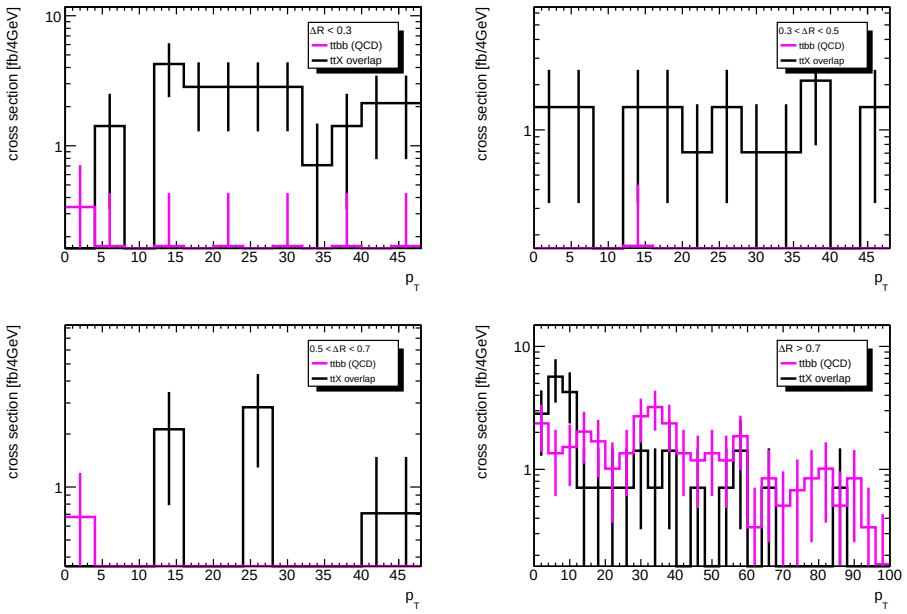

Figure 6.9: Numbers of b quark pairs distributed in $\mathrm{p_T}$ for the different regions of phase space for the $t\bar{t}b\bar{b}$ and $t\bar{t}X$ sample after analysis cuts have been applied.

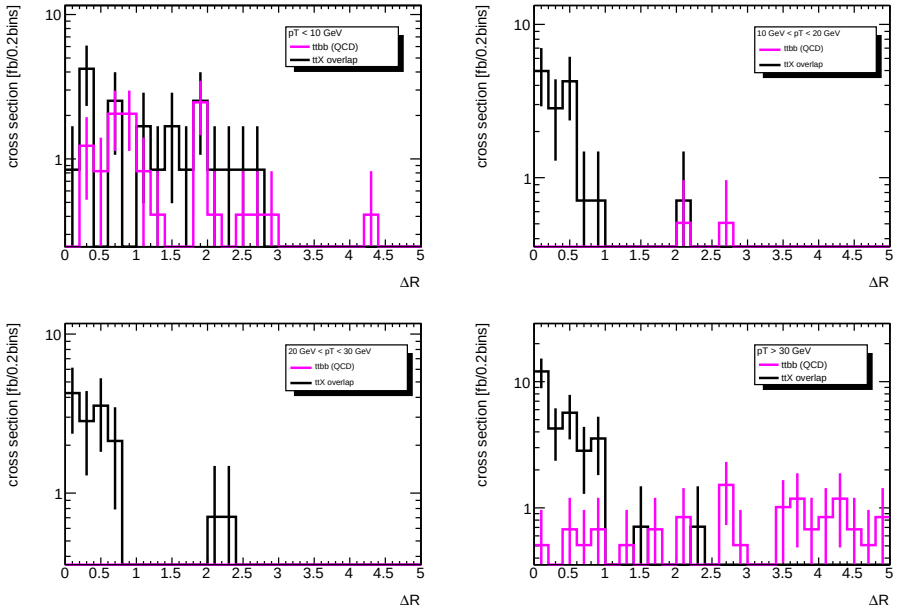

Figure 6.10: Numbers of b quark pairs distributed in $\Delta\mathrm{R}(b\bar{b})$ for the different regions of phase space for the $t\bar{t}b\bar{b}$ and $t\bar{t}X$ sample after analysis cuts have been applied.

Chapter 7

Fat Jets Analysis

7.1 Introduction

The associated production of a top quark pair with a Higgs boson in combination with the Higgs decaying to b-quarks was expected to be one of the leading discovery channels for a light Higgs boson. Reconstructing the $t\bar{t}H^0$ system typically involved the identification of a semileptonically and a hadronically decaying top including four jets, two of which are tagged as b-jets, a lepton and missing energy and additionally two jets tagged as b-jets from the Higgs decay. The main problems are the combinaFtorial background of b-jets and the lack of truly distinctive kinematic feature of the Higgs decay jets.

A recently published paper [3] (which will be referred to as *hadron* or *truth level analysis*) investigated the $t\bar{t}H^0(H^0 \to b\bar{b})$ channel in a boosted regime, in which the Higgs and top quarks are emitted at large transverse momenta. One of the keys to successfully exploiting the boosted $t\bar{t}H^0$ channel lies in the use of jet-finding geared to identifying the characteristic structure of a Higgs boson with high momenta that decays to $b\bar{b}$ pair in a common neighbourhood in angle. This region corresponds to only a small fraction of the total $t\bar{t}H^0$ cross-section, but the signal acceptance is larger, while the backgrounds are significantly reduced. The paper shows how jets from the decay of massive particles and reconstructed with a large R-parameter, can help to indeed extract this channel with a reasonable statistical significance and a much reduced sensitivity on systematics. These jets are called *fat jets*.

Fat jets have been studied in the framework of searches for strongly interacting W bosons [72, 73, 74, 75], supersymmetric particles [76, 77, 78] and heavy resonances decaying to strongly boosted top quarks [79, 80, 81], as well as the WH/ZH production channels with $t\bar{t}H^0$, for which a significance of 3.7σ (considering only statistical errors) using 30 fb^{-1} for a Higgs boson mass of 120 GeV using a realistic ATLAS detector simulation has been found [4, 35].

It is now of great importance to confirm that the Higgs boson signal extraction is indeed possible in such a boosted environment in a detailed study based on a realistic detector simulation. This chapter presents a first detector level study of the fat jets analysis for the $t\bar{t}H^0(H^0 \to b\bar{b})$ channel. The procedure of finding the substructure of a fat jet is described in Section 7.2. The hadron level based analysis for the $t\bar{t}H^0(H^0 \to b\bar{b})$ channel [3] is summarised in Section 7.3. The feasibility of this analysis in the ATLAS detector and the Monte Carlo samples used is discussed in Section 7.4, followed by a comparison of the results in Section 7.5.

7.2 Substructure Finding and Filtering

When a highly boosted particle like a top quark or a Higgs boson decays, it can be reconstructed as a single fat jet containing the decay products. While the identification of a high p_T top quark has been studied elsewhere [54], the reconstruction of a high p_T Higgs boson decaying into a pair of b-quark jets is a more challenging task. Due to the high boost, the two decay products will be increasingly close in ΔR for increasing p_T as shown in Figure 7.1. The ΔR dependency can approximately be expressed in terms of Higgs mass and transverse Higgs momentum:

$$\Delta R(b, \bar{b}) \approx \frac{2 \cdot m_H}{p_{T,H}}. \tag{7.1}$$

This behaviour of the Higgs decay products makes the identification more challenging and requires optimised jet finding and b-tagging for this specific kinematic region.

The procedure of finding the jet substructure used in [3] has been derived from the study presented in [4]. It has been adapted so that the same algorithm can be used for the reconstruction of a boosted top. In the following, the jet substructure finding is explained by the means of the boosted Higgs boson.

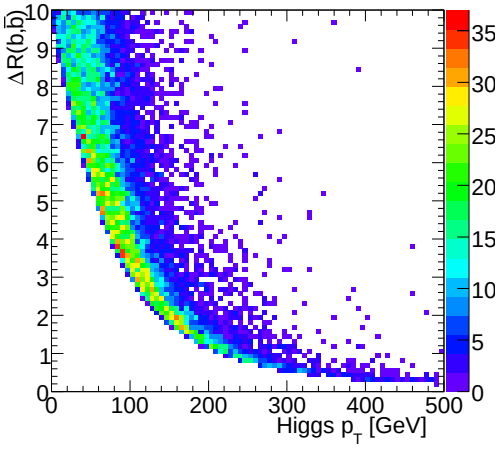

Figure 7.1: Distance in $\Delta R = \sqrt{\Delta\phi^2 + \Delta\eta^2}$ between the two b-quarks from the Higgs boson with a Higgs boson mass of $m_H = 120$ GeV as a function of the Higgs boson transverse momentum. $\Delta\phi$ represents the distance in azimuthal angle, while $\Delta\eta$ is the distance in pseudo-rapidity. The normalisation is arbitrary. Taken from [82].

The jet algorithm used to reconstruct those fat jets is the Cambridge/Aachen algorithm [52, 53], specifically to flexibly adapt to the fact that the decay products ($b\bar{b}$) angular separation varies significantly with the transverse momentum p_T of the particle (Higgs) and decay orientation.

The C/A jet finding algorithm uses an iterative procedure to cluster all pairs of particles. The angular distance $\Delta R_{i,j} = \sqrt{(y_i - y_j)^2 + (\phi_i - \phi_j)^2}$ where y is the rapidity and ϕ the azimuthal angle is calculated between all pairs of objects (particles) i and j, combining the closest pair. The set of distances is updated and the procedure is repeated until all objects are separated by a $\Delta R_{i,j} > R$, where R is a parameter of the algorithm. The algorithm provides a hierarchical structure for the clustering in angles.

The event reconstruction starts with reconstructing C/A jets from topological cell clusters (see Section 4.4.3) using an R parameter of $R = 1.5$. Those jets satisfying p_T >200 GeV and $|y| < 2.5$ are then further decomposed. The recursive decomposition procedure involves two parameters: a mass drop fraction μ which

helps to distinguish between jets from the underlying event or soft QCD emission with a value between 0 and 1; a maximum subjet mass m^{max} as a cut-off parameter which terminates the algorithm (typical value around 30 GeV). The main stages are given below:

1. Undo the last stage of clustering by splitting the jet j into two subjets j_1, j_2, such that $m_{j_1} > m_{j_2}$.

2. In case of a significant mass drop $m_{j_1} > \mu m_j$ $(0 < \mu < 1)$, discard j_2 (j_2 comes from the underlying event or from soft QCD emission) and only keep j_1, otherwise keep both j_1 and j_2.

3. If the mass of the subjet j_i is smaller than a maximum subjet mass $m_{j_i} < m^{max}$ add this jet to list of relevant substructures, otherwise redefine j to be equal to j_i and go back to step 1.

The parameters μ and m^{max} are chosen individually for the top and Higgs tagger.

All two-subjet configurations of the resulting set of relevant substructures are then examined to try to reconstruct a two-body decay candidate, like a W or a Higgs boson. Those two-jet configurations are then re-clustered or *filtered* to reduce contamination from the underlying event. The procedure of re-clustering or filtering of the candidate was first developed for the tagging of the Higgs boson in the WH analysis [4]. However, in the fat jet analysis for $t\bar{t}H^0$ it is also used in the top tagger to filter the W candidate and top candidate. The following description of this procedure is based on the tagging of the Higgs boson.

The angular distance $\Delta R_{b\bar{b}}$ between two subjets j_1, j_2 defines the distance between two b-quarks. A reliable separation and reconstruction of the two b-subjets is needed, so that the direction of the two b-subjets can be considered as a reasonable approximation for the direction of the outgoing b-partons after eventual QCD final state radiation. This is important for obtaining a good b-tagging performance as the two subjets have to be correctly associated to the their charged particle tracks reconstructed in the inner detector.

The effective size of the combined subjets j will be just big enough to contain

the QCD radiation from the Higgs decay. Because of angular ordering [83, 84, 85] this radiation will almost entirely be emitted in the two angular cones of size $R_{b\bar{b}}$ around the b-quarks. Therefore it makes sense to re-cluster or filter the candidate with this radius $R_{b\bar{b}}$, which sets the angular scale of the Higgs decay on a candidate-by-candidate basis.

To filter the candidate, the C/A algorithm is rerun with a finer angular scale $R_{filt} < R_{b\bar{b}}$ on the constituents of the two subjets which make up the candidate. The three hardest objects are taken, one capturing the dominant $O(\alpha_s)$ radiation from the decay, while most of the contamination from the underlying event is eliminated. In this analysis, R_{filt} is chosen to be $R_{filt} = min(0.3, R_{b\bar{b}}/2)$ [18].

7.3 Hadron Level Analysis

The strategy for a $t\bar{t}H^0(H^0 \rightarrow b\bar{b})$ search is based on the high transverse momentum of the leading top quark and the Higgs boson; their spectra are shown in Figure 7.2. To reconstruct the Higgs candidate, several analysis steps have to be taken first. The outline of the analysis is as follows [3]:

- **Event preselection**: Ensuring the presence of fundamental physics objects for the following analysis, requiring two jets and one lepton.

- **Top tagger**: One of the two jets should pass the top tagger. If two jets pass, then the one closer to the top mass is chosen.

- **Higgs tagger**: Run over the remaining jets with $|y_l^{(H)}| < 2.5$ (y being the rapidity), including a double b-tag for the substructure pairings reconstructing the Higgs to reduce the leading $t\bar{t}jj$ topology.

- **Triple b-tag**: To improve the signal-to-background ration S/B and remove the impact of the $t\bar{t}$ + jets background, a third b-tag can be applied in a separate jet analysis.

- **Mass window cut**: A cut on the Higgs mass window of $m_{bb}^{rec} = m_H \pm 10$ GeV is applied.

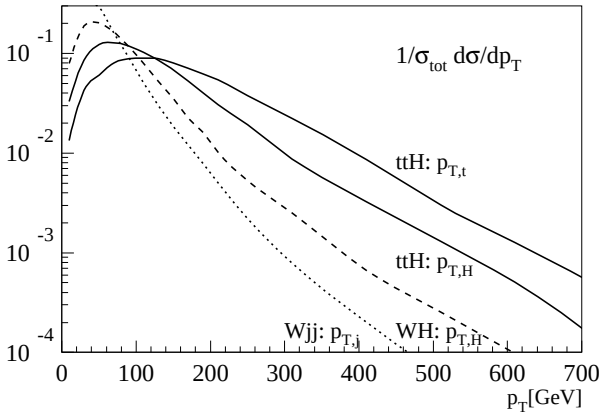

Figure 7.2: Normalised top and Higgs transverse momentum spectra in $t\bar{t}H^0$ production (solid). The p_T^H in W^-H production (dashed and the p_T of the harder jet in W^-jj production with $p_T^j > 20$ GeV (dotted) is also shown. Taken from [3].

7.3.1 Simulated Signal and Background Samples

For the signal sample, associated top and Higgs production with one hadronic and one leptonic top decay have been generated. To account for higher-order effects, a k-factor has been applied to the the signal sample, normalising it to the next-to-leading (NLO) order prediction of 702 fb for a Higgs mass of $m_H = 120$ GeV. The main backgrounds considered in this analysis are:

- irreducible QCD background $pp \to t\bar{t}b\bar{b}$
- irreducible Z production background $pp \to t\bar{t}Z$
- jets misstagged as b-quarks $pp \to t\bar{t}$ + jets

The NLO cross-section of the irreducible $t\bar{t}b\bar{b}$ background is 2.6 pb after the acceptance cuts of $|y_b| < 2.5$, $p_{T,b}$ >20 GeV and $R_{bb} > 0.8$. The $t\bar{t}Z$ background has a NLO cross-section of 1.1 pb. For the $t\bar{t}$ plus jets production no k-factor is applied (see [3] for more details).

All hard processes were generated using MadEvent [86], shower and hadronisation via HERWIG++ [87] (without $g \to b\bar{b}$ splitting) and analysed with FastJet [88].

7.3.2 Lepton and Jets Preselection

The event preselection ensures the presence of fundamental physics objects which are necessary to carry out the following analysis. At least two hard jets satisfying p_T >200 GeV and $|y^{\text{Higgs}}| < 2.5$ (for the jet to be tagged as Higgs), $|y^{\text{top}}| < 4$ (for the jet to be tagged as the top) and a lepton with $p_{T,\,\text{lepton}}$ >15 GeV and $|y_{\text{lepton}}| < 2.5$ are required. For lepton identification and isolation a 80% efficiency was used. The maximum Higgs jet rapidity y^{Higgs} is limited so that the tagging of the b-content is possible.

7.3.3 Top Tagger

For a top candidate with typically a jet mass above 200 GeV, a complex hard substructure inside the fat jet is assumed. To analyse the jet's substructure, the procedure in Section 7.2 is applied. The value for the mass drop fraction is chosen to be $\mu = 0.8$ and a value of $m^{max} < 30$ GeV is chosen for the mass cut-off [3]. The choice of the cuts is motivated by the default values from the VH analysis [4] which have been shifted to accommodate the generically larger jet multiplicity in the $t\bar{t}H^0$ channel.

First, all two-subjet configurations are then examined to reconstruct a W boson. Those two-jet configurations are then filtered (see Section 7.2) and the W candidate is formed from the three hardest subjets, assuming two jets to be from the decay of the W boson and the third jet to be from QCD radiation. The mass of the substructure pair is required to be in the range $m_W^{rec} = 65 - 95$ GeV.

The top candidate is reconstructed: to tag the top quark, a third subjet is added to the two-subjet configuration which was used to reconstruct the W candidate. These three subjets are now filtered and the five hardest objects are taken to form the top candidate. Three of the five jets represent the decay products of the top quark ($t \to Wb$, $W \to jj$) and the remaining two jets take the QCD radiation into account. Their mass is required to be $m_t^{rec} = 150 - 200$ GeV.

Additionally the W helicity angle θ with respect to the top candidate should satisfy $\cos\theta < 0.7$ [54]. The helicity angle is a standard observable in top decays,

used to determine the Lorentz structure of the top-W coupling. It is defined as the angle, measured in the rest frame of the reconstructed W, between the reconstructed top quark's flight direction and one of the W decay products. If more than one top tag was found in the event, the tag with the smaller mass difference $|m_t^{rec} - m_t^{pole}| + |m_W^{rec} - m_W^{pole}|$ is chosen. Figure 7.3 shows the reconstructed W and top quark mass distributions for signal and background samples.

7.3.4 Higgs Tagger

The Higgs tagger runs on the remaining jets which have not been tagged as top quarks, using the same decomposition procedure with a mass cut off $m_{j_i} < 40$ GeV and a mass drop fraction of $\mu = 0.9$. All pairs of subjets are then ordered by the modified Jade distance [76, 77, 78]:

$$J = p_{T,1} p_{T,2} (\Delta R_{12})^4 \tag{7.2}$$

similar to the mass of the hard splitting but shifted towards larger jet separation. The three pairs with the highest Jade distance are filtered and considered as Higgs candidates. They have to explicitly pass a cut $p_{T,H} \gtrsim 200$ GeV.

At this stage, flavour tags are included to control the $t\bar{t}$ +jets and W + jets backgrounds. Two bottom tags for the substructure pairings which form the Higgs candidate are required in order to reduce the $t\bar{t}$ + jets topology. In the hadron level analysis, a 70% b-tagging efficiency with a 1% mis-tagging probability is assumed.

7.3.5 Triple b-tag

With the top tagger, the hadronically decaying top from the $t\bar{t}$ system has been identified. To improve the signal-to-background ratio S/B and remove the impact of the $t\bar{t}$ + jets background, it is now attempted to find the b quark from the semileptonically decaying top by applying a third b-tag to the event.

Firstly, all constituents from the Higgs and top candidates are removed from the event before the remaining particles are clustered using the C/A algorithm with $R = 0.6$. These jets have pass the acceptance cuts of $p_T > 30$ GeV and $|\eta| < 2.5$ and

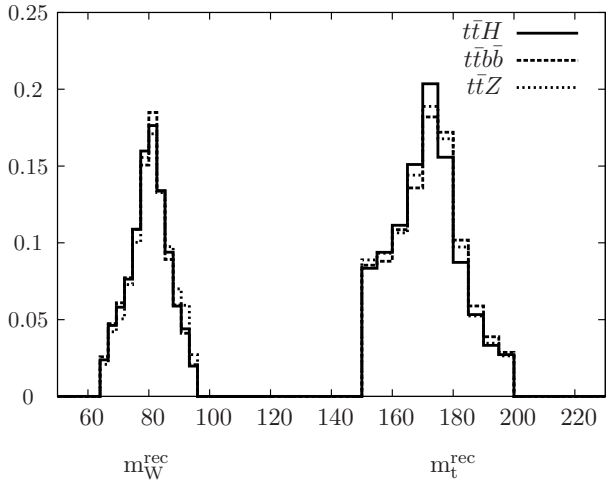

Figure 7.3: Individually normalised m_W^{rec} and m_t^{rec} distributions for signal and background (with underlying event). Taken from [3].

are then b-tagged assuming a b-tagging efficiency of 60% and purity of 2%. To ensure that the b-tagged does not originate from the hadronically decaying top or the Higgs boson, a minimum distance of $\Delta R_{b,j} > 0.4$ between the subjets from the Higgs and top candidate is required. Figure 7.4 shows the reconstructed Higgs mass for signal ($m_H = 120$ GeV) and backgrounds with (lower) and without (upper) underlying event after the third b-tag has been applied.

7.3.6 Results

The results for the double b-tag analysis (Higgs tag including a double b-tag and $m_H^{rec} = 110 - 130$ GeV) and the triple b-tag analysis for an integrated luminosity of 100 fb^{-1} and a generated Higgs mass of $m_H = 120$ GeV can be found in Table 7.1.

stage of analysis	S	B	S/B	$S/\sqrt{B}$
double b-tag	100	380	1/3.2	6.2
triple b-tag	48	115	1/2.4	4.5 (5.1)

Table 7.1: Results for the double and triple b-tag analysis for an integrated luminosity of 100 fb^{-1}. The number in parenthesis is without underlying event. Taken from [3].

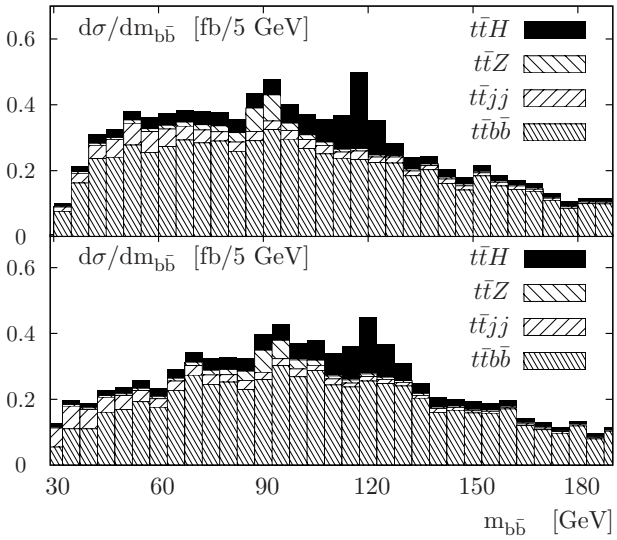

Figure 7.4: Reconstructed b-pair mass for signal ($m_H = 120$ GeV) and backgrounds with (lower) and without (upper) underlying event after the third b-tag has been applied. Taken from [3].

7.4 Detector Level Analysis

The hadron level analysis has indicated that at high transverse momenta the $t\bar{t}H^0$ channel can be recovered as a promising search channel for the Standard Model Higgs boson discovery around 120 GeV using state-of-the-art jet reconstruction and decomposition techniques.

This section presents an investigation of the feasibility of this analysis using a realistic simulation of the ATLAS detector. The selection applied has been chosen to be close to that in the hadron level analysis to be able to directly compare the results of the hadron and detector level analysis (except for b-tagging and applied mass windows).

In the following, *truth matching* is applied where applicable, meaning that a reconstructed particle is matched to a MC truth particle of a certain kind, i.e. the lepton from a semileptonic top decay. Hereby the distance in ΔR is calculated and where not stated otherwise, a match is considered a *correctly* reconstructed candidate when $\Delta R < 0.15$. The ΔR distribution is not a sharp distribution due to the process of hadronisation, therefore this value has been chosen as a compromise

between efficiency and purity.

7.4.1 Event Samples and Detector Simulation

All event samples have been generated at leading order with a centre-of-mass energy of $\sqrt{s} = 10$ TeV and a top quark mass of $m_{top} = 172.5$ GeV. Although $\sqrt{s} = 10$ TeV is not the nominal centre-of-mass energy, it is the energy at which it was originally expected to collect a first sizeable amount of data. A brief study towards the comparability of the results obtained with 10 TeV simulated data to 14 TeV data is given in Section 7.4.1.

Signal and Background Samples

The $t\bar{t}H^0(H^0 \rightarrow b\bar{b})$ sample used in this analysis is the same as in the cut-based analysis and described in detail in Section 5.2 and Table 5.1.

The main background processes considered are the same as those in the cut-based analysis and the hadron level analysis:

- irreducible electroweak background $pp \rightarrow t\bar{t}b\bar{b}$
- irreducible QCD background $pp \rightarrow t\bar{t}b\bar{b}$
- jets misstagged as b-quarks $t\bar{t}$ + jets

The $t\bar{t}b\bar{b}$ (QCD and EW) and $t\bar{t}X$ samples were generated in the same way as those described in detail in Section 5.2 with the only difference that the TtbarPlusJetsFilter, which applies multiplicity, p_T and η requirements to 0.4 cone sized jets (see Section 5.2 for details), has not been applied. Tables 7.2 and 7.3 summarise the details of the background samples including the final cross-sections.

Centre-of-mass Energy Considerations

As already mentioned in Chapter 5.2.2, at the time of generating the MC samples for this thesis, the LHC run plan had foreseen a longer run with $\sqrt{s} = 10$ TeV. Therefore the MC samples used in this thesis were generated at $\sqrt{s} = 10$ TeV.

For this analysis it is of interest to compare the results with the result from the $\sqrt{s} = 14$ TeV hadron level analysis but also to the $\sqrt{s} = 10$ TeV cut-based

Dataset	109627	109626
Process	$t\bar{t}b\bar{b}$(QCD)	$t\bar{t}b\bar{b}$(EW)
Production mode	gg, $q\bar{q}$	gg
$t\bar{t}$ decays included	All	All
ME generator	ALPGEN 2.13	AcerMC
ME cross-section (fb)	3703.5	195.4
Q scale ($m_T^2 = m^2 + p_T^2$)	232.5 GeV	$\hat{s}$
PDF set used	CTEQ6L1	CTEQ6L
Cuts	$\lvert\eta_{\text{light jet}}\rvert < 6$	-
ME cross-section at Q=232.5 GeV (fb)	3703.5	315.2
Supervising generator	HERWIG	Pythia
Enforced decays	-	Semileptonic e, μ
Cross-section before filter (fb)	3703.5	90.78[a]
Detector simulation	ATLFAST II	
Semileptonic e,μ selection efficiency	0.2492	1.0
Final cross-section (fb)	1270.13	90.78

Table 7.2: Summary of the simulated $t\bar{t}b\bar{b}$ background samples contributing as irreducible backgrounds.

[a]by-hand multiplication of ME cross-section with semileptonic (e, μ) BR based on current PDG values: 28.8%

result. A simple preselection has been applied to $t\bar{t}H^0$ events, generated with Pythia 6.4 [44] and with $\sqrt{s} = 7$ TeV, 10 TeV and 14 TeV. The preselection cuts are applied at hadron level and jets have been reconstructed using the cone jet algorithm using an R-parameter of 1.5. An event passes the preselection if it contains exactly one lepton with $p_T > 15$ GeV and $|\eta| < 2.5$ and at least two jets with $p_T > 200$ GeV and $|\eta| < 4.0$.

The cross-sections before and after preselection as well as the efficiencies for the lepton and jet preselection are summarised in Table 7.4. The resulting cross-section

Dataset	109620	109621	109622	109623
Process ($t\bar{t}$ + X partons)	$t\bar{t}+0$	$t\bar{t}+1$	$t\bar{t}+2$	$t\bar{t}+3$
Production mode	gg,$q\bar{q}$			
$t\bar{t}$ decays included	Semileptonic (e,μ,τ)			
ME generator	ALPGEN 2.13			
ME cross-section (fb)	95360	121220	91370	50480
Q scale ($m_T^2 = m^2 + p_T^2$)	$\sum m_T^2$ over all (final state partons)			
PDF set used	CTEQ6L1			
Cuts	$p_T^{\text{light jet}} > 20$ GeV, $\lvert\eta_{\text{light jet}}\rvert < 6$ ΔR(light jet, light jet) > 0.7			
ME cross-section at Q=232.5 GeV (fb)	105196	139197	108649	62880
MLM matching efficiency	0.39	0.29	0.22	0.16
Supervising generator	HERWIG			
Cross-section before filter (fb)	41363.1	39893.9	23479.0	10274.6
Detector simulation	ATLFAST II			
Semileptonic e,μ selection efficiency	0.5394	0.5910	0.6417	0.6607
Cross-section after filter (fb)	27771.74	26725.8	15580.81	9557.76
Cross-section after overlap removal (fb)	27105.23	25630.04	14677.13	8754.9

Table 7.3: Summary of the simulated $t\bar{t}X$ background samples, simulated in four sub-samples containing between zero and three additional light partons. The cross-sections after removing the overlap (see text and Chapter 6 for details) are also given.

scaling factor between the 10 TeV and 14 TeV sample is 2.47 and 3.01 between the 7 TeV and 10 TeV sample. This means that the obtained significances for this analysis have to be scaled by a factor of $\sqrt{2.47} = 1.57$ to compare them to the significances obtained in the 14 TeV hadron level analysis.

$\sqrt{s}$	cross-section	preselection efficiency		cross-section
	before preselection	lepton	jet	after preselection
7 TeV	8.12 fb	65.62%	41.54%	2.21 fb
10 TeV	21.98 fb	63.91%	47.48%	6.66fb
14 TeV	51.96 fb	62.92%	50.29%	16.44 fb

Table 7.4: Cross-sections before and after the preselection carried out at parton level for simulated $t\bar{t}H^0$ events at centre-of-mass energies of $\sqrt{s} = 7$ TeV, 10 TeV, 14 TeV and the selection efficiencies of the lepton and fat jet preselection. The resulting cross-section scaling factor between the 10 TeV and 14 TeV sample is 2.47 and 3.01 between the 7 TeV and 10 TeV sample.

7.4.2 Preselection

To ensure that the required physics objects are present in the event, a preselection as a first step of the analysis is applied. It requires at least two jets, reconstructed using the Cambridge/Aachen (C/A) jet algorithm with $R = 1.5$ and one isolated lepton.

Lepton Preselection

Leptons (electrons and muons) have to pass the kinematic and geometrical cuts on the transverse momentum $p_T > 15$ GeV and pseudorapidity $|\eta| < 2.5$ as well as some electron- and muon-specific cuts to be accepted as a candidate lepton coming from the semileptonic decay of the $t\bar{t}$ system. The lepton preselection is the same as applied in the cut-based analysis (Chapter 5) and more details can be found in Section 5.4.1.

The lepton preselection efficiency in the signal is 61.3%, the efficiencies for all samples can be found in Table 7.5.

Jet Preselection

The event passes the preselection if at least two jets satisfy p_T >200 GeV and $|\eta^{\text{Higgs}}| < 2.5$, $|\eta^{\text{top}}| < 4$. The jet preselection efficiency in the signal is 25.7%; efficiencies for all samples can be found in Table 7.5 .

Step of analysis	$t\bar{t}H^0$	$t\bar{t}b\bar{b}$ EW	$t\bar{t}b\bar{b}$ QCD
Lepton preselection	61.3% (61.3%)	61.1% (61.1%)	60.4% (60.4%)
Jet preselection	25.7% (15.8%)	19.2% (11.7%)	12.0% (7.3%)
Top tagging	57.5% (9.1%)	50.8% (6.0%)	48.9% (3.6%)
Higgs tagging	12.7% (1.1%)	6.6% (0.4%)	8.1% (0.3%)
Triple b-tag	39.1% (0.5%)	43.0% (0.2%)	30.8% (0.1%)

Step of analysis	$t\bar{t}$+0p	$t\bar{t}$+1p	$t\bar{t}$+2p	$t\bar{t}$+ >3p
Lepton preselection	64.2% (64.2%)	62.3% (62.3%)	60.0% (60.0%)	56.8% (56.8%)
Jet preselection	2.7% (1.7%)	6.7% (4.2%)	13.3% (8.0%)	25.9% (14.7%)
Top tagging	41.1% (0.7%)	43.3% (1.8%)	47.2% (3.8%)	53.8% (7.9%)
Higgs tagging	0.6% (0.0004%)	0.9% (0.02%)	1.2% (0.05%)	1.6% (0.1%)
Triple b-tag	0% (0%)	5.6% (0.001%)	6.6% (0.003%)	13.3% (0.02%)

Table 7.5: Efficiencies of each step of the analysis for the signal and $t\bar{t}b\bar{b}$ (top) and the $t\bar{t}X$ samples (bottom). The efficiencies are calculated on a tool-by-tool basis and as overall efficiencies (in brackets).

7.4.3 Trigger Requirements

The presence of one high-p_T lepton, together with missing transverse momentum, is a distinct signature of the W boson production. These leptons can generally be used to trigger on W production with high efficiency. The trigger menu considered here

is the the menu which was foreseen for a luminosity of 10^{31} cm^{-2}s^{-1}. It contains various relevant lepton trigger signatures but also various jet and missing energy signatures.

The efficiencies for the three trigger levels have been studied in detail in Section 5.5. A combination of the electron trigger *e20_loose* and the muon trigger *mu10* has been chosen to select semileptonic $t\bar{t}H^0$ events. The efficiencies for the logical OR combination of these lepton trigger signatures are given in Table 5.9. The trigger efficiency at EF level is approximately 82.0% for those semileptonic $t\bar{t}H^0$ events which would otherwise pass the offline analysis. The efficiencies have been calculated after the preselection of the cut-based analysis described in Chapter 5 but it is not expected that the difference in the jet preselection between the cut-based and the fat jet analysis interfere with the trigger efficiencies. The trigger efficiencies are not included in the efficiency calculation for this analysis.

7.4.4 Top Tagger

To tag the preselected jets as top candidates, their substructure is considered following the recursive procedure described in Section 7.2. The mass drop fraction is chosen to be $\mu = 0.8$ and the maximum subjet mass to be $m_{j_i} < 30$ GeV.

The first step is to reconstruct the W candidate by forming all possible two-subjet combinations. To reduce the contamination from the underlying event, the subjet combination is filtered (see Section 7.2) and the W candidate is reconstructed from three highest p_T filtered subjets.

Figure 7.5 (left) shows the mass distribution of all reconstructed W candidates and those which could be matched to a W boson in the MC truth in the signal sample, Figure 7.5 (right) shows the truth matched W bosons to which a Gaussian has been fitted to. The mean W mass is found to be $m_W = 78.8$ GeV which, given the error of ± 0.4 GeV, is not in agreement with the nominal W mass of 80.4 GeV. This is probably due to the difference in jet energy scale for which the subjets have not been corrected for. W candidates within a mass window of ± 25 GeV around the nominal W mass are kept to then further reconstruct the top candidates. This is a difference to the hadron level analysis where a mass window of only $m_W = 80$

$\pm$ 15 GeV was chosen in order to account for experimental resolution effects.

The top candidate is reconstructed by adding a third subjet to the two original, non-filtered subjets which form the W candidate. These three subjets are then filtered and the five highest p_T filtered subjets form the top candidate.

For each top candidate, the W helicity angle θ (see Section 7.3.3) with respect to the top candidate is calculated and has to satisfy $\cos\theta < 0.7$. For top jets, the distribution is expected to be basically flat: since the W boson decays on-shell, its decay products are almost isotropically distributed in the W boson rest frame. In contrast, for light quark or gluon jets, the distribution diverges (at the parton level) as $1/(1-\cos\theta)$. This corresponds to a soft singularity in the QCD matrix elements for emitting an additional parton. Example distributions are shown in Figure 7.6 (left). Figure 7.6 (right) shows the helicity angle distribution for top candidates and candidates matched to truth for the signal sample after the top mass window cut has been applied.

Jets with very high transverse momentum ($p_T > 1000$ GeV) have a broader mass distribution than lower p_T jets due to increased radiation from QCD. Therefore, the mass window cuts will have to be adjusted depending on the p_T of the jet. Ref. [54] suggests to choose the mass cuts on the top and W to $p_T/20 + 155$ GeV and $p_T/40 + 70$ GeV, respectively. Figure 7.7 shows the p_T distribution of the top candidates after the helicity cut but before the mass window cut has been applied. It can be seen that most top candidate have a $p_T < 1000$ GeV, therefore the p_T dependent mass window cut has not been used in this analysis.

Figure 7.8 (left) shows all reconstructed and truth matched top candidates after applying the selection cuts with the exception of the top mass window cut, Figure 7.8 (right) shows a Gaussian fitted to the truth matched top candidate mass distribution. The shoulder at lower masses in this distribution is due to candidates which could be matched to a truth top in ΔR space but where the subjets which form the candidate are not the correct ones, i.e. not all decay products are used and instead subjets

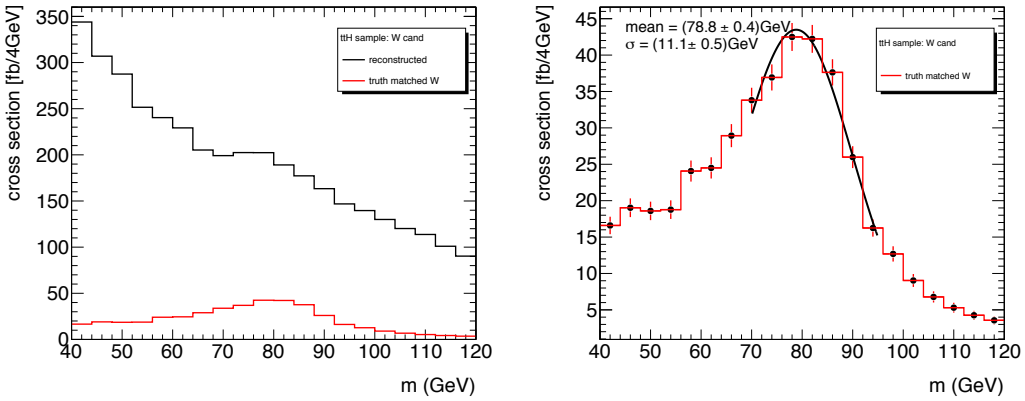

Figure 7.5: Left: Mass distribution of all reconstructed W candidates and the candidates which could be matched a W boson in the MC truth in signal sample. Right: Mass distribution of truth matched W candidates to which a Gaussian has been fitted. All distributions are normalised to 100 fb^{-1}.

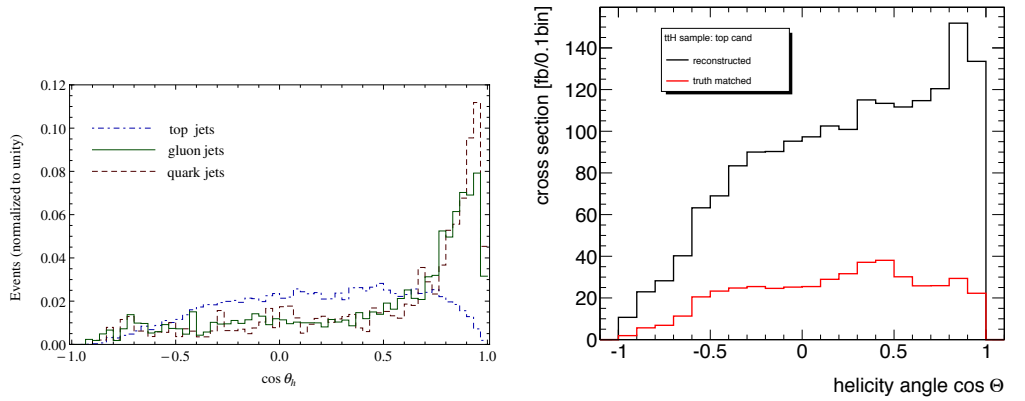

Figure 7.6: Left: Helicity angle distribution for top jets, gluon jets and light-quark jets for $p_T > 700$ GeV, taken from Ref. [54]. The distributions are normalised to unit area. Right: Helicity distribution for the signal sample of all reconstructed top candidates and for all candidates which have been matched to a truth candidate after the top mass window cut has been applied. Distributions are normalised to 100 fb^{-1}.

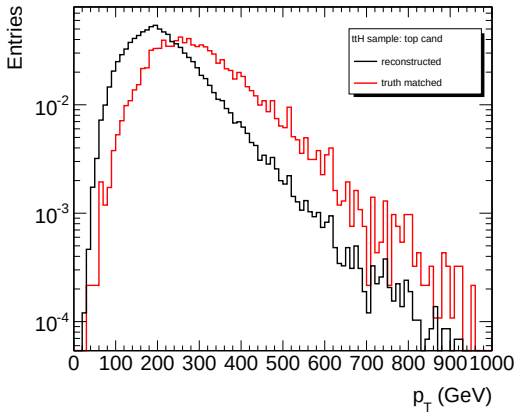

Figure 7.7: Transverse momentum distribution for all reconstructed top candidates after the helicity cut, before the mass window cut has been applied. Distributions are normalised to unit area.

from the underlying event or soft QCD radiation is pulled in. Ideally, to avoid the matching of incorrectly reconstructed candidates to truth particles in ΔR space, the subjets of the massive jet should be matched to the truth partons individually. However, this becomes an extremely challenging task at high energies as the partons which make up the jet are very close together. The Gaussian fit has a mean value of 159.6 ± 1.2 GeV and a width of 22.3 GeV. One of the reasons for the low mean mass value could be the incorrectly matched candidates mentioned above, causing the distribution to shift towards lower values. Another reason could be the use of subjets which have not been corrected for physics effects, i.e. energy loss due to out-of-cone effects (see Section 5.6.2 for details). Therefore, top candidates are required to be within a mass window of $m_t = (160 \pm 25)$ GeV.

It is possible that more than one hadronic top candidate is found in the event. Either more than one top candidate per jet due to the various subjet combinations has been found or more than one preselected fat jet has been tagged as a top candidate. If more than one top candidate has been found, the candidate which minimises the mass difference $|m_t^{rec} - m_t| + |m_W^{rec} - m_W|$ is chosen, with $m_t = 160$ GeV and $m_W = 80.4$ GeV for consistency with the W reconstruction described above. This mass difference is shown in Figure 7.9 for the signal sample. The distribution peaks

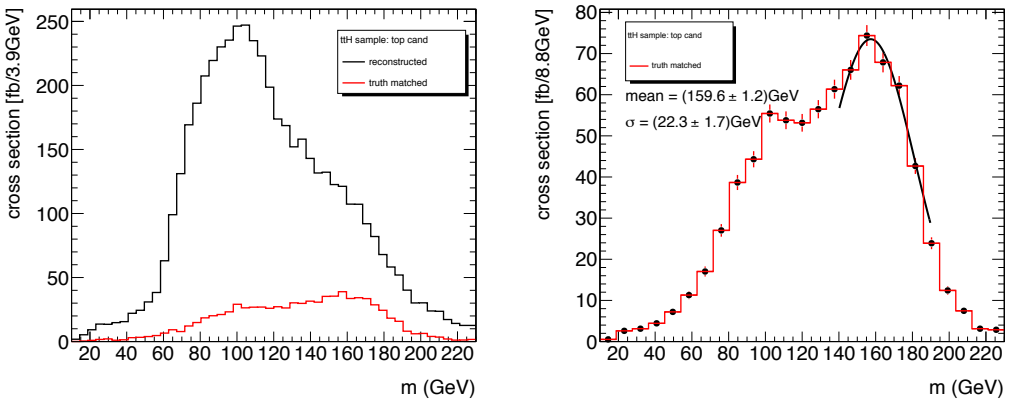

Figure 7.8: Left: Mass distribution of all reconstructed and truth matched top candidates in signal sample. Right: Gaussian fitted to the mass distribution of truth matched top candidates. All distributions are normalised to 100 fb^{-1}.

at around 25 GeV due to the size of the mass windows chosen to be ±25 GeV around the W and top masses. Optimising the W and top reconstruction could probably help to shift the peak towards smaller masses, implying a better mass resolution of the the reconstructed candidates.

The mass distribution for the best W-top combination is shown in Figure 7.10 which compares well with the distribution obtained in the hadron level analysis (Figure 7.3). The resulting top tagging efficiency in the signal is 57.5%. The efficiencies for all samples can be found in Table 7.5.

7.4.5 Higgs Identification

The remaining preselected fat jets within $\eta < 2.5$ which have not been tagged as a top jet are now recursively decomposed as described in Section 7.2 with a maximum subjet mass of $m_{j_i} < 40$ GeV and a mass drop fraction of $\mu = 0.9$. For all two-subjet combinations the modified Jade distance is calculated (see Eq. 7.2) and the filtering procedure is applied to the three pairings with the highest Jade distance. A cut of $p_T > 200$ GeV is re-applied to the filtered four-momentum computed from the three highest p_T filtered subjets which form the Higgs candidate. Figure 7.11 shows the p_T, η, invariant mass and Jade distance distributions for the Higgs candidates at this step of the analysis.

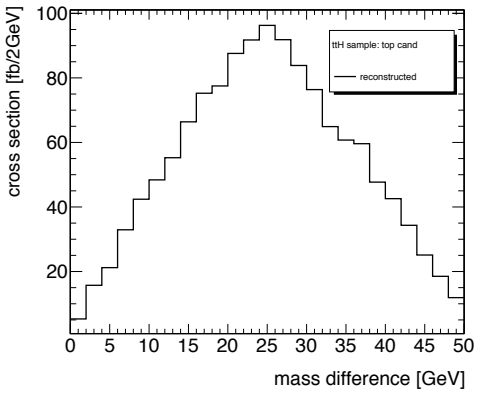

Figure 7.9: Mass difference for the signal sample for all reconstructed W-top combinations.

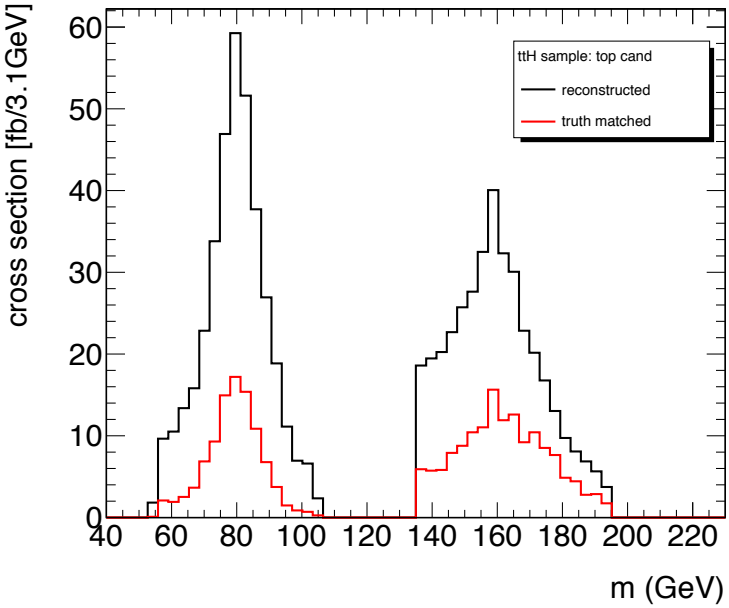

Figure 7.10: Mass distribution for the best W-top combination for the signal sample for reconstructed and truth matched combinations. Distributions are normalised to 100 fb^{-1}.

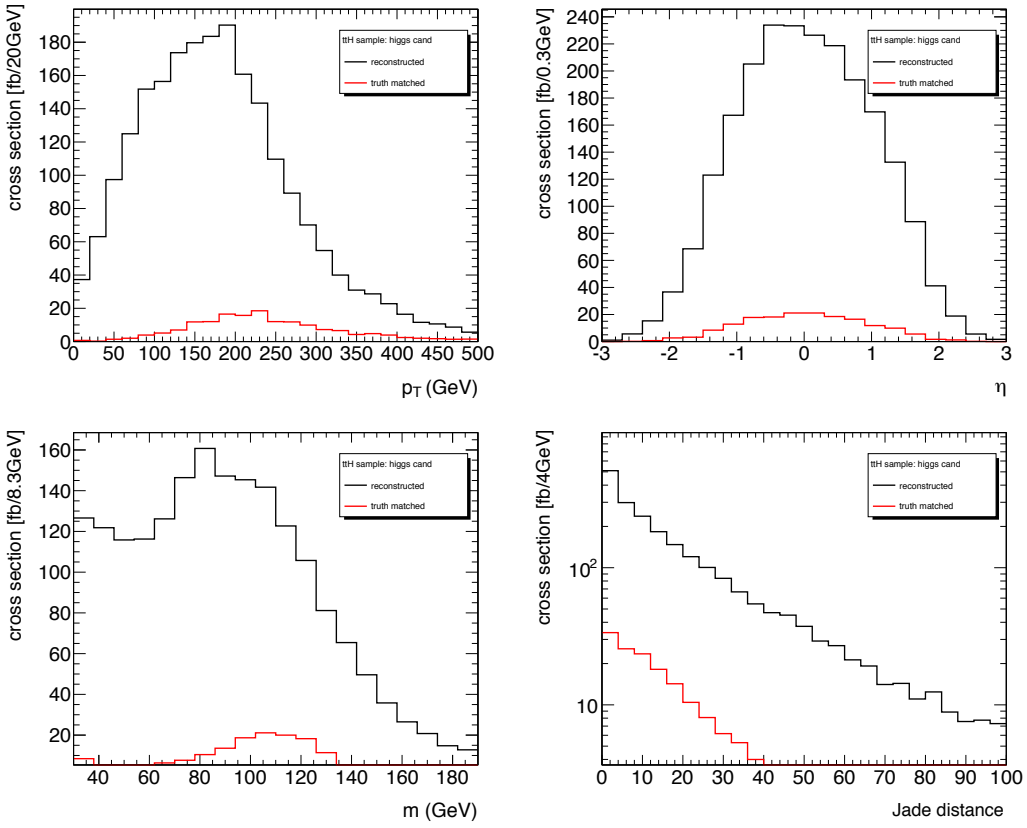

Figure 7.11: Transverse momentum p_T, pseudorapidity η, invariant mass m and Jade distance for the up to three in Jade distance leading Higgs candidates for the signal sample. At this point, b-tagging has not been applied. The distributions for all reconstructed and truth matched are normalised to 100 fb^{-1}.

As a next step, the two highest p_T subjets out of the three which form the Higgs candidate, are required to be tagged as b-jets. The b-tagging weight distribution, b-tagging efficiency versus weight cut, light jet rejection and c-jet rejection versus b-tagging efficiency for the JetFitter-based tagger (JetFitterCOMBNN) and the ATLAS default combined tagger (COMB) (see Chapter 5.4.2) are shown in Figures 7.12 and 7.13.

The b-tagging algorithm chosen for this analysis is JetFitterCOMBNN, an algorithm which combines impact parameter information with the explicit determination of an inclusive secondary vertex. This algorithms has been used and optimised for the environment of boosted Higgs decays in a similar study [35]. Given the differ-

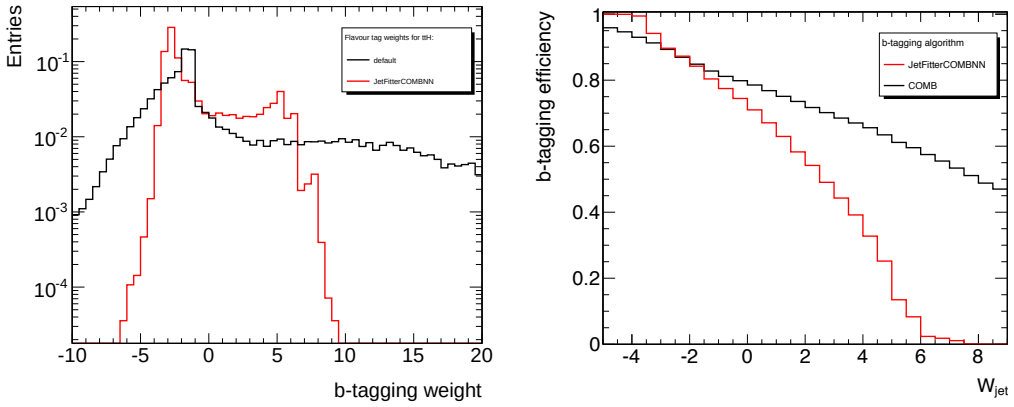

Figure 7.12: Left: Distribution of the weight of the JetFitterCOMBNN and COMB b-tagging algorithm for the signal sample. Right: b-tagging efficiency versus b-tagging weight for the considered b-taggers.

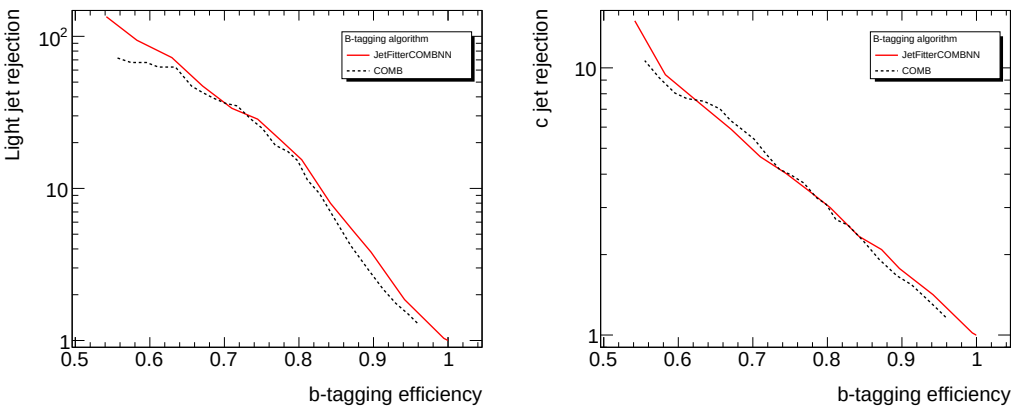

Figure 7.13: Light jet (left) and c-jet (right) rejection versus b-tagging efficiency for the JetFitterCOMBNN and COMB b-tagging algorithms for the signal sample.

ent weight cuts for the COMB and JetFitterCOMBNN tagger (COMB: $W_{jet} > 4$; JetFitterCOMBNN: $W_{jet} > 1$) it can be seen from Figures 7.12 and 7.13 that both taggers have a similar performance in terms of light and c-jet rejection at a given b-tagging efficiency. Jets are required to have a weight $W_{jet} > 1$ to be tagged as b-jets. This corresponds to a b-tagging efficiency of 63.0%, a light jet rejection of 72.5 and a c-jet rejection of 7.3. Figure 7.14 shows the p_T, η and Jade distance distributions for the Higgs candidates with at least two b-tagged subjets.

If more than one Higgs candidate is found for an event with a top-tagged jet,

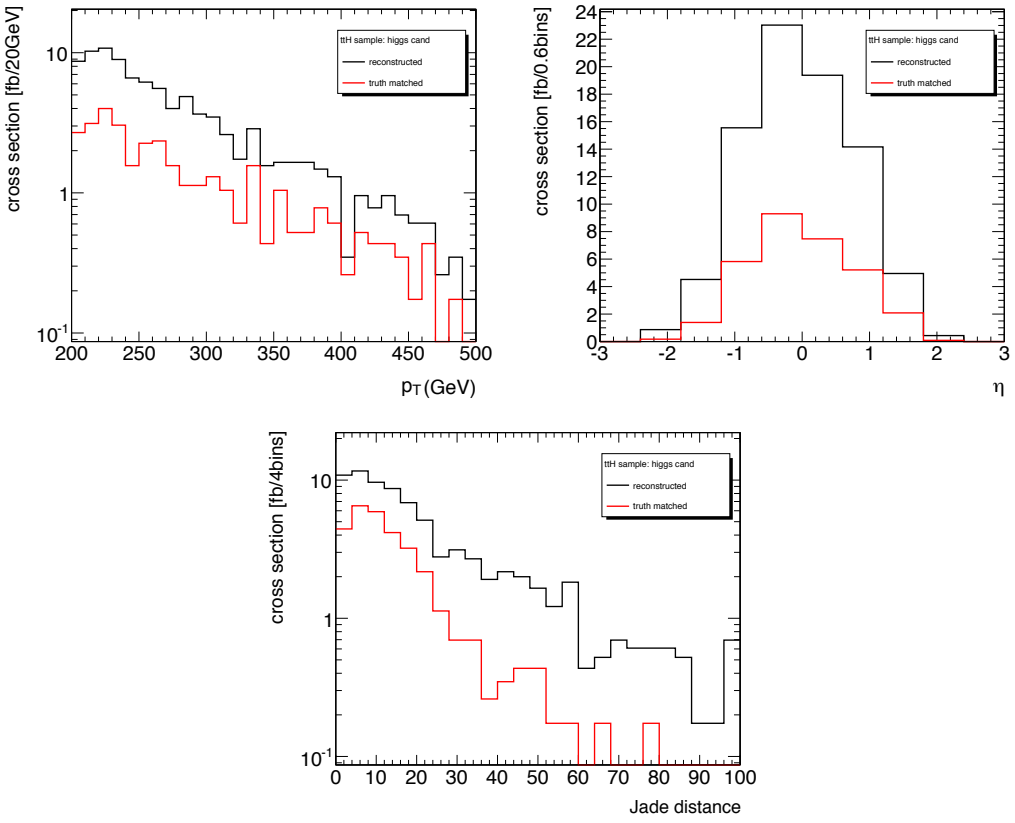

Figure 7.14: Transverse momentum p_T, pseudorapidity η and Jade distance for the up to three in Jade distance leading Higgs candidates for the signal sample after the b-tagging has been applied and the two highest p_T jets are tagged as b-jets. The distributions for all reconstructed and truth matched candidates are normalised to 100 fb^{-1}.

all of these candidates are considered. This means all entries in the reconstructed invariant $b\bar{b}$ mass histograms are counted, assuming they are statistically independent. Figure 7.15 shows the number of Higgs candidates for signal and all considered background processes.

The invariant mass distribution for the best Higgs candidates and their truth matches is shown in Figure 7.16 (left). A Gaussian has been fitted to the truth matched Higgs mass distribution with a peak at 114.2 ± 1.1 GeV and a width of 15.4 GeV (see Figure 7.16).

Figure 7.17 (left) compares the shape of the mass distribution of all Higgs can-

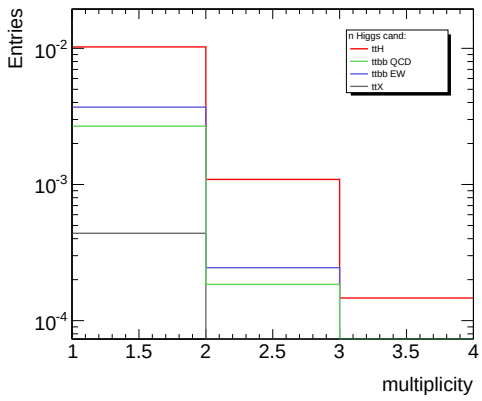

Figure 7.15: Multiplicity of Higgs candidates after all Higgs tagging cuts have been applied for all samples considered, normalised to 100 fb^{-1}.

didates found for signal and all background events and in Figure 7.17 (right) added up corresponding to their cross-sections, normalised to 100 fb^{-1}. It can be seen that invariant Higgs mass spectrum is largely dominated by the $t\bar{t}X$ background, implying the necessity to apply the third b-tag.

The selection efficiency for the signal sample for the Higgs tagging is 12.7%. The corresponding efficiencies for all background samples can be found in Table 7.5.

7.4.6 Triple b-tag

The third b-tag is applied to the event to further suppress the $t\bar{t}X$ background and thereby to enhance the signal-to-background ratio. The constituents of the Higgs and top candidates are removed from the event and the remaining constituents are clustered using the C/A algorithm. The event passes the selection if at least one b-tagged jet with a certain distance in ΔR from the Higgs and top subjets has been found.

In the hadron level analysis, the C/A jets are reconstructed with a parameter of $R = 0.6$. Only jets passing the cuts of $p_T > 30$ GeV and $|\eta| < 2.5$ are considered for b-tagging.

In order to select the best jet reconstruction and b-tagging strategy for the third b-tag, the significance, defined as $\frac{S}{\sqrt{B}}$ has been analysed as a function of the cut applied on the b-tagging weight for three different R parameters of the C/A algorithms,

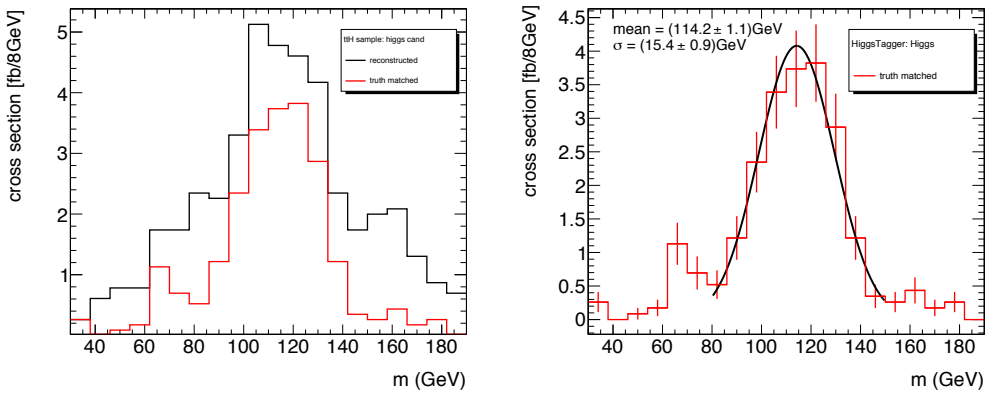

Figure 7.16: Left: Invariant mass distribution of all Higgs candidates and their truth matches reconstructed in signal events. Right: Gaussian distribution fitted to the truth matched Higgs candidates. All distributions are normalised to 100 fb^{-1}.

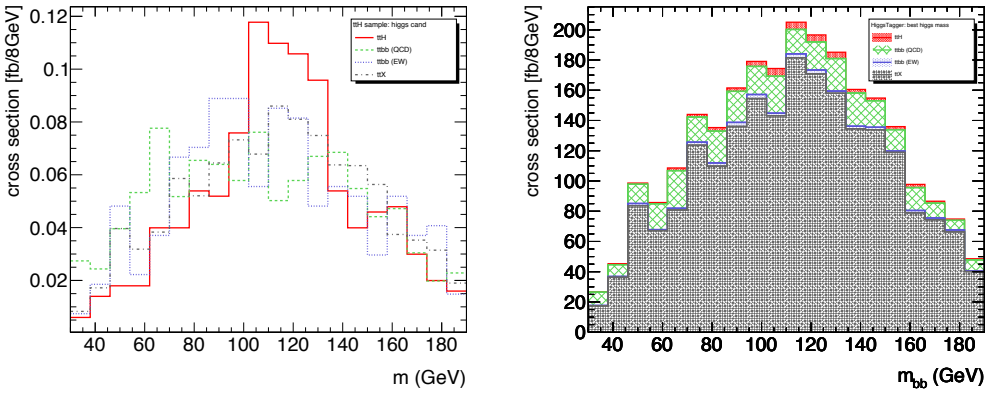

Figure 7.17: Higgs mass distribution of all Higgs candidates found for signal and all background events, normalised to unit area (left) and added up corresponding to their cross-sections, normalised to 100 fb^{-1}.

$R = 0.4, 0.5, 0.6$. The result is shown in Figure 7.18. The b-tagging weights of 0 to 4 correspond to b-tagging efficiencies of roughly 70% down to 40%.

The combination of using a R parameter of $R = 0.4$ and a cut on the b-tagging weight of 2 achieves the highest significance of 0.92σ for an integrated luminosity of 100 fb^{-1}.

Jets are tagged using the JetFitterCOMBNN and considered b-jets if their weight is greater than a weight $W_{jet} > 2$ which corresponds to a b-tagging efficiency of

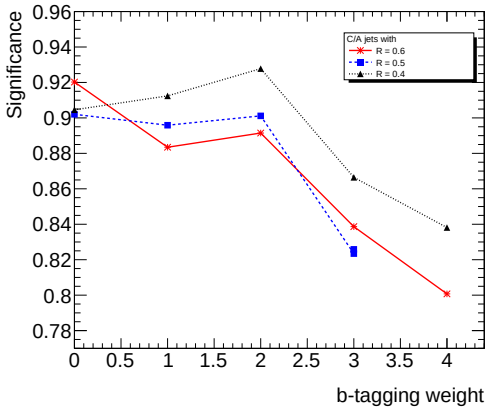

Figure 7.18: Significance versus b-tagging weight cut for jets reconstructed with the C/A algorithm using an R parameter of $R = 0.4$, 0.5 and 0.6.

65.8%, a light jet rejection of 96.6 and a c-jet rejection of 10.2.

If at least one b-tagged jet with a distance of $\Delta R > 0.4$ to the subjets of the reconstructed Higgs and top candidates is found, the event passes the selection. The resulting number of Higgs candidates from events with such a b-jet is shown in Figure 7.19.

The invariant mass distribution of the remaining Higgs candidates and their truth matches after the third b-tag is shown in Figure 7.20 (left). Figure 7.20 (right) shows the mass distribution of truth matched Higgs candidates to which a Gaussian fit has been applied. The Gaussian peaks at a mass of 112.3 ± 1.7 GeV and has a width of 15.1 GeV.

Figure 7.21 shows the final selection of Higgs candidates for signal events in comparison to all background events normalised normalised to 100 fb^{-1}. It can be seen that the shape of the distribution is not ideal for identifying a signal peak due to the very low selection efficiency in the $t\bar{t}X$ sample leading to low statistics. The selection efficiency for applying a third b-tag for signal events is 39.1%. 69.1% of these events lie in a mass window of $m_H = (115 \pm 30)$ GeV. All other efficiencies can be found in Table 7.5.

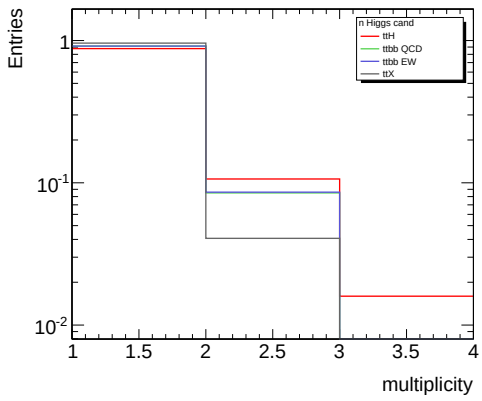

Figure 7.19: Multiplicity of Higgs candidates after the third b-tag requirement has been applied for all samples considered, normalised to 100 fb^{-1}.

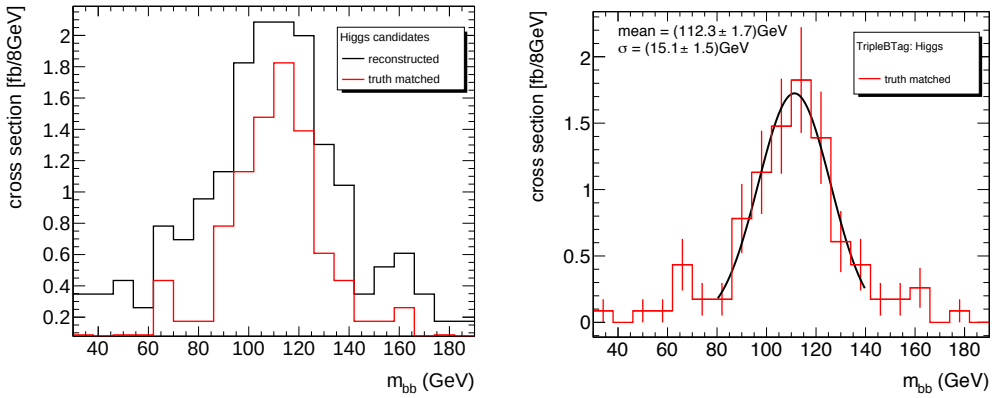

Figure 7.20: Left: Invariant mass distribution of all Higgs candidates and their truth matches found for signal events. Right: Invariant mass distribution of truth matched Higgs candidates to which a Gaussian has been fitted. All distributions are normalised to 100 fb^{-1}.

7.4.7 Results of the Fat Jet Analysis in ATLAS

The baseline of the fat jet analysis was implemented according to the selection in [3]. For this analysis the sensitivity after an integrated luminosity of $L = 100$ fb^{-1} of data, considering only statistical errors and a Higgs boson mass of 120 GeV is $S/\sqrt{B} = 0.92\sigma$ and a signal-to-background ratio of $S/B = 0.07$. Table 7.6 summarises the number of reconstructed Higgs candidates, the signal-over-background ratio and the significance after applying the Higgs tag and after the third b-tag.

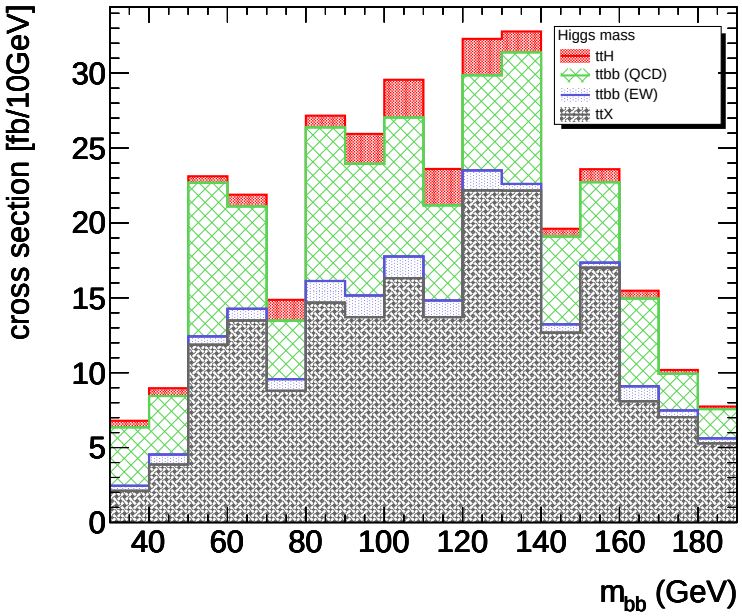

Figure 7.21: Higgs mass distribution of all Higgs candidates after the third b-tag has been applied including signal and all backgrounds normalised to 100 fb^{-1}.

The number of background candidates has been reduced by 88.1%, with the biggest fraction being $t\bar{t}X$ candidates, leading to a higher signal-to-background ratio and significance after applying a third b-tag.

Step of analysis	Signal	Backgrounds			S/B	$S/\sqrt{B}$
		$t\bar{t}b\bar{b}$ QCD	$t\bar{t}b\bar{b}$ EW	$t\bar{t}X$		
Higgs tagging	28.0	152.0	15.8	1173.7	0.02	0.76
Triple b-tag	11.7	50.8	6.8	105.0	0.07	0.92

Table 7.6: Number of signal and background events, signal-over-background ratio and significance after tagging a Higgs jet and after applying the third b-tag for an integrated luminosity of L = 100 fb^{-1}.

7.5 Comparison of the Hadron and Detector Level Analyses

The obtained significance of the hadron level analysis of 4.5σ and the signal-to-background ratio of $S/B = 1/2.4$ for an integrated luminosity of 100 fb^{-1}, a Higgs boson mass of 120 GeV and a centre-of-mass energy of $\sqrt{s} = 14$ TeV has been a promising result in extracting the Higgs production process $t\bar{t}H^0(H^0 \to b\bar{b})$.

The implementation of this analysis in the ATLAS detector environment using simulated data with a centre-of-mass energy of $\sqrt{s} = 10$ TeV and a Higgs boson mass of 120 GeV has yielded a statistical significance of 0.92σ and signal-over-background ratio of $S/B = 1/13.3$. With the scaling factor of $\sqrt{2.47} = 1.57$ obtained from the centre-of-mass energy considerations in Section 7.4.1, the significance scales to 1.45σ assuming signal and background scale the same for a centre of mass energy of $\sqrt{s} = 14$ TeV.

Table 7.7 lists the efficiencies obtained for the hadron level analysis (top) which can be directly compared to those of the detector level analysis (bottom). The selection efficiencies for the top tagger are higher for the detector level analysis due the larger mass window cut which was applied to the reconstructed top and W candidates. Generally the detector level analysis is roughly twice as efficient as the hadron level analysis for signal events. For $t\bar{t}b\bar{b}$ EW and QCD backgrounds, the overall efficiency of the detector level analysis is about 4 and 2 times higher, for $t\bar{t}X$ background even 40 times higher.

The number of Higgs candidates per 1 fb^{-1} after the Higgs tagging and after applying the third b-tag for both analysis are compared in Table 7.8. The reduction factor of entries after the Higgs tagging and the third b-tag is roughly the same for the $t\bar{t}H^0$ and $t\bar{t}b\bar{b}$ EW dataset, however for the $t\bar{t}b\bar{b}$ QCD and the $t\bar{t}X$ sample it differs by quite a lot, with the detector level analysis having an almost 3 times higher reduction rate for $t\bar{t}b\bar{b}$ QCD but a 2 times lower reduction rate of $t\bar{t}X$ events. A plausible explanation for these differences can be found in the differences of the Monte Carlo samples used in the analysis, which are discussed in more detail below.

Hadron level analysis	$t\bar{t}H^0$	$t\bar{t}b\bar{b}$ EW	$t\bar{t}b\bar{b}$ QCD	$t\bar{t}X$
Top tag	42.3% (42.3%)	42.0% (42.0%)	36.8% (36.8%)	35.0% (35.0%)
Higgs tag	9.8% (4.1%)	2.8% (1.2%)	3.2% (1.2%)	0.1% (0.03%)
Triple b-tag	48.0% (2.0%)	37.5% (0.4%)	47.4% (0.6%)	4.3% (0.001%)

ATLAS level analysis	$t\bar{t}H^0$	$t\bar{t}b\bar{b}$ EW	$t\bar{t}b\bar{b}$ QCD	$t\bar{t}X$
Top tag	57.5% (57.5%)	50.8% (50.8%)	48.9% (48.9%)	46.4% (46.4%)
Higgs tag	14.2% (8.1%)	7.1% (3.6%)	8.7% (4.2%)	1.2% (0.6%)
Triple b-tag	46.1% (3.7%)	47.8% (1.7%)	33.3% (1.4%)	6.9% (0.04%)

Table 7.7: Selection efficiencies for the top tagging, Higgs tagging and the third b-tag for the hadron level analysis (top) and the detector (ATLAS) level analysis (bottom). The overall efficiencies for the analysis are given in brackets.

The large difference in the performance of the hadron and detector level analysis can be traced back to the differences between the Monte Carlo samples used in the analyses and the performance assumptions of lepton identification and isolation and b-tagging efficiency and purity.

The most significant differences of the simulated samples used in the hadron level analysis are the following:

- $t\bar{t}b\bar{b}$ QCD sample: Acceptance cuts $|y_b| < 2.5$, $p_{T,b}$ >20 GeV and $R_{b\bar{b}} > 0.8$ have been applied to this sample in the hadron level analysis. This is possibly the reason for the higher reduction rate observed in the detector level analysis when applying the third b-tag, since no $R_{b\bar{b}}$ has been applied to the samples used.

- A so-called *k-factor* has been applied to the signal and $t\bar{t}b\bar{b}$ background samples used in the hadron level analysis to account for higher-order effects (next-to-leading order effects (NLO)). For $t\bar{t}b\bar{b}$ QCD, a k-factor of 2.3 has been applied (after the acceptance cuts mentioned above have been applied), compared to k = 1.57 for the signal. The k-factor applied to the $t\bar{t}b\bar{b}$ EW sample is k =

Hadron level analysis	$t\bar{t}H^0$	$t\bar{t}b\bar{b}$ EW	$t\bar{t}b\bar{b}$ QCD	$t\bar{t}X$
Higgs tagging	1.0	0.08	2.3	1.4
Triple b-tag	0.48	0.03	1.09	0.06
reduction factor	2.1	2.7	1.2	23.3

Detector level analysis	$t\bar{t}H^0$	$t\bar{t}b\bar{b}$ EW	$t\bar{t}b\bar{b}$ QCD	$t\bar{t}X$
Higgs tagging	0.28	0.16	1.52	11.74
Triple b-tag	0.12	0.07	0.51	1.05
reduction factor	2.3	2.3	3.0	11.2

Table 7.8: Number of Higgs candidates per 1 fb^{-1} after the Higgs tagging and after applying the third b-tag for the hadron level analysis (top) and the detector level analysis (bottom). The last row of each table gives the reduction factor when the third b-tag is applied.

1.35 [89]. For $t\bar{t}$+ jets production no higher-order correction has been applied because the background rejection cuts drive it into kinematic configuration in which a constant k-factor cannot be used. Using these k-factors enhances the significance by roughly 0.5σ for an integrated luminosity of 100 fb^{-1}. The significance for the hadron level analysis without applying k-factors is therefore found to be 4.0σ.

- No $g \to b\bar{b}$ splitting has been included to any of the samples in the hadron level analysis. In the analysis presented here, $g \to b\bar{b}$ splitting has been applied, which means it is more likely for background events to pass the Higgs reconstruction and the third b-tag requirement due to a higher b-jet multiplicity. This would then result in a lower reduction rate of entries for the detector level analysis when the third b-tag is applied.

- The centre-of-mass energy at which the hard process was simulated is $\sqrt{s} =$ 14 TeV. This can be compensated by applying a scaling factor in order to compare results (see Section 7.4.1).

The hadron level analysis assumes a lepton identification and isolation efficiency

of 80% which is, compared to the lepton preselection efficiency in signal events about 20% higher. A more severe assumption the hadron level analysis makes is the b-tagging performance in the Higgs tagger of 70% with a mistagging probability of 1% which corresponds to a light jet rejection of 100. The b-tagging efficiency in the detector level Higgs tagger is 63.0% with a light jet rejection of 72.5 and a c-jet rejection of 7.3. So there is quite a difference in b-tagging performance, causing fewer signal events to pass due to the lower b-tagging efficiency but also more background events to go through due to the reduced light jet rejection. For the third b-tag, a b-tagging efficiency of 60% with purity of 2%, corresponding to a light jet rejection of 50, is assumed. In the detector level analysis the b-tagging efficiency of 65.8%, a light jet rejection of 96.6 and a c-jet rejection of 10.2 has been chosen to reduce the number of selected $t\bar{t}X$ events.

Overall the differences in the simulated samples as well as the b-tagging performance in the Higgs tagger and the lepton identification and isolation efficiency can explain the observed difference in performance between the two analyses reasonably well.

7.6 Systematic Uncertainties

The fat jets analysis is expected have a significant reduction in the systematic uncertainties compared to the cut-based analysis presented in Chapter 5. The reason lies in the way of reconstructing the event which differs significantly from the cut-based analysis: By applying three instead of four b-tag, the b-tagging uncertainty will be reduced. Additionally, the lower multiplicity of required jets with a very high transverse momentum (two jets compared to six in the cut-based analysis) will reduce the jet energy scale uncertainty contribution. The estimation of systematic uncertainties due to the standard detector effects has been investigated for the cut-based CSC analysis [5] and is summarised in Table 5.12.

Additionally to the systematic uncertainties from detector effects, the analysis of the $t\bar{t}H^0$ channel suffers mainly from the large uncertainty in the prediction of the background from top quark pairs with additional jets. The leading-order

cross-section calculation is very sensitive to the choice of the renormalisation and factorisation scale [60]. This indicates a significant contribution from higher order corrections, it is therefore essential to measure the rate of the $t\bar{t}X$ background from real data and to tune the Monte Carlo generators accordingly. For an extraction of the $t\bar{t}H^0$ signal peak in the $m_{b\bar{b}}$ mass spectrum it is likewise important to know the shape of the background, especially that of the irreducible $t\bar{t}b\bar{b}$ background. A robust method to infer background shapes and normalisation from data has yet to be developed for this analysis.

However, it is possible to investigate the impact of the systematic uncertainties in the background prediction and their effect on the statistical significance. The statistical significance $\frac{S}{\sqrt{B}}$ evaluated in Section 7.4.7 is based on simple counting of Higgs candidates and gives a first evaluation of the discovery sensitivity of the $t\bar{t}H^0(H^0 \rightarrow b\bar{b})$ analysis to a Standard Model Higgs boson with a mass around 120 GeV. However, this significance can only be realised under the assumption that the number of expected background events is known very precisely. Depending on the uncertainty in the theoretical prediction of the differential cross-section of the backgrounds in the selected region of phase space and depending on the uncertainty on the background acceptance as predicted by Monte Carlo simulations, this uncertainty ΔB on B, can be very high. To understand how this uncertainty propagates into the sensitivity of this channel to the discovery of a Higgs boson, the statistical uncertainty on the background $\sqrt{B}$ is summed up in quadrature with the systematic uncertainty ΔB. The corrected significance then takes the form $\frac{S}{\sqrt{B+\Delta B}}$. This corrected significance is shown in Figure 7.22 as a function of $\frac{\Delta B}{B}$ after applying the third b-tag. The significance of 0.92σ in the perfect case is found to be reduced to about 0.6σ in the case of a 10% uncertainty and to roughly 0.45σ in the case of a 15% uncertainty on the background. These background uncertainty values are not unrealistic as the systematic uncertainties are expected to be reduced in this analysis from the 22% quoted in Table 5.12.

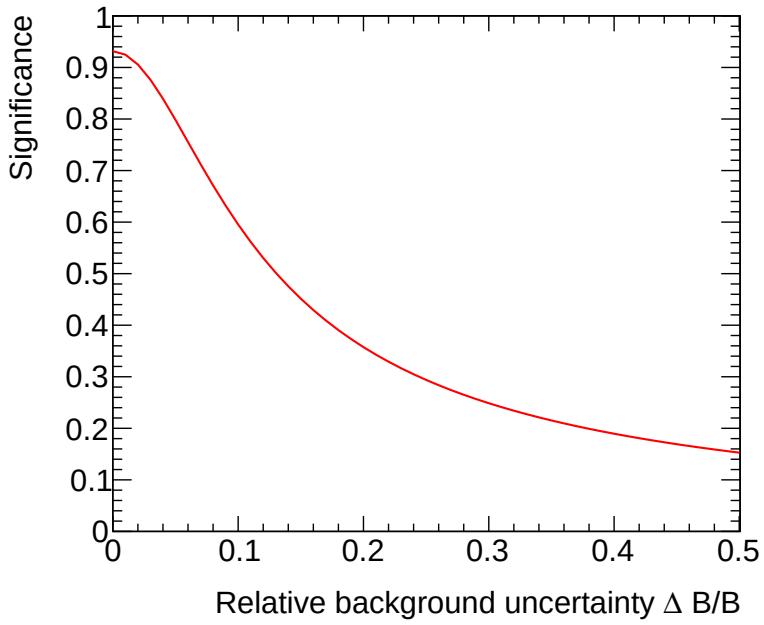

Figure 7.22: Discovery significance for a 120 GeV Higgs boson as a function of the systematic uncertainty on the background $\frac{\Delta B}{B}$ for an integrated luminosity of 100 fb^{-1} after applying the third b-tag. No further systematic uncertainties are considered here.

7.7 Conclusion

A first study of the ALTAS sensitivity to the associated $t\bar{t}H^0$ production at high-p_T for a low mass Standard Model Higgs boson using a realistic simulation of the the ATLAS detector has been presented. The analysis follows closely that of [3]. For the analysis presented here, a sensitivity of 0.92σ for an integrated luminosity of 100 fb^{-1} and a centre-of-mass energy of 10 TeV was achieved. If the major backgrounds have a systematic uncertainty of around 10% this sensitivity drops to 0.6σ for $\sqrt{s} = 10$ TeV.

The achieved sensitivity corresponds to a statistical sensitivity of 1.45σ for an integrated luminosity of 100 fb^{-1} at a centre-of-mass energy of 14 TeV. The hadron level analysis yielded a significance of 4.5σ, which is much higher than the detector level analysis but it is possible to explain the discrepancy with the choice of the settings for the simulated data and the performance of the b-tagging and lepton

identification and isolation efficiency (see Chapter 7.5).

All numbers are based on signal and background processes generated at LO and normalised to their respective LO cross-sections. The use of dedicated NLO generators, whenever possible, is foreseen for a future update of the analysis.

Further improvements can be expected in this analysis with respect to refined reconstruction methods such as the top or Higgs tagging. Generally, the necessity of a strong b-tagging algorithm emerges from this study, as it is of great importance for the Higgs reconstruction as well as for the suppression of the $t\bar{t}X$ background. Since two steps of the analysis rely heavily on b-tagging, efforts might be made in terms of calibration and further optimising for this specific kinematic region, resulting in a higher b-tagging efficiency while at the same time preserving a similar light- and charm-jet rejection. No jet calibrations have been applied in this analysis, therefore the development of a calibration to these specific jets will improve the mass resolutions of the reconstructed objects. The sensitivity could be additionally enhanced by using more sophisticated and advanced multivariate techniques compared to presented cut-based analysis presented here.

In addition, this channel could give information on the $H \rightarrow b\bar{b}$ coupling and therefore be an important channel together with the WH/ZH channels to determine parameters of the Higgs sector [90]. More importantly it will give direct access to the top-Higgs Yukawa coupling. Although it has been shown by recent CMS and ATLAS studies that the combinatorial backgrounds (in the low p_T analyses) make it very hard to observe this decay in the $t\bar{t}H^0$ production, it may still be realisable when considering possible improvements to this analysis and combining the subjet analysis together with the cut-based analysis (or any more sophisticated analysis) for the low-p_T region. This combination of low- and high-p_T analyses is further exploited in Section 8.

In conclusion, the reinstatement of the $t\bar{t}H^0(H^0 \rightarrow b\bar{b})$ channel in the high-p_T region as a promising search and measurement channel for the low-mass Standard Model Higgs boson using a realistic ATLAS detector simulation as predicted by the hadron level analysis paper [3] has not been possible to confirm. Further improvements of the detector analysis have to be done, including the use of sophisticated

multivariate techniques to enhance the sensitivity compared to the relatively simple cut-based analysis.

Chapter 8

Combining the Low p_T and High p_T Analyses

8.1 Motivation

The combination of the low p_T (cut-based) analysis (see Chapter 5) and the high p_T (fat jets/boosted) analysis (see Chapter 7) is performed. This has been done as events are selected in complementary regions of phase space, thereby increasing the sensitivity of the $t\bar{t}H^0(H^0 \to b\bar{b})$ channel.

8.2 Analyses Performance on a Common Dataset

The results of both analyses are reviewed in this chapter when run separately on the same simulated data described in Chapter 7.4.1. These datasets have been generated for the purpose of performing the fat jet analysis; no requirements on the minimum number of jets in form of the *TtbarPlusJetsFilter* (see Section 5.2.1 for details) is made compared to the simulated data used in the cut-based analysis.

8.2.1 Cut-based Analysis

The cut-based analysis has been described in detail in Chapter 5. The selection efficiencies for the different steps of the analysis are summarised in Table 8.1. The efficiencies for the signal sample are expected to be the same, but since the *TtbarPlus-*

Step of analysis	$t\bar{t}H^0$	$t\bar{t}b\bar{b}$ EW	$t\bar{t}b\bar{b}$ QCD
Lepton preselection	61.3% (61.3%)	61.1% (61.1%)	60.4% (60.4%)
Jet preselection	6.6% (4.0%)	3.6% (2.2%)	2.2% (1.3%)
leptonic W	95.7% (3.8%)	96.8% (2.1%)	95.8% (1.3%)
hadronic W	69.6% (2.7%)	69.1% (1.5%)	66.8% (0.8%)
$t\bar{t}$ system	91.9 % (2.5%)	90.8% (1.3%)	89.1% (0.7%)
Higgs	95.9% (2.4%)	95.6% (1.3%)	93.8% (0.7%)

Step of analysis	$t\bar{t}$+0p	$t\bar{t}$+1p	$t\bar{t}$+2p	$t\bar{t}$+ >3p
Lepton preselection	64.2% (64.2%)	62.3% (62.3%)	59.9% (59.9%)	56.8% (56.8%)
Jet preselection	0.002% (0.001%)	0.02% (0.01%)	0.08% (0.05%)	0.2% (0.1%)
leptonic W	93.3% (0.001%)	95.7% (0.01%)	97.7% (0.05%)	96.7% (0.1%)
hadronic W	57.1% (00.01%)	44.4% (0.005%)	49.2% (0.02%)	70.7% (0.07%)
$t\bar{t}$ system	62.5% (0.0005%)	80.0% (0.004%)	82.3% (0.02%)	87.5% (0.06%)
Higgs	100.0% (0.0005%)	96.9% (0.004%)	93.0% (0.02%)	94.6% (0.06%)

Table 8.1: Efficiencies of each step of the analysis for signal and $t\bar{t}b\bar{b}$ backgrounds (top) and $t\bar{t}X$ samples (bottom). The efficiencies are calculated on a tool-by-tool basis and as overall efficiencies in brackets. The Higgs reconstruction efficiency quoted is for the reconstruction method using the two b-jet with the highest b-weight, and the mass window applied is optimised to this approach.

JetsFilter has not been applied to the background datasets, they have a lower overall selection efficiency.

The resulting invariant Higgs mass spectrum for signal and background events added up is shown in Figure 8.1.

In the mass window of (105±30) GeV the statistical significance is found to be $\frac{S}{\sqrt{B}} = 1.75\sigma$ (0.96σ) for an integrated luminosity of 100 fb^{-1} (30 fb^{-1}) and a signal-to-background ratio of $\frac{S}{B} = 0.07$ (0.07), the number of signal and background events are listed in Table 8.2. For a mass window of (110±30) GeV the significance is $\frac{S}{\sqrt{B}}$ $= 1.69\sigma$ (0.93σ) for an integrated luminosity of 100 fb^{-1} (30 fb^{-1}) with a signal-to-background ratio of $\frac{S}{B} = 0.07$ (0.07). Compared to the results in Chapter 5, the significance and signal-to-background ratio are lower when running on simulated datasets which were generated without the *TtbarPlusJetsFilter*. This is probably due to the choice of jet algorithms applied in the TtbarPlusJetsFilter at hadron level, where a seeded fixed-cone algorithm was used to reconstruct jets whereas in the analysis, the Anti $-$ k$_{\mathrm{T}}$ algorithm has been used. While the number of signal events remains the same (no jet filter applied to this sample), more events from the background samples are selected.

8.2.2 Fat Jets Analysis

The fat jet analysis has been described in detail in Chapter 7. The selection efficiencies for the different steps of the analysis are summarised in Table 7.5. The resulting invariant Higgs mass spectrum after the three b-tag analysis for signal only and signal and background events added up is shown in Figure 8.2.

For this analysis the sensitivity after an integrated luminosity of 100 fb^{-1}, considering only statistical errors and a Higgs boson mass of 120 GeV, is 0.93σ and a signal-to-background ratio of $S/B = 0.07$ evaluated for a Higgs mass window of $m_H = (115 \pm 30)$ GeV.

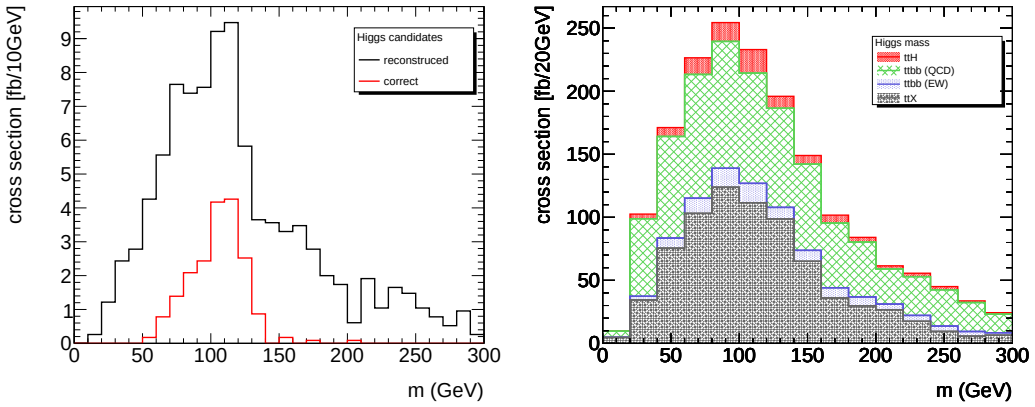

Figure 8.1: Left: The Higgs boson mass reconstructed from the two b-jets with the highest b-weight for the signal sample for $m_{H^0} = 120$ GeV given in cross-sections, the red line indicates Higgs candidates formed by assigning the correct b-jets. Right: Signal and background events added up corresponding to their cross-sections. Both mass distributions are normalised to 100 fb^{-1}, the simulated datasets used have no minimum number of jets requirement applied.

8.3 Evaluation of Overlap between the Low and High p_T Analysis

When running the two analyses on a common dataset, for some events, Higgs candidates are reconstructed by both; This has to be treated with care when combining the analyses.

Table 8.3 lists the number of events for signal and background datasets which were reconstructed by both analyses at different steps of the analyses: after the preselection since the selection of leptons is the same in both analyses; after the jet preselection which selects slightly different areas of phase space; after the Higgs reconstruction; and for the mass windows which were chosen for the significance estimates. It is important to note that for the fat jet analysis it is indeed possible to reconstruct more than one Higgs candidate per event, whereas for the cut-based analysis, only one Higgs candidates per event is reconstructed.

The invariant Higgs mass distribution for all overlapping events after the Higgs reconstruction is shown in Figure 8.3 for signal and all background samples. From

analysis	integrated luminosity	Signal	Backgrounds			S/B	$S/\sqrt{B}$
			$t\bar{t}b\bar{b}$ QCD	$t\bar{t}b\bar{b}$ EW	$t\bar{t}X$		
cut-based	30 fb^{-1}	13.6	83.0	12.1	106.2	0.07	0.96
	100 fb^{-1}	45.4	275.6	40.5	354.1	0.07	1.75
fat jet	30 fb^{-1}	3.5	15.2	2.0	30.5	0.07	0.51
	100 fb^{-1}	11.7	50.8	6.8	101.6	0.07	0.93

Table 8.2: Number of signal and background events, signal-to-background ratio S/B and the statistical significance $S/\sqrt{B}$ for the cut-based and fat jet (including the third b-tag) analyses presented in this thesis using a mass window of (105±30) GeV for the cut-based analysis and a mass window of (115±30) GeV for the fat jets analysis. Results are shown for an integrated luminosity of 30 fb^{-1} and 100 fb^{-1}.

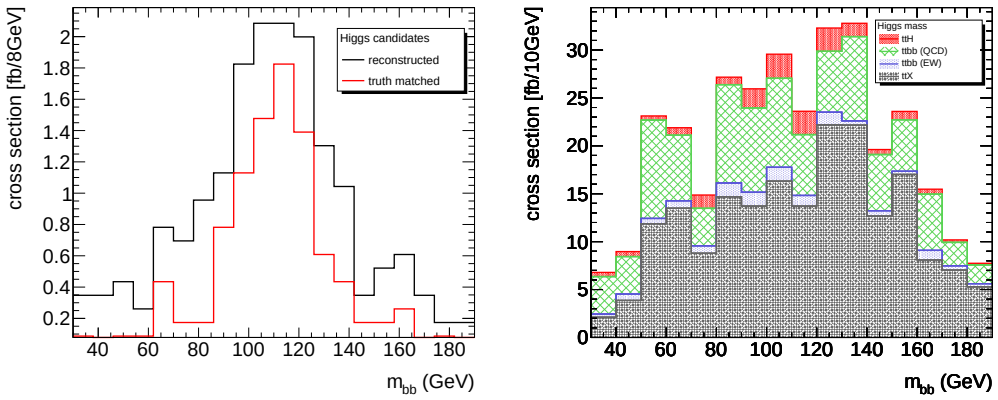

Figure 8.2: Invariant mass distribution of all Higgs candidates for the fat jets analysis. Left: All Higgs candidates and their truth matches found for signal events. Right: Higgs candidates of signal and all backgrounds normalised to 100 fb^{-1}.

these distributions it can be seen that especially for the signal sample, more Higgs candidates can be found around the generated Higgs mass for the fat jets analysis than for the cut-based analysis. The distributions of overlapping events for the $t\bar{t}b\bar{b}$ QCD sample have different shapes, with the candidates reconstructed with the fat jet analysis peaking around 100 GeV, due to the the signal selection cuts such as the W and top mass windows. The $t\bar{t}b\bar{b}$ EW and $t\bar{t}X$ overlap distributions suffer from low statistics, a shape comparison is therefore not possible.

analysis step	Signal	Backgrounds		
		$t\bar{t}b\bar{b}$ QCD	$t\bar{t}b\bar{b}$ EW	$t\bar{t}X$
Preselection	85.5 (2.8%)	541.9 (0.46%)	136.4 (2.3%)	45.23 (0.01%)
(event based)	85.5 (13.1%)	541.9 (5.9%)	136.4 (12.8%)	45.23 (0.08%)
Higgs	5.6 (5.6%)	31.8 (3.6%)	3.9 (3.2%)	9.4 (0.7%)
	6.4 (34.6%)	32.7 (29.1%)	3.8 (25.2%)	9.4 (3.1%)
Higgs in	2.0 (4.4%)	5.4 (1.9%)	0.9 (2.2%)	4.4 (0.9%)
mass window	2.1 (17.7%)	5.4 (10.6%)	1.0 (14.8%)	4.4 (5.3%)

Table 8.3: Number of events and Higgs candidates (for the fat jet analysis) for signal and background datasets after three different steps in the analysis. The first line corresponds to the cut-based analysis, the second to the fat jet analysis. The number in brackets give the percentage of overlapping events/candidates in each analysis. For the cut-based analysis only one Higgs candidate per event can be reconstructed whereas for the fat jet analysis more than one is possible. The mass window for the Higgs candidates for the cut-based analysis was chosen to be (105±30) GeV and for the fat jet analysis (115±30) GeV. Numbers are normalised to 100 fb^{-1}.

The signal-to-background ratios evaluated for this overlap for the corresponding mass windows for the fat jet and the cut-based analysis are 1/5.1 and 1/5.4, respectively. Both signal-to-background ratios are close together, so no conclusion about with which analysis the overlap should be identified can be drawn. Therefore the reconstruction of the overlapping events with both analyses will be studied.

8.4 Combination of Analyses

To evaluate an overall significance for the $t\bar{t}H^0(H^0 \to b\bar{b})$ channel, the results of the analysis must be combined. The combination of the WH/ZH channels presented in [35] uses a profile likelihood method (see Higgs Boson Chapter in [5]). From this combination it was concluded that the observed median significance obtained through the profile likelihood method is consistent with what would be expected from adding the $S/\sqrt{B}$ in quadrature, assuming perfect understanding of the backgrounds.

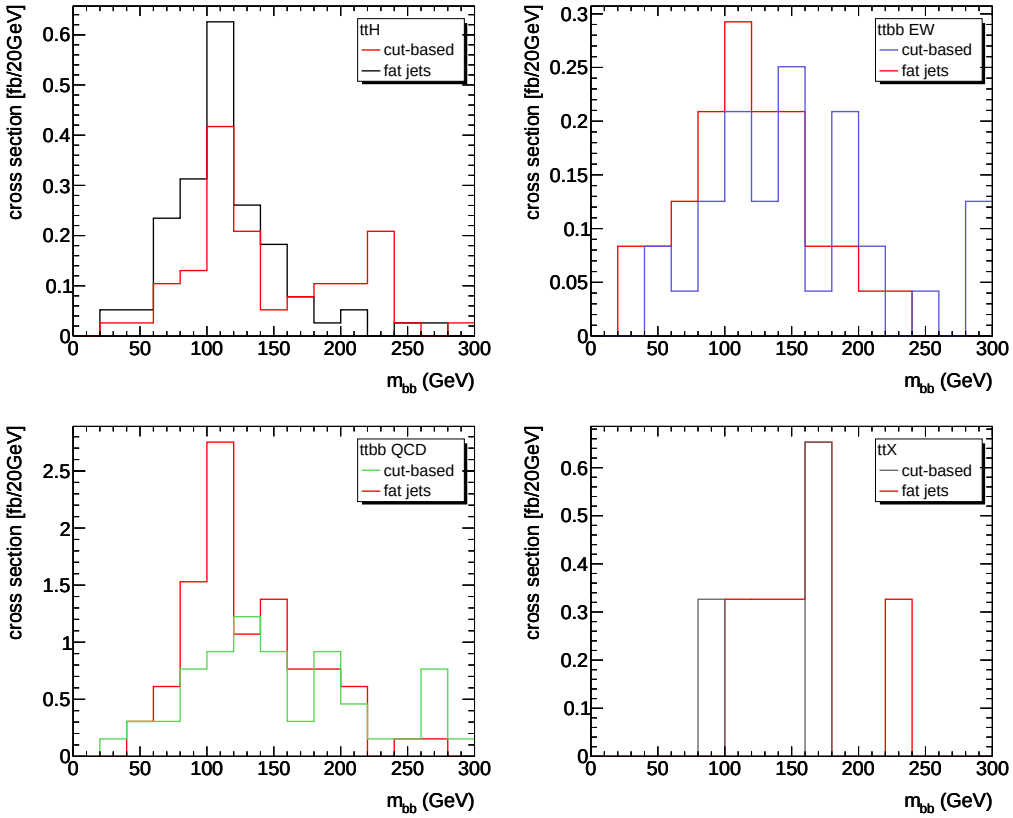

Figure 8.3: Invariant mass distribution of Higgs candidates for the $t\bar{t}H^0$ (top left), $t\bar{t}b\bar{b}$ EW (top right), $t\bar{t}b\bar{b}$ QCD (bottom left) and $t\bar{t}X$ (bottom right) samples, normalised to 100 fb^{-1}.

Therefore, the estimation of the overall significance of the analyses presented here will be achieved by adding the obtained $S/\sqrt{B}$ in quadrature. The treatment of events in which both analyses reconstructed Higgs candidates will be done by first running the fat jets (cut-based) analysis on the common dataset, and then running the cut-based (fat jets) analysis on the remaining events, in which no Higgs candidate has been found.

8.4.1 Fat Jets and Cut-based Combination

First the fat jets analysis is run on the dataset and the remaining events, in which no Higgs candidate has been found, are then analysed with the cut-based analysis. Figure 8.4 shows the Higgs mass distributions for the fat jets analysis and the cut-

based analysis for signal and background.

The significance calculation is done separately for both distributions, since the mass windows used are different for the two analyses. Table 8.4 summarises the number of signal and background events, the signal-to-background ratio and the significance obtained separately for the two analyses.

Both significances are added up in quadrature and result in an overall statistical significance of $S/\sqrt{B} = \sqrt{(0.93)^2 + (1.67)^2} = 1.91\sigma$ for an integrated luminosity of 100 fb^{-1}. This corresponds to a statistical significance of 2.80σ for a centre-of-mass energy of $\sqrt{s} = 14$ TeV, using the scaling factors obtained in Chapters 5.2.2 and 7.4.1 for the two analyses.

This way of evaluating the overall significance is also consistent with treating the two sets of signal and backgrounds obtained from the two analyses as one set, as if obtained from a single analysis.

8.4.2 Cut-based and Fat Jets Combination

Now the cut-based analysis is run first, then the remaining events are reconstructed with the fat jets analysis. Figure 8.5 shows the Higgs mass distributions for the fat jets analysis and the cut-based analysis for signal and background.

The significance is again calculated separately for both distributions due to the different mass windows applied in the two analyses. The number of signal and background events, the signal-to-background ratio and the significance obtained are summarised in Table 8.5.

Both significances are added up in quadrature and result in an overall statistical

analysis	Signal	Backgrounds			S/B	$S/\sqrt{B}$
		$t\bar{t}b\bar{b}$ QCD	$t\bar{t}b\bar{b}$ EW	$t\bar{t}X$		
fat jets	11.7	50.8	6.8	101.6	0.07	0.93
cut-based	42.9	268.3	39.3	353.5	0.06	1.67

Table 8.4: Number of signal and background events, signal-to-background ratio and significance, normalised to 100 fb^{-1}, for the fat jets and cut-based analysis. Overlapping events have been reconstructed with the fat jets analysis.

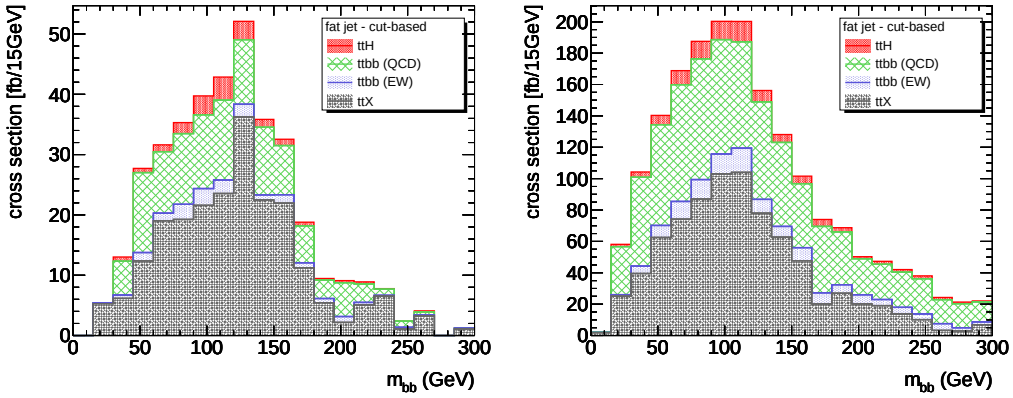

Figure 8.4: Invariant Higgs mass distribution for the fat jet analysis (left) and cut-based analysis (right) for all signal and background events when first reconstructing events with the fat jets analysis and the remaining events with the cut-based analysis. Distributions are normalised to 100 fb^{-1}.

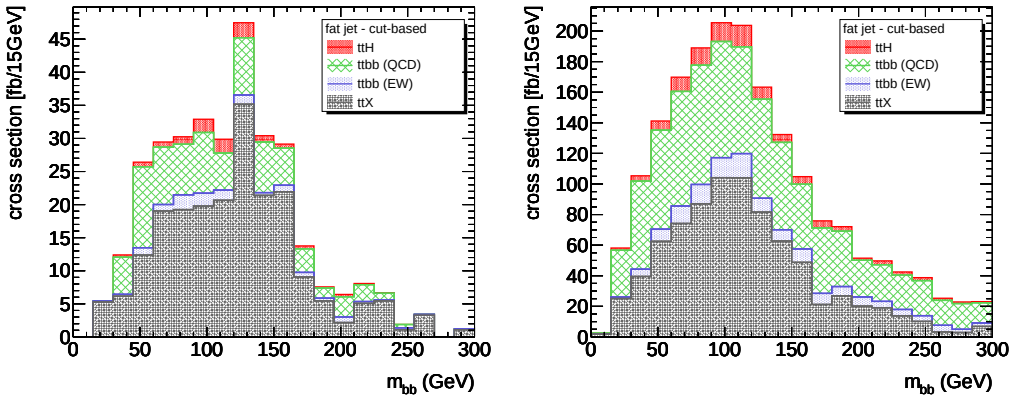

Figure 8.5: Invariant Higgs mass distribution for the fat jet analysis (left) and cut-based analysis (right) for all signal and background events when first reconstructing events with the cut-based analysis and the remaining events with the fat jets analysis. Distributions are normalised to 100 fb^{-1}.

analysis	Signal	Backgrounds			S/B	$S/\sqrt{B}$
		$t\bar{t}b\bar{b}$ QCD	$t\bar{t}b\bar{b}$ EW	$t\bar{t}X$		
cut-based	7.6	34.3	4.9	96.0	0.06	0.65
fat jets	45.5	276.6	40.5	358.0	0.07	1.75

Table 8.5: Number of signal and background events, signal-to-background ratio and significance, normalised to 100 fb^{-1}, for the fat jets and cut-based analysis. Overlapping events have been reconstructed with the cut-based analysis.

significance of $S/\sqrt{B} = \sqrt{(0.65)^2 + (1.75)^2} = 1.87\sigma$ for an integrated luminosity of 100 fb^{-1}. The significances can be scaled separately to a centre-of-mass energy of $\sqrt{s} = 14$ TeV (see Chapters 5.2.2 and 7.4.1) resulting in a statistical significance of 2.70σ for an integrated luminosity of 100 fb^{-1}.

8.5 Results and Conclusion

The combination of both analysis, the boosted fat jets analysis and the low p_T cut-based analysis has been presented in this Chapter. It was found that the combination achieves the best result in terms of statistical significance when the events in which Higgs candidates are both reconstructed from the fat jets and cut-based analysis, are actually reconstructed by the fat-jet analysis. A statistical significance of 1.9σ has been obtained for an integrated luminosity of 100 fb^{-1} for a centre-of-mass energy of $\sqrt{s} = 10$ TeV. This result scales to 2.8σ for a centre-of-mass energy of $\sqrt{s} = 14$ TeV for 100 fb^{-1} and to 1.5σ for 30 fb^{-1}.

This is in fact a lower significance than achieved by the cut-based analysis in Chapter 5, however it was found that the TtbarPlusJetsFilter applied when generating the events, seems to remove events from the samples which would be otherwise reconstructed by the analysis.

Chapter 9

Conclusions

Searches for the Higgs boson have been one of the primary pursuits at past and present particle accelerators. The $t\bar{t}H^0(H^0 \rightarrow b\bar{b})$ channel is one of the most challenging processes which could contribute to a Higgs discovery in the low mass range. This region is particularly difficult and various channels have to be studied to achieve a 5σ observation. More importantly, once this channel has been discovered, it will give direct access to the top-Higgs Yukawa coupling.

This thesis presented two search strategies for a Higgs boson mass of 120 GeV in a realistic simulation of the ATLAS detector at a centre-of-mass energy of $\sqrt{s} =$ 10 TeV. In a previous run plan of the Large Hadron Collider (LHC), a longer run period at this centre-of-mass energy had been foreseen. Both studies rely on Monte Carlo events generated with LO Monte Carlo generators.

One analysis focuses on the complete reconstruction of the two top-quarks in the event to reduce the large backgrounds. To identify the top quark pairs and the Higgs boson through their decay products, a cut-based approach has been implemented. In the most recent study [5], the expected statistical significance for this analysis was found to be 1.82σ for a Higgs boson mass of 120 GeV at a centre-of-mass energy of $\sqrt{s} = 14$ TeV and an integrated luminosity of 30 fb^{-1}. The updated analysis presented in this thesis found a statistical significance of 1.1σ at a centre-of-mass energy of $\sqrt{s} = 10$ TeV for an integrated luminosity of 30 fb^{-1}. Based on a cross-section study, the significance can be scaled to a centre-of-mass energy of $\sqrt{s} =$ 14 TeV, resulting in a significance of 1.57σ.

The second analysis presented in this thesis is a first detector level study of the $t\bar{t}H^0(H^0 \to b\bar{b})$ search channel which is based on a new method employing state-of-the-art jet reconstruction and decomposition techniques where the $t\bar{t}$ pair and Higgs boson are required to have large transverse momenta and can therefore be reconstructed as massive, fat jets. The identification of the Higgs boson relies on a recently proposed algorithm [4] which has been adapted in [3] by constructing Higgs and top taggers for tagging in busy environments at moderately high transverse momentum. The hadron level study gives a statistical significance of at least 4.5σ for a Higgs boson mass of 120 GeV and a centre-of-mass energy of $\sqrt{s} = 14$ TeV for an integrated luminosity of 100 fb^{-1}. The statistical significance of the implementation of the analysis in the ATLAS environment was found to be 0.92σ for a centre-of-mass energy of $\sqrt{s} = 10$ TeV and integrated luminosity of 100 fb^{-1}, scaling to a 1.45σ significance for a centre-of-mass energy of $\sqrt{s} = 14$ TeV. If the major backgrounds have a systematic uncertainty of around 10% this sensitivity drops to 0.6σ for $\sqrt{s} =$ 10 TeV. More work towards an improvement of the sensitivity has to be done and can certainly be expected.

The feasibility of a combination of the two analyses was investigated. The best result in terms of statistical significance was obtained by reconstructing the overlap with the fat jets analysis. For an integrated luminosity of 100 fb^{-1} and for a centre-of-mass energy of $\sqrt{s} = 10$ TeV a statistical significance of 1.91σ was found. This result scales to 2.80σ for a centre-of-mass energy of $\sqrt{s} = 14$ TeV for 100 fb^{-1} and to 1.53σ for 30 fb^{-1}.

Bibliography

[1] LEP Working Group for Higgs boson searches, R. Barate *et al.*, Phys. Lett. **B565**, 61 (2003), [hep-ex/0306033].

[2] The LEP Collaborations (ALEPH, DELPHI, L3 and OPAL), the LEP Electroweak Working Group and the SLD Heavy Flavour Group.

[3] T. Plehn, G. P. Salam and M. Spannowsky, Phys. Rev. Lett. **104**, 111801 (2010), [arXiv:0910.5472].

[4] J. M. Butterworth, A. R. Davison, M. Rubin and G. P. Salam, Phys. Rev. Lett. **100**, 242001 (2008), [arXiv:0802.2470].

[5] The ATLAS Collaboration, G. Aad *et al.*, *Expected Performance of the ATLAS Experiment - Detector, Trigger and Physics* (CERN, Geneva, 2009), arXiv:0901.0512.

[6] O. S. Brüning *et al.*, *LHC Design Report: the LHC Main Ring*, CERN-2004-003-V-1 (CERN, Geneva, 2004).

[7] O. S. Brüning *et al.*, *LHC Design Report: the LHC Infrastructure and General Services*, CERN-2004-003-V-2 (CERN, Geneva, 2004).

[8] M. Benedikt *et al.*, *LHC Design Report: the LHC Injector Chain*, CERN-2004-003-V-3 (CERN, Geneva, 2004).

[9] *ATLAS: technical proposal for a general-purpose pp experiment at the Large Hadron Collider at CERN*, LHC Tech. Proposal, CERN-LHCC-94-43; LHCC-P-2 (CERN, Geneva, 1994).

[10] *CMS, the Compact Muon Solenoid : technical proposal*, CERN-LHCC-94-38; LHCC-P-1 (CERN, Geneva, 1994).

[11] *LHCb : Technical Proposal*, CERN-LHCC-98-004; LHCC-P-4 (CERN, Geneva, 1998).

[12] W. Kienzle *et al.*, *TOTEM, Total Cross Section, Elastic Scattering and Diffraction Dissociation at the LHC: Technical Proposal*, CERN-LHCC-99-007; LHCC-P-5 (, 1999).

[13] *ALICE: Technical proposal for a Large Ion collider Experiment at the CERN LHC*, CERN-LHCC-95-71; LHCC-P-3 (CERN, Geneva, 1995).

[14] *ATLAS detector and physics performance: Technical Design Report, Vol. 1*, ATLAS-TDR-014 ; CERN-LHCC-99-014 (CERN, Geneva, 1999).

[15] *ATLAS detector and physics performance: Technical Design Report, Vol. 2*, ATLAS-TDR-015 ; CERN-LHCC-99-015 (CERN, Geneva, 1999).

[16] The ATLAS collaboration, G. Aad *et al.*, JINST **3**, S08003 (2008).

[17] S. L. Glashow, Nucl. Phys. **22**, 579 (1961).

[18] A. Salam and J. C. Ward, Phys. Lett. **13**, 168 (1964).

[19] S. Weinberg, Phys. Rev. Lett. **19**, 1264 (1967).

[20] Super-Kamiokande, Y. Fukuda *et al.*, Phys. Rev. Lett. **81**, 1562 (1998), [hep-ex/9807003].

[21] H. Fritzsch, M. Gell-Mann and H. Leutwyler, Phys. Lett. **B47**, 365 (1973).

[22] D. J. Gross and F. Wilczek, Phys. Rev. **D8**, 3633 (1973).

[23] H. D. Politzer, Phys. Rept. **14**, 129 (1974).

[24] B. Andersson, G. Gustafson, G. Ingelman and T. Sjostrand, Phys. Rept. **97**, 31 (1983).

[25] P. W. Higgs, Phys. Lett. **12**, 132 (1964).

[26] F. Englert and R. Brout, Phys. Rev. Lett. **13**, 321 (1964).

[27] F. Mandl and G. Shaw, *Quantum field theory* (John Wiley and Sons, 1968).

[28] A. Djouadi, Phys. Rept. **457**, 1 (2008), [hep-ph/0503172].

[29] M. Spira and P. M. Zerwas, Lect. Notes Phys. **512**, 161 (1998), [hep-ph/9803257].

[30] C. F. Kolda and H. Murayama, JHEP **07**, 035 (2000), [hep-ph/0003170].

[31] N. Cabibbo, L. Maiani, G. Parisi and R. Petronzio, Nucl. Phys. **B158**, 295 (1979).

[32] T. New Phenomena, Higgs working group, for the CDF collaboration and DZero collaboration, arXiv:0903.4001.

[33] T. New Phenomena, Higgs working group, CDF Collaboration and D0 Collaboration, arXiv:0808.0534.

[34] The ALEPH collaboration, Phys. Rept. **427**, 257 (2006), [hep-ex/0509008].

[35] CERN Report No. ATL-PHYS-PUB-2009-088, 2009 (unpublished).

[36] Particle Data Group, K. Nakamura *et al.*, J. Phys. **G37**, 075021 (2010).

[37] J. M. Campbell, R. K. Ellis and D. L. Rainwater, Phys. Rev. **D68**, 094021 (2003), [hep-ph/0308195].

[38] J. Cammin and M. Schumacher, CERN Report No. ATL-PHYS-2003-024, 2003 (unpublished).

[39] The ATLAS Collaboration, G. Aad *et al.*, *Expected Performance of the ATLAS Experiment - Detector, Trigger and Physics: Prospect for Single Top Quark Cross-Section Measurements* (CERN, Geneva, 2009), arXiv:0901.0512.

[40] S. Tsuno *et al.*, Comput. Phys. Commun. **151**, 216 (2003), [hep-ph/0204222].

[41] *ATLAS computing: Technical Design Report*, ATLAS-TDR-017 ; CERN-LHCC-2005-022 (CERN, Geneva, 2005).

[42] G. Corcella *et al.*, JHEP **01**, 010 (2001), [hep-ph/0011363].

[43] J. M. Butterworth, J. R. Forshaw and M. H. Seymour, Z. Phys. **C72**, 637 (1996), [hep-ph/9601371].

[44] T. Sjöstrand, S. Mrenna and P. Skands, JHEP **5**, 26 (2006), [arXiv:hep-ph/0603175].

[45] T. Sjöstrand, L. Lonnblad, S. Mrenna and P. Z. Skands, hep-ph/0308153.

[46] S. A. et al., Nucl. Instrum. Meth **A506**, 250 (2003).

[47] E. Richter-Was *et al.*, CERN Report No. ATL-PHYS-98-131, 1998 (unpublished).

[48] T. Cornelissen *et al.*, CERN Report No. ATL-COM-SOFT-2007-002, 2007 (unpublished).

[49] G. P. Salam, Eur. Phys. J. **C67**, 637 (2010), [arXiv:0906.1833].

[50] S. Catani, Y. L. Dokshitzer, M. H. Seymour and B. R. Webber, Nucl. Phys. **B406**, 187 (1993).

[51] S. D. Ellis and D. E. Soper, Phys. Rev. **D48**, 3160 (1993), [hep-ph/9305266].

[52] Y. L. Dokshitzer, G. D. Leder, S. Moretti and B. R. Webber, JHEP **08**, 001 (1997), [hep-ph/9707323].

[53] M. Wobisch and T. Wengler, arXiv:hep-ph/9907280.

[54] D. E. Kaplan, K. Rehermann, M. D. Schwartz and B. Tweedie, Phys. Rev. Lett. **101**, 142001 (2008), [arXiv:0806.0848].

[55] L. Asquith *et al.*, CERN Report No. ATL-COM-PHYS-2009-630, 2009 (unpublished).

[56] S. Corréard, V. Kostyukhin, J. Lévêque, A. Rozanov and J. B. De Vivie de Régie, Aix-Marseille 2. Cent. Phys. Part. Report No. ATL-PHYS-2004-006, 2003 (unpublished).

[57] G. Piacquadio and C. Weiser, Journal of Physics: Conference Series **119**, 032032 (2008).

[58] V. Kostyukhin, CERN Report No. ATL-PHYS-2003-031, 2003 (unpublished).

[59] B. P. Kersevan and E. Richter-Was, hep-ph/0405247.

[60] M. L. Mangano, M. Moretti, F. Piccinini, R. Pittau and A. D. Polosa, JHEP **0307**, 001 (2003).

[61] G. Corcella *et al.*, hep-ph/0210213.

[62] S. Hoeche *et al.*, hep-ph/0602031.

[63] S. Frixione and B. R. Webber, JHEP **06**, 029 (2002), [hep-ph/0204244].

[64] W. Beenakker *et al.*, Phys. Rev. Lett. **87**, 201805 (2001), [hep-ph/0107081].

[65] S. Moch, J. Phys. **G35**, 073001 (2008), [arXiv:0803.0457].

[66] J. Cammin, BONN-IR-2004-06.

[67] G. Altarelli and G. Parisi, Nucl. Phys. **B126**, 298 (1977).

[68] G. Altarelli, Phys. Rept. **81**, 1 (1982).

[69] M. Dobbs and J. B. Hansen, Comput. Phys. Commun. 134 (2001) 41 .

[70] Sketch of a proton-proton collision, from the sherpa generator web page: http://projects.hepforge.org/sherpa/dokuwiki/lib/exe/detail.php?media=sketch.gif.

[71] J. Alwall *et al.*, Eur. Phys. J. **C53**, 473 (2008), [arXiv:0706.2569].

[72] M. H. Seymour, Z. Phys. **C62**, 127 (1994).

[73] J. M. Butterworth, B. E. Cox and J. R. Forshaw, Phys. Rev. **D65**, 096014 (2002), [hep-ph/0201098].

[74] W. Skiba and D. Tucker-Smith, Phys. Rev. **D75**, 115010 (2007), [hep-ph/0701247].

[75] B. Holdom, JHEP **03**, 063 (2007), [hep-ph/0702037].

[76] J. M. Butterworth, J. R. Ellis and A. R. Raklev, JHEP **05**, 033 (2007), [hep-ph/0702150].

[77] J. M. Butterworth, J. R. Ellis, A. R. Raklev and G. P. Salam, Phys. Rev. Lett. **103**, 241803 (2009), [arXiv:0906.0728].

[78] CERN Report No. ATL-PHYS-PUB-2009-076. ATL-COM-PHYS-2009-262, 2009 (unpublished).

[79] U. Baur and L. H. Orr, Phys. Rev. **D77**, 114001 (2008), [arXiv:0803.1160].

[80] P. Fileviez Perez, R. Gavin, T. McElmurry and F. Petriello, Phys. Rev. **D78**, 115017 (2008), [arXiv:0809.2106].

[81] Y. Bai and Z. Han, JHEP **04**, 056 (2009), [arXiv:0809.4487].

[82] G. Piacquadio and K. Jakobs, *Identification of b-jets and investigation of the discovery potential of a Higgs boson in the $WH \to l\nu b\bar{b}$ channel with the ATLAS experiment.*, PhD thesis, Freiburg University, Freiburg, 2010.

[83] A. H. Mueller, Phys. Lett. **B104**, 161 (1981).

[84] B. I. Ermolaev and V. S. Fadin, JETP Lett. **33**, 269 (1981).

[85] A. Bassetto, M. Ciafaloni and G. Marchesini, Physics Reports **100**, 201 (1983).

[86] J. Alwall *et al.*, JHEP **09**, 028 (2007), [arXiv:0706.2334].

[87] M. Bahr *et al.*, arXiv:0812.0529.

[88] M. Cacciari, G. P. Salam and G. Soyez.

[89] A. Lazopoulos, T. McElmurry, K. Melnikov and F. Petriello, Phys. Lett. **B666**, 62 (2008), [arXiv:0804.2220].

[90] R. Lafaye, T. Plehn, M. Rauch, D. Zerwas and M. Duhrssen, JHEP **08**, 009 (2009), [arXiv:0904.3866].